HIGH-THROUGHPUT CHARACTERIZATION OF SOLID OXIDE FUEL CELL CATHODE MATERIALS

Thesis by

CHRISTOPHER JAMES KUCHARCZYK

In Partial Fulfillment of the Requirements for
the degree of
DOCTOR OF PHILOSOPHY

CALIFORNIA INSTITUTE OF TECHNOLOGY
Pasadena, California

2018
(Defended March 7, 2018)

Christopher James Kucharczyk
ORCID: 0000-0002-4712-839X

ACKNOWLEDGEMENTS

Foremost, I would like to thank my advisor, Professor Sossina Haile, for her guidance and mentorship over nearly six years and at schools thousands of miles apart. It goes without saying (but will be said anyway) that the work in this thesis would not be possible without her, but in particular her encouragement of my exploration of new tools and techniques and her flexibility in allowing me to pursue the questions about which I was curious enabled both this work and my new career. I am fortunate to have trained under such a wise and fearless leader. I am also fortunate to have met my wife in Professor Haile's conference room.

The members of the Haile Group were instrumental in supporting me, both in my research and outside it. Anu, Mike, Tim, Sihyuk, Ho-il, Haemin, Ruiyun, Rob, Hadi, Moureen, Sara, Stephen, Nate, Sheel, Xin – thank you for the coffee breaks, the chess, and the late-night biking through hallways. I am indebted to Dr. Robert Usiskin for constructing the scanning probe station, without which this work would have been quite literally impossible. I am also immensely grateful to Dr. Sihyuk Choi for his support and for allowing me to play a small role in his routine process of making fantastic scientific discoveries.

I received dozens upon dozens of samples from the tireless Dr. Xiaohang Zhang and Dr. Yangang Liang of Professor Ichiro Takeuchi's group at the University of Maryland. I am so grateful for their prolific efforts in perfecting the art of gradient deposition and for their meticulous documentation of their work.

I sorely missed Caltech after leaving, especially the people who make that place so special. Christy, Jonathan, Felicia, Michelle, Jennifer, Tess – thank you for putting so much time and effort into making Caltech a truly special place and a wonderful environment in which to do science, and also take a break from doing science. Kate, Franklin, Isak, Elise, Larissa, Viki, Stefan, Teddy, Christian, Saneyuki, Phil, Magnus, Leon, Anton, Enrique, Evan, Will, Marius, Daryl, Suichi – thanks for all the memories.

I am very grateful to have found a new home at Northwestern and to have met people who welcomed me wholeheartedly from the moment I arrived. Jack, Allie, Justin, Stephanie, David, Nathan, Kazi, Ryan, Karen, Bo, Karl – thank you for helping me make a new home.

Finally, I would like to thank my family for all their support. My mother and father have supported me in every step along my journey, and I would not be where I am today, a graduate of Caltech, without them. Words cannot express my gratitude.

And to my wife, Danielle: thank you for everything.

For Mom and Dad

ABSTRACT

Solid oxide fuel cells are electrochemical devices which convert chemical energy directly to electricity. The extreme environments in which these devices operate require the use of expensive components to withstand degradation. To lower operating temperatures and therefore cost, materials discovery efforts have targeted new electrodes with high ionic and electronic conductivity, but these studies often convolute electrode morphology and performance, masking the inherent activity of electrode materials. In this work, a high-throughput experimental technique utilizing a robotic scanning impedance probe is applied to materials libraries to rigorously compare the performance of electrode materials and characterize fundamental electrode properties.

Two cathode materials libraries are studied in-depth: the perovskite material $La_{1-x}Sr_xCo_{1-y}Fe_yO_{3-\delta}$ (LSCF) and the double perovskite material $PrBa_{0.5}Sr_{0.5}Co_{2-x}Fe_xO_{5+\delta}$ (PBSCF). Each materials library is investigated through the entire regime of cobalt and iron doping and results are obtained on both oxide-ion- and proton-conducting electrolyte materials. For LSCF, a four-fold increase in electrochemical resistance is observed from the cobalt-dominant endmember LSC64 to the iron-dominant endmember LSF64 on an oxygen-ion conducting substrate, concurrent with a decrease in chemical capacitance indicating lower oxygen vacancy concentration. For PBSCF, proton conductivity is observed through the bulk of the film, leading to its use in a real proton-conducting ceramic fuel cell that demonstrates exceptional performance at low temperatures (>500mW/cm^2 at 500°C) while remaining stable over hundreds of hours of testing. These results demonstrate the power and robustness of this high-throughput approach in characterizing both well-known and novel materials, and show great promise for future targeted searches of high-performance materials.

PUBLISHED CONTENT AND CONTRIBUTIONS

Kucharczyk, C. J., Liang, Y., Zhang, X., Choi, S., Takeuchi, I., Ji, H.-I., & Haile, S. M. Electrochemical characterization of complete $La_{0.6}Sr_{0.4}Co_{1-x}Fe_xO_{3-\delta}$ composition phase space by microelectrode impedance spectroscopy. (*in preparation*)

Measured and analyzed microelectrode impedance response across complete composition phase space of LSCF64.

Choi, S., **Kucharczyk, C. J.**, Liang, Y., Zhang, X., Takeuchi, I., Ji, H.-I., & Haile, S. M. Exceptional power density and stability at intermediate temperatures in protonic ceramic fuel cells. *Nature Energy*. doi:10.1038/s41560-017-0085-9 (2018).

Conducted micro-electrode measurements of PBSCF which revealed a two-phase boundary pathway in the thin film geometry.

Huang, R., **Kucharczyk, C. J.**, Liang, Y., Zhang, X., Takeuchi, I., & Haile, S. M. An out-of-plane ionic conductivity measurement configuration for high-throughput experiments" *ACS Combinatorial Science* (*accepted*)

Contributed to analysis of conducting pathways through metal contact electrodes in proposed measurement geometries.

Usiskin, R. E., Maruyama, S., **Kucharczyk, C. J.**, Takeuchi, I. & Haile, S. M. Probing the reaction pathway in $(La_{0.8}Sr_{0.2})_{0.95}MnO_{3+\delta}$ using libraries of thin film microelectrodes. *J Mater Chem A* **3**, 19330-19345, doi:10.1039/c5ta02428e (2015).

Developed fitting routines in MATLAB which exceeded the capabilities of commercial software in its ability to fit impedance spectra to arbitrarily complex circuit models.

Davenport, T. C., Yang, C. K., **Kucharczyk, C. J.**, Ignatowich, M. J. & Haile, S. M. Implications of Exceptional Material Kinetics on Thermochemical Fuel Production Rates. *Energy Technology* **4**, 764-770, doi:10.1002/ente.201500506 (2016).

Improved modelling routines and visualizations to determine the peak fuel production rate for a thermochemical reactor.

Davenport, T. C., Yang, C. K., **Kucharczyk, C. J.**, Ignatowich, M. J. & Haile, S. M. Maximizing fuel production rates in isothermal solar thermochemical fuel production. *Appl Energ* **183**, 1098-1111, doi:10.1016/j.apenergy.2016.09.012 (2016).

Created modelling routines and visualizations to determine the peak fuel production rate for a thermochemical reactor.

TABLE OF CONTENTS

Acknowledgements iii

Abstract vi

Published Content and Contributions vii

Table of Contents ix

Table of Figures xiii

Table of Tables xxii

Chapter 1: Introduction 1

1. Fuel Cells 3

2. Cathodes 6

Perovskites 7

Double Perovskites 9

Mixed conductors 10

3. Motivation 11

4. Outline 12

5. References 14

Chapter 2: Experimental Technique 17

1. Overview 17

2. Library Synthesis 18

Pulsed Laser Deposition 18

Target Synthesis 19

Photolithography & Ion Milling 22

3. Impedance Measurements 23

Scanning Impedance Probe 23

Impedance Spectroscopy 25

Positioning the Probe Tip 29

4. Data Analysis 30

Equivalent Circuit Models 30

Matlab Fitting Code 32

5. Experimental challenges 33

6. References 35

Chapter 3: Traditional Cathode Materials on Oxide-Ion Conducting Electrolytes 38

1. Motivation 38

2. Library preparation and preliminary characterization 39

3. Electrochemical characterization 46

Impedance measurements in scanning impedance probe 46

Impedance spectra fitting 48

4. Results and Discussion 51

General impedance features 51

Stability 55

Geometric variation 56

Surface reaction resistance 59

Comparison to literature values 68

5. Summary 70

6. Bibliography 70

Chapter 4: Novel Cathode Materials on Oxide-Ion Conducting Electrolytes . 73

1. Sample Synthesis and Characterization 73

2. Impedance Results 77

Raw spectra 77

Geometry dependence 78

Composition depdence 79

3. Comparison to LSCF 82

4. Summary 84

5. References 84

Chapter 5: Traditional Cathode Materials on Proton-Conducting Electrolytes 86

1. Challenges 87

2. Single-composition library 88

Synthesis and characterization 88

Impedance results 90

3. Composition-gradient library 92

Sample synthesis and characterization 92

Impedance results 93

4. Summary 95

5. References 96

Chapter 6: Novel Cathode Materials on Proton-conducting Electrolytes 98

1. Single-composition PBSCF Library 99

Sample preparation 99

Impedance results 101

2. BZPY Library 104

3. Comparison Summary 108

4. Application to devices 109

5. Summary 111

6. References 112

Chapter 7: Conclusion 113

1. Summary 113

2. Future Work 114

3. References 115

Appendix A: Equivalent Circuit Model Equivalence 116

Appendix B: MATLAB Code 120

1. customImpedanceFit 120

2. calculateDotPositions 132

TABLE OF FIGURES

Figure 1-1. Monthly mean global atmospheric CO_2 (left) and global mean temperature anomaly (right). Sources: NOAA (left), NASA (right). 1

Figure 1-2. SOFC schematics. *Left*, schematic of an oxygen-ion-conducting SOFC; *right*, schematic of a proton-conducting SOFC. 3

Figure 1-3. Conductivity comparison of different electrolytes[7,13]. 5

Figure 1-4. The cubic perovskite crystal structure. The A-site is represented by the green atoms, the B-site by blue atoms, and oxygen by the red atoms. 7

Figure 1-5. The double perovskite crystal structure. Note the layering of large green atoms, representing the A site, and smaller purple atoms, representing the A' site. 9

Figure 1-6. Schematic of cathode reaction pathways (adapted from Chueh and Haile). 10

Figure 2-1. Schematic overview of synthesis and measurement of gradient film samples.. 17

Figure 2-2. Schematic of photolithographic microdot pattern. 22

Figure 2-3. Images of the scanning impedance probe system. (left) Exterior view showing manual and robotic manipulators. (right) Top view of stage showing clipped sample. 24

Figure 2-4. Schematic of electrochemical impedance spectroscopy. A sinusoidal voltage perturbation (bottom) is applied to the electrode and the resulting current signal (left) is measured. This schematic represents a measurement at zero bias. 25

Figure 2-5. (left) Nyquist plot of a measured impedance spectrum. (right) Bode magnitude and phase plots of the same spectrum. 27

Figure 2-6. Schematic of ac impedance spectroscopy on a gradient film in an asymmetric geometry. 28

Figure 2-7. Mixed-conducting impedance model. 30

Figure 3-1. (left) X-ray diffraction patterns of PLD targets of LSC and LSF. (right) Thin-film X-ray diffraction patterns of deposited film gradients for both libraries. 40

Figure 3-2. Schematic (top) and image (bottom) of LSCF composition library. 41

Figure 3-3. Atomic-force microscopy images of the post-deposition surface of the LSF64 film (top left) through the LSF64 film (bottom right) of Library i (top) and Library ii (bottom) in ~10% composition steps. The rms roughness of each surface is given indicating flat, crack-free surfaces. 42

Figure 3-4. FIB-SEM cross-sectional images of top) Library i and bottom) Library ii showing variation in thickness between the LSC64 (left) and LSF64 (right) films. 44

Figure 3-5. Schematic and measured composition for Library i. Composition measured by EDS as a function of horizontal position (red X's) and expected values for a perfect linear gradient (open circles).....45

Figure 3-6. Schematic and measured composition for Library ii. Composition measured by EDS as a function of horizontal position (red X's) and expected values for a perfect linear gradient (open circles). The dashed line shows a prediction for the composition profile given the uneven thicknesses of each film. 45

Figure 3-7. (a) R(RQ)(RQ) circuit (after Crumlin et al.). (b) Circuit derived from transmission line model after Baumann et al. (c) Model from Boukamp et al. 48

Figure 3-8. Impedance spectra for a 200μm LSCF64 microdot electrode a) in Library i with magnification in b) and c) Library ii with magnification in d) measured at 600°C and 1 atm pO2 fitted to various model circuits. 49

Figure 3-9. (a) Nyquist plot of impedance spectra from 200 μm diameter LSCF microelectrodes in Library i, taken at 600°C under 1 atm O2. Solid lines indicate fit to R(RQ)(RQ) model circuit. Color corresponds to composition as shown in color bar. 52

Figure 3-10. Parameters resulting from fitting impedance data obtained at a film temperature of 600°C and 1 atm O2 to an R(RQ)(RQ) circuit as a function of composition: (a)

high frequency offset resistance; (b) electrochemical resistance; and (c) chemical capacitance. Data marker diameters correspond to the diameter of the measured microelectrode (from 500 to 100 um), while colors correspond to microelectrode composition. 53

Figure 3-11. Library stability. Initial (open circles) and final (filled circles) values, after 24 hours and 120 hours under environmental conditions respectively, of electrochemical properties of LSCF (Library ii) as a function of composition at a film temperature of 650°C and 1 atm O2 obtained from fitting impedance data to an R(RQ) circuit: (a) electrochemical resistance, and (b) chemical capacitance. Data marker diameters correspond to microelectrode diameter (from 500 to 100 um), while colors correspond to microelectrode composition. 55

Figure 3-12. Diameter dependence. Electrochemical properties of LSCF (Library i) as a function of film diameter shown as double-logarithmic plots, at a film temperature of 600 °C and atmosphere of 1 atm pO2, obtained from fitting impedance data to an R(RQ)(RQ) circuit: (a) high frequency off-set resistance, (b) electrochemical resistance, and (c) chemical capacitance. Insets in each panel show absolute value of the slope of the linear best fit line to the data on a double logarithmic scale as a function of composition. 57

Figure 3-13. Comparison of the area-specific electrochemical resistance of LSCF at 600°C (●), 625°C (■), 650°C (▲), and 675°C (◆) and 1 atm O2 obtained for both libraries. Plotted points are averaged over all microelectrodes with the same composition. (left) Library i; (right) Library ii. 59

Figure 3-14. Oxygen dependence. Area-normalized electrochemical resistance for Library ii as a function of oxygen partial pressure shown as double-logarithmic plots, at a film temperature of 650 °C. Inset shows slope as a function of composition, with a guideline at ¾. Color corresponds to microelectrode composition. Plotted values are averaged over multiple microelectrodes with the same composition. 60

Figure 3-15. Arrhenius behavior. Temperature dependence of electrode resistance in LSCF at 1 atm pO2. 61

Figure 3-16. (left) activation energy and (middle) pre-exponential factor as functions of composition determined from Arrhenius scaling. Plotted values are averaged over multiple microelectrodes with the same composition. (right) Log of the pre-exponential factor versus activation energy. 63

Figure 3-17. Repeatability. Comparison of the volume-normalized chemical capacitance of LSCF at 600°C (●), 625°C (■), 650°C (▲), and 675°C (◆) and 1 atm O2 obtained for both libraries. Plotted points are averaged over all microelectrodes with the same composition. (left) Library I; (right) Library ii. 65

Figure 3-18. Oxygen dependence. Volume-normalized chemical capacitance for Library ii as a function of oxygen partial pressure shown as double-logarithmic plots, at a film temperature of 650 °C. Inset shows slope as a function of composition, with a guideline at ¾. Color corresponds to microelectrode composition. Plotted values are averaged over multiple microelectrodes with the same composition. 66

Figure 3-19. Arrhenius behavior. Temperature dependence of chemical capacitance in LSCF (Library ii) at 1 atm pO2. Plotted values are averaged over multiple microelectrodes with the same composition. (a) Arrhenius plot of volume-normalized chemical capacitance with electrode composition shown by color; (b) activation energy and (c) pre-exponential factor as functions of composition determined from Arrhenius scaling. (d) Log of the pre-exponential factor versus activation energy. 67

Figure 4-1. Sample schematic of PBSCF gradient sample..... 74

Figure 4-2. XRD patterns of PBSC and PBSF PLD targets. (Courtesy Sihyuk Choi)..... 74

Figure 4-3. Thin-film XRD pattern of PBSC-PBSF composition spread. (Courtesy Yangang Liang, Xiaohang Zhang) 75

Figure 4-4. Atomic force microscopy (AFM) images of the PBSC-PBSF composition spread. (Courtesy Yangang Liang, Xiaohang Zhang). 76

Figure 4-5. Nyquist spectra of (left) 500um and (right) 150um microelectrodes across PBSCF gradient. Solid lines represent fits to RRQ model circuit. 77

Figure 4-6. Results of fitting RRQ circuit to PBSCF microelectrode impedance spectra. From top to bottom, offset resistance, electrochemical resistance, and total capacitance. Left column shows composition dependence for all measured diameters; right column shows diameter dependence for all measured compositions as well as values for fitted slopes. Composition values are nominal rather than as-measured. 81

Figure 4-7. Comparison of area-specific resistance of PBSCF (left) and LSCF (right). The PBSCF is measured at 650°C, while the circles on the right figure represent LSCF measured at 650°C. 82

Figure 4-8. Comparison of chemical capacitance. 83

Figure 5-1. Sample schematic. 88

Figure 5-2. LSCF6428 microelectrode on BZY20/BZY20PLD substrate. (left) Secondary electron images. (right) Backscattered electron images. 89

Figure 5-3. LSCF spectrum (top) and spectra over initial 24 hours (bottom). 90

Figure 5-4. Diameter dependence of LSCF6428 91

Figure 5-5. Schematic of gradient composition library sample. 92

Figure 5-6. Secondary electron image of 300 μm LSCF electrode showing reduced cracking but remaining pores. 93

Figure 5-7. Nyquist spectra of LSCF64 microelectrodes on BZCYYb1711 substrate. 94

Figure 5-8. Resistance (top) and capacitance (bottom) values extracted from fits to impedance spectra as a function of diameter (left) and composition (right). 94

Figure 6-1. Sample schematic of PBSCF microelectrodes on BZCYYb electrolyte 99

Figure 6-2. XRD pattern (left) and AFM image of surface (right) for L111915. 100

Figure 6-3. Nyquist spectra of PBSCF micro-electrodes on BZCYYb 101

Figure 6-4. Nyquist spectra over time showing degradation in PBSCF microelectrodes. . 102

Figure 6-5. Degradation in PBSCF microelectrode resistance over time. 103

Figure 6-6. Diameter dependence of PBSCF microelectrodes at different pO2 conditions. 104

Figure 6-7. Sample schematic of BZPY microelectrodes. 105

Figure 6-8. Nyquist spectra for BZPY microelectrodes. (left) multiple diameter microelectrodes at one composition, (right) multiple compositions at 150 um 106

Figure 6-9. Resistance vs diameter for all microelectrode compositions. 107

Figure 6-10. Summary of electrode activity on proton-conducting substrates. 108

Figure 6-11. I-V curves of fuel cell without PBSCF PLD interlayer.....109

Figure 6-12. I-V curves of fuel cell without PBSCF PLD interlayer.....110

Figure 6-13. Impedance spectra of fuel cells with and without a PLD interlayer of PBSCF on the cathode.....111

Figure A1-1. (a) R(RQ)(RQ) circuit (after Crumlin et al.). (b) Circuit derived from transmission line model after Baumann et al. (c) Model from Boukamp et al. 116

TABLE OF TABLES

Table 1-1. Fuel cell reactions 4

Table 1-2. Property-value criteria for SOFC cathode selection. 6

Table 2-1. Positions and diameters of each of the 337 micro-dots in the photolithographic pattern. Positions (mm) in bold in first row and column, diameters (μm) are all other values. 23

Table 2-2. Examples of model circuits and their impedance formulas. 31

Table 3-1. Comparison of LSCF literature results. 69

Chapter 1

INTRODUCTION

Technologies that generate electricity while producing minimal greenhouse gas emissions are essential to sustain humanity without inflicting further environmental damage. Over the last century, emissions from fossil fuels have increased the global concentration of carbon dioxide in the atmosphere to levels exceeding 400 ppm and caused a corresponding temperature increase of approximately 1°C (Figure 1-1). Continued use of carbon-emitting sources of fuel will only exacerbate this trend, resulting in devastating global climate change. Among the candidates for such clean technologies are fuel cells, which are devices that convert the energy stored in chemical fuels directly into electricity.

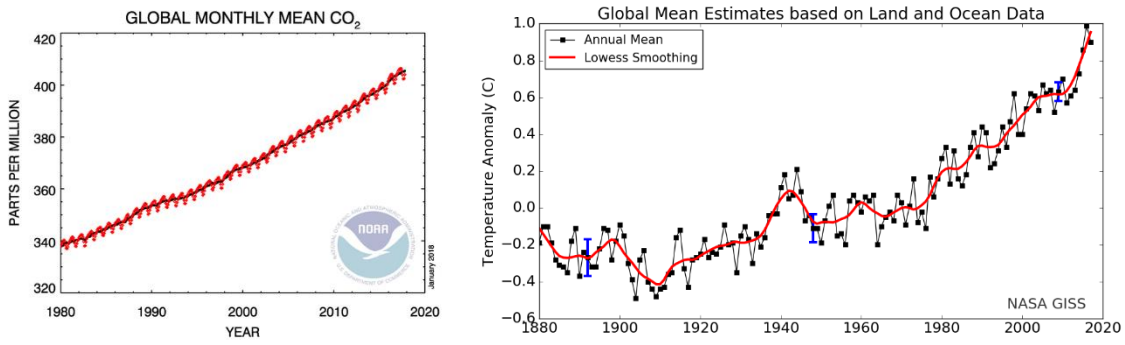

Figure 1-1. Monthly mean global atmospheric CO_2 (left) and global mean temperature anomaly (right). Sources: NOAA (left), NASA (right).

Fuel cells combine the best aspects of batteries and combustion engines: like engines, fuel cells will continue to produce power as long as fuel is supplied; like batteries, fuel cells efficiently convert chemical energy directly to electricity without combustion. Among the many types of fuel cells that exist, solid oxide fuel cells (SOFCs) are attractive due to their

exceptionally high efficiency and fuel flexibility[1]. These simple devices require, in principle, only five components: a solid oxide electrolyte, electrodes (the cathode for oxygen reduction and the anode for fuel oxidation), and interconnect wires to collect current at the electrodes. In addition to hydrogen, which when used as fuel produces only water as a by-product, many hydrocarbon fuels can be used as fuel, making SOFCs attractive as a bridge technology from the current energy ecosystem to a clean and sustainable energy future.

Despite these benefits, SOFCs have yet to achieve substantial commercial penetration. This failure largely stems from the high cost of these devices due to the components required to withstand the high temperatures at which these devices operate[2]. As such, efforts to improve these devices have focused on lowering operating temperatures to both permit the use of inexpensive stainless steel as the interconnect material and improve durability. At low temperatures, research has shown that SOFC performance is primarily limited by cathode overpotential losses[3]. This finding had motivated electrochemical characterization by many different groups of hundreds electrode material compositions in hopes of discovering a stable performance with high catalytic activity at low temperatures[2,4-6]. In each of these studies, a parameter of the synthesis procedure or measurement of the material is changed, systematically or unknowingly, leading to a resulting value for the electrochemical performance of that particular material. The myriad ways in which synthesis and characterization procedures can affect these values lead to questions regarding the rigor of comparisons between different studies or even results within the same study. The lack of such rigorous comparisons hinders understanding of the factors governing electrochemical performance of various materials and hence the development of high-performance devices.

The work presented in this thesis addresses this deficiency through further development of a high-throughput characterization technique for solid oxide fuel cell electrode materials. In so doing, a systematic understanding is sought of the properties of SOFC cathode materials that lead to improved fuel cell performance and develop techniques that aid in the discovery of new, high-performance cathode materials. Before describing the experimental technique and its application, a general introduction to fuel cell operation and cathode materials is presented.

1. Fuel Cells

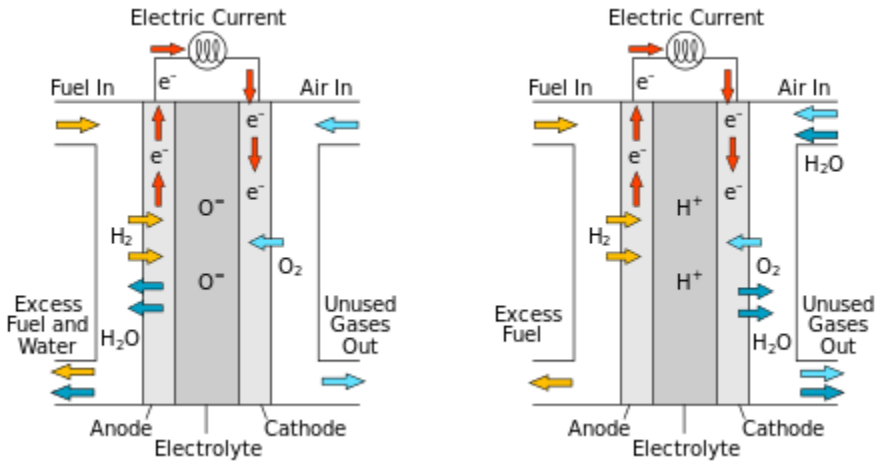

Figure 1-2. SOFC schematics. *Left*, schematic of an oxygen-ion-conducting SOFC; *right*, schematic of a proton-conducting SOFC.

Figure 1-2 shows schematics of hydrogen fuel conversion to electricity via SOFCs based on the two main types of oxide electrolytes: oxygen-ion conducting oxides (left) and proton-conducting oxides (right). For both types of electrolytes, the overall reaction is the same: fuel is oxidized at the anode and oxygen is reduced at the cathode, then water and, if hydrocarbon fuels are used, carbon dioxide are released as by-products:

$$2H_2 + O_2 \rightarrow 2H_2O(g) \quad (1.1)$$

$$CH_4 + 2O_2 \rightarrow 2H_2O(g) + CO_2 \quad (1.2)$$

However, the half-reactions differ by electrolyte type as shown below in Table 1-1.

Table 1-1. Fuel cell reactions

	Oxygen-ion conducting electrolyte	**Proton-conducting electrolyte**
Anode	$2H_2 + 2O^{2-} \rightarrow 2H_2O + 4e^-$ (1.3)	$2H_2 \rightarrow 4H^+ + 4e^-$ (1.4)
Cathode	$O_2 + 4e^- \rightarrow 2O^{2-}$ (1.5)	$4H^+ + 4e^- + O_2 \rightarrow 2H_2O$ (1.6)
Overall	$\mathbf{2H_2 + O_2 \rightarrow 2H_2O}$	$\mathbf{2H_2 + O_2 \rightarrow 2H_2O}$

In the case of oxygen-ion conducting electrolytes, water is produced on the anode side after the oxidation of the fuel (Equation 1.3). For proton-conducting electrolytes, water is produced on the cathode side, preventing fuel dilution (Equation 1.6). The canonical oxygen-ion conducting electrolyte used in solid oxide fuel cells is yttria-stabilized zirconia, commonly abbreviated YSZ[7]. Doping with yttria stabilizes the high-temperature cubic fluorite phase of zirconia at lower temperatures and introduces oxygen vacancies which lead to high ionic conductivity. Other common oxygen-ion conducting electrolytes are based on doped ceria[8] or doped lanthanum gallate[9].

As contrasted with oxygen-ion conducting electrolytes, proton-conducting oxides such as yttrium-doped barium zirconate (abbreviated BZY) uptake hydroxyl molecules onto oxygen vacancy sites and conduct protons via a Grotthuss mechanism, hopping from oxygen atom

to oxygen atom within the lattice[10]. Proton-conducting electrolytes offer two distinct beneifts: first, the lower activation energy posed by proton migration and therefore improved conductivity at lower temperatures; second, water is produced at the cathode rather than the anode, and thus fuel dilution is avoided. A comparison of the conductivity of yttria-stabilized zirconia ($E_a^{YSZ} = 1.1$ eV [11]) and yttrium-doped barium zirconate ($E_a^{BZY} = 0.45$ eV[12]) is shown in Figure 1-3.

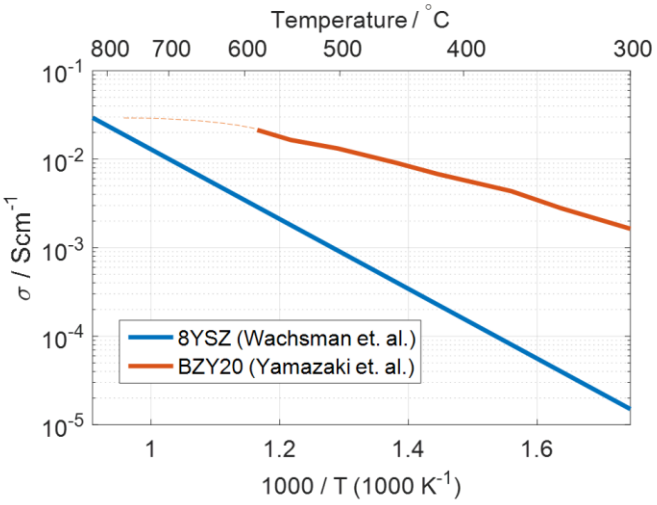

Figure 1-3. Conductivity comparison of different electrolytes[7,13].

For oxide materials, the most common proton-conducting electrolytes are based on doped $BaZrO_3$ and $BaCeO_3$, where the dopant is a trivalent metal cation (often yttrium)[14,15]. The former material offers excellent chemical stability and high bulk proton conductivity, but is highly refractory and thus difficult both to sinter densely for use as an electrolyte and to achieve large grain sizes that minimize the contribution to the conductivity of highly resistive grain boundaries. The latter material is susceptible to decomposition into $BaCO_3$ and CeO_2

in carbon-containing atmospheres, and thus degrades when unprocessed air is used at the cathode or when carbon monoxide is used as the fuel.

Table 1-2. Property-value criteria for SOFC cathode selection.

Property	Desired qualitative value
Catalytic activity	Highly active toward oxygen reduction
Thermal expansion coefficient	Good matching to electrolyte to prevent cracking or degradation when cycled
Electrical conductivity	As high as possible to avoid ohmic electronic losses
Ionic conductivity	Sufficiently high to permit surface reaction and bulk transport
Stability	Cannot degrade/oxidize under fuel cell-relevant conditions such as high temperature or highly oxidizing atmosphere
Abundance/cost	Cheap, earth-abundant elements preferred
Manufacturability	Materials amenable to mass-manufacturing techniques such as screen printing, e.g., easily sinterable
Reactivity with electrolyte	Electrode materials which react with common electrolyte materials are not suitable

2. Cathodes

The purpose of the cathode is to catalyze the oxygen reduction reaction (Equations 1.5 and 1.6). While precious metals such as platinum serve as excellent catalysts, their high cost prohibits use in real devices. In fact, many considerations must be accounted for when choosing an appropriate SOFC cathode material, considered in Table 1-2 above. Each of the listed properties in the table have some desired value that corresponds to improved fuel cell performance, specifically high power density or minimal degradation. The magnitude of the

contribution of each of these parameters to the long-term performance of a device varies widely.

Finding a material that meets all of these criteria is difficult, and efforts over the last half century have shown many different approaches leading to the use of many different materials[5]. Two of the major families of materials that have emerged as successful candidates for use in SOFCs are perovskites and double perovskites, referred to by the structure in which these materials form.

Perovskites

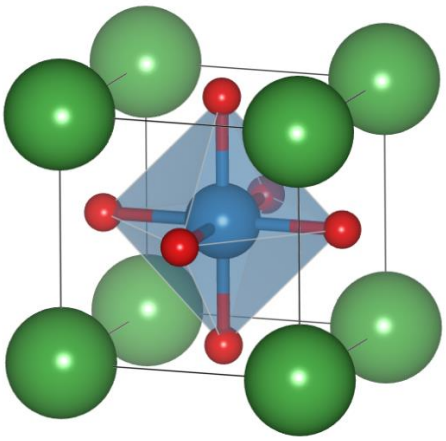

Figure 1-4. The cubic perovskite crystal structure. The A-site is represented by the green atoms, the B-site by blue atoms, and oxygen by the red atoms.

The types of oxides most frequently used as SOFC cathodes form the perovskite structure, ABO_3, where canonically A is a 12-fold coordinated 2+ cation and B a 6-fold coordinated 4+ cation. The structure is named after the mineral perovskite, $CaTiO_3$, which forms in the cubic structure. An image of the perovskite crystal structure is shown in Figure 1-4. Many

combinations of elements have been found to form this structure, though different combinations of elements have often formed distorted perovskite structures that are pseudocubic, such as rhombohedral or orthorhombic[4]. A predictor of whether a material will stably form the perovskite structure is the Goldschmidt tolerance factor *t*, calculated as shown in Equation 1.7:

$$t = \frac{r_A + r_O}{\sqrt{2}(r_B + r_O)} \qquad 1.7$$

where r_A is the ionic radius of the metal cation on the A-site, r_B the radius of the metal cation on the B-site, and r_O the radius of the oxygen anion. When t is close to 1, the material should stably form in the perovskite structure, though it may be distorted. The tolerance of this structure to defects also allows it to incorporate oxygen vacancies and hence conduct oxygen ions.

$La_{0.6}Sr_{0.4}Co_{1-y}Fe_yO_{3-\delta}$ (LSCF64) is chosen as the canonical perovskite material for this thesis, and for the point of reference for case studies on each of oxygen-ion conducting and proton-conducting electrolytes. LSCF64 is a well-studied pseudo-cubic perovskite and mixed ionic and electronic conductor[16-20]. The ratio of strontium and lanthanum largely controls the resulting oxygen non-stoichiometry δ, while the ratio of cobalt and iron relates to thermal expansivity and electronic conductivity. The cobalt-dominant range of this family typically exhibits higher electronic and ionic conductivity, while the substitution of iron lowers the thermal expansion coefficient to a range more comparable to that of zirconia-based electrolytes[4]. Surface strontium segregation is thought to limit the performance of these materials through the formation of ion- and electron-blocking phases at the surface, a problem somewhat worse in the iron-dominant range[21-24].

Double Perovskites

When a large difference exists between the radii of doped cations within either the A site or the B-site, these cations preferentially order into layers giving rise to the double perovskite structure, denoted $AA'BB'O_5$. This structure consists of a doubled perovskite unit cell with alternating ordered layers consisting of A or A' cations (or alternately, B and B' cations if the mismatch exists on the B-site). In the lanthanide layer, when the A/A' site is occupied by a lanthanide and an alkali rare earth, the oxygen bond strength is weakened, leading to channels of high oxygen vacancy concentration and hence high oxygen diffusivity[25]. An image of the double perovskite structure is shown in Figure 1-5, where the A and A' atoms are represented by large green and purple spheres respectively, oxygen is represented by small red spheres, and the B site atom is represented by blue spheres.

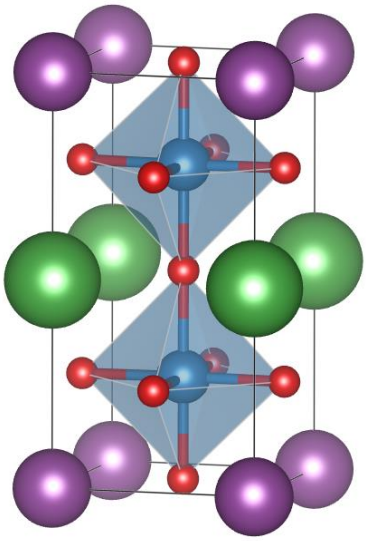

Figure 1-5. The double perovskite crystal structure. Note the layering of large green atoms, representing the A site, and smaller purple atoms, representing the A' site.

$PrBa_{0.5}Sr_{0.5}Co_{2-x}Fe_xO_{5+\delta}$ (PBSCF) is chosen as the novel cathode material for this thesis. PBSCF is a relatively novel cathode material, first demonstrated to have exceptional performance in a fuel cell 2013[26]. Though some studies exist on PBSCF and related compounds[27-29], the data are sparse, especially with regard to composition variation. It therefore presents a good counterpoint to LSCF for investigation, as the systematic trends of performance of PBSCF with cobalt-iron substitution has yet to be determined.

Mixed conductors

Materials that form each of these structures have been found to be mixed ion- and electron-conducting (MIEC) materials[30]. Mixed conducting cathodes are attractive because they make the entire electrode surface a viable reaction site, as oxygen ions reduced at the surface can be transported through the bulk electrode by ionic conduction (See Figure 1-6**Error! Reference source not found.**). This contrasts with purely electronic conductors, for which the available reaction sites are restricted to the triple phase boundary, where the gas, electrode, and electrolyte all meet and oxygen can be reduced and incorporated into the electrolyte. Many modern fuel cell electrodes are designed to maximize the density of the triple phase boundary by using composites or making highly porous structures.

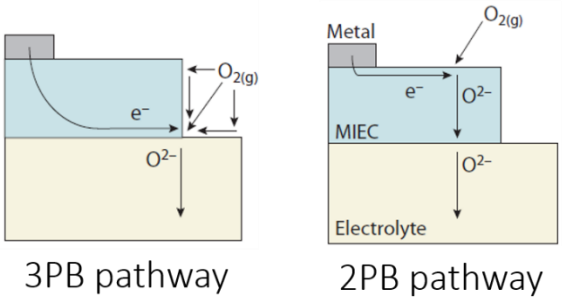

Figure 1-6. Schematic of cathode reaction pathways (adapted from Chueh and Haile).

These mixed conducting materials pose additional opportunities for cell engineering, as devices no longer require optimization of triple-phase boundaries through the use of complex composite materials. Rather, optimization efforts can focus on the appropriate structuring of the mixed conducting materials. Some knowledge of the underlying properties of these mixed conducting materials is required to perform this morphology optimization. In particular, the precise electronic and ionic conductivity must be known to determine the appropriate structure to use to maximize useful reaction site density. Many studies show varying results when measuring these properties[31]. For example, measuring the surface reaction constant and diffusivity for LSCF has yielded quantities differing by orders of magnitude depending on the experimental technique used to perform the measurement and the group performing the study[2].

3. Motivation

This presents a problem which this thesis seeks to address. Given the wide variation in measured kinetic parameters among the many different types of materials studied, how is it possible to precisely measure meaningful trends between observed parameters between different materials? How then is it possible to select and engineer the most optimal materials for a given fuel cell device?

This work addresses this problem through the use of a standardized thin-film electrode geometry. To address the convolution of morphology and performance, impedance spectroscopy on patterned thin-film model electrodes has emerged as a useful tool to rigorously investigate the electrochemical properties of mixed ion- and electron-conducting (MIEC) electrode materials[32-41]. By controlling the geometry in which these materials are

measured, valuable information about the dominant electrochemical pathway as well as fundamental material properties can be extracted. While important advances have made with this technique, the majority of the studies have been restricted to the measurement of relatively few microelectrodes due to the tedious nature of manual operation of the probing equipment. In a work done by a previous student[41], the use of an automated robotic probe was demonstrated to vastly increase the number of microelectrodes that can be measured using this technique. In this work, we further extend this methodology by utilizing, in addition to traditional geometry gradients, a composition gradient thin film[42] deposited by pulsed laser deposition. This methodology, in which the deposited material compositions are synthesized and characterized simultaneously under identical environmental conditions, removes much of the variation resulting from morphology variation and thus enables rigorous materials performance comparisons.

In addition to a technique for rigorously comparing materials performance, this approach is also useful as a method for characterizing novel materials or even exploring new regions of composition phase space. As long as the two deposition targets which formulate the end members of the composition spread are stable, a thin film gradient can be deposited even if it the resulting film does not form in a single phase solid solution across the entire composition range in question. Though it is not carried out here, the groundwork is laid for the exploration of new materials using this technique.

4. Outline

The work in this thesis is summarized in Table 1-2 below. This chapter provides an introduction to fuel cells and motivation for pursuing their study. Chapter 2 details the

experimental methods used in this thesis to investigate fuel cell materials, specifically the further development of a high-throughput synthesis and characterization technique for rapid serial characterization of multiple material compositions and geometries. The remaining chapters focus on the results of experiments on the two selected cathode material compositions which exemplify both well-known and novel materials compositions, LSCF and PBSCF.

Chapter 3 presents the investigation of the composition phase space of an LSCF composition library on a YSZ electrolyte substrate. Chapter 4 contains the results of a similar study on PBSCF. Chapter 5 presents an investigation of the performance of LSCF on a proton-conducting electrolyte, BZCYYb. Chapter 6 presents a similar study of PBSCF electrolytes and describes how the results of this study impact real-world fuel cell performance. Finally, Chapter 7 presents a summary of the conclusions drawn from this thesis and describes future work.

	Oxygen-ion conducting electrolyte (YSZ)	Proton-conducting electrolyte (BZCYYb)
LSCF	**Chapter 3**: State-of-the-art cathode material on traditional electrolyte	**Chapter 5**: State-of-the-art cathode material on novel electrolyte
PBSCF	**Chapter 4**: Novel cathode material on traditional electrolyte	**Chapter 6**: Novel cathode material on novel electrolyte

5. References

1 Kendall, K. & Kendall, M. *High Temperature Solid Oxide Fuel Cells for the 21st Century*. 2 edn, (Elsevier, 2015).

2 Gao, Z., Mogni, L. V., Miller, E. C., Railsback, J. G. & Barnett, S. A. A perspective on low-temperature solid oxide fuel cells. *Energ Environ Sci* **9**, 1602-1644, doi:10.1039/c5ee03858h (2016).

3 Adler, S. B. Factors governing oxygen reduction in solid oxide fuel cell cathodes. *Chem Rev* **104**, 4791-4843, doi:Doi 10.1021/Cr020724o (2004).

4 Jun, A., Kim, J., Shin, J. & Kim, G. Perovskite as a Cathode Material: A Review of its Role in Solid-Oxide Fuel Cell Technology. *Chemelectrochem* **3**, 511-530, doi:10.1002/celc.201500382 (2016).

5 Aguadero, A. *et al.* Materials development for intermediate-temperature solid oxide electrochemical devices. *J Mater Sci* **47**, 3925-3948, doi:DOI 10.1007/s10853-011-6213-1 (2012).

6 Sun, C. W., Hui, R. & Roller, J. Cathode materials for solid oxide fuel cells: a review. *Journal of Solid State Electrochemistry* **14**, 1125-1144, doi:DOI 10.1007/s10008-009-0932-0 (2010).

7 Wachsman, E. D. & Lee, K. T. Lowering the Temperature of Solid Oxide Fuel Cells. *Science* **334**, 935-939, doi:DOI 10.1126/science.1204090 (2011).

8 Inaba, H. & Tagawa, H. Ceria-based solid electrolytes - Review. *Solid State Ionics* **83**, 1-16, doi:Doi 10.1016/0167-2738(95)00229-4 (1996).

9 Huang, K. Q., Tichy, R. & Goodenough, J. B. Superior perovskite oxide-ion conductor; strontium- and magnesium-doped LaGaO3: III, Performance tests of single ceramic fuel cells. *J Am Ceram Soc* **81**, 2581-2585 (1998).

10 Yamazaki, Y. *et al.* Proton trapping in yttrium-doped barium zirconate. *Nat Mater* **12**, 647-651, doi:Doi 10.1038/Nmat3638 (2013).

11 Badwal, S. P. S. Zirconia-based solid electrolytes: microstructure, stability and ionic conductivity. *Solid State Ionics* **52**, 23-32, doi:https://doi.org/10.1016/0167-2738(92)90088-7 (1992).

12 Babilo, P. & Haile, S. M. Enhanced sintering of yttrium-doped barium zirconate by addition of ZnO. *J Am Ceram Soc* **88**, 2362-2368, doi:DOI 10.1111/j.1551-2916.2005.00449.x (2005).

13 Yamazaki, Y., Hernandez-Sanchez, R. & Haile, S. M. High Total Proton Conductivity in Large-Grained Yttrium-Doped Barium Zirconate. *Chem Mater* **21**, 2755-2762, doi:Doi 10.1021/Cm900208w (2009).

14 Kreuer, K. D. Proton-Conducting Oxides. *Annu Rev Mater Res* **33**, 333-359, doi:10.1146/annurev.matsci.33.022802.091825 (2003).

15 Medvedev, D. *et al.* BaCeO3: Materials development, properties and application. *Progress in Materials Science* **60**, 72-129, doi:DOI 10.1016/j.pmatsci.2013.08.001 (2014).

16 Hashimoto, S. *et al.* Oxygen nonstoichiometry and thermo-chemical stability of La0.6Sr0.4Co1-yFeyO3-delta (y=0.2, 0.4, 0.6, 0.8). *Solid State Ionics* **181**, 1713-1719, doi:10.1016/j.ssi.2010.09.024 (2010).

17 Teraoka, Y., Zhang, H. M., Okamoto, K. & Yamazoe, N. Mixed Ionic-Electronic Conductivity of La1-Xsrxco1-Yfeyo3-Delta Perovskite-Type Oxides. *Mater Res Bull* **23**, 51-58, doi:Doi 10.1016/0025-5408(88)90224-3 (1988).

18 Petric, A., Huang, P. & Tietz, F. Evaluation of La-Sr-Co-Fe-O perovskites for solid oxide fuel cells and gas separation membranes. *Solid State Ionics* **135**, 719-725, doi:Doi 10.1016/S0167-2738(00)00394-5 (2000).

19 Kuhn, M., Hashimoto, S., Sato, K., Yashiro, K. & Mizusaki, J. Thermo-chemical lattice expansion in La0.6Sr0.4Co1-yFeyO3-delta. *Solid State Ionics* **241**, 12-16, doi:DOI 10.1016/j.ssi.2013.03.023 (2013).

20 Plonczak, P., Sogaard, M., Bieberle-Hutter, A., Hendriksen, P. V. & Gauckler, L. J. Electrochemical Characterization of La0.58Sr0.4Co0.2Fe0.8O3-delta Thin Film Electrodes Prepared by Pulsed Laser Deposition. *J Electrochem Soc* **159**, B471-B482, doi:10.1149/2.043204jes (2012).

21 Jung, W. & Tuller, H. L. Investigation of surface Sr segregation in model thin film solid oxide fuel cell perovskite electrodes. *Energ Environ Sci* **5**, 5370-5378, doi:Doi 10.1039/C1ee02762j (2012).

22 Ding, H. P., Virkar, A. V., Liu, M. L. & Liu, F. Suppression of Sr surface segregation in La1-xSrxCo1-yFeyO3-delta: a first principles study. *Phys Chem Chem Phys* **15**, 489-496, doi:10.1039/c2cp43148c (2013).

23 Finsterbusch, M., Lussier, A., Schaefer, J. A. & Idzerda, Y. U. Electrochemically driven cation segregation in the mixed conductor La0.6Sr0.4Co0.2Fe0.8O3-delta. *Solid State Ionics* **212**, 77-80, doi:10.1016/j.ssi.2012.02.006 (2012).

24 Wang, H. Q. *et al.* Mechanisms of Performance Degradation of (La,Sr)(Co,Fe)O3-delta Solid Oxide Fuel Cell Cathodes. *J Electrochem Soc* **163**, F581-F585, doi:10.1149/2.0031607jes (2016).

25 Taskin, A. A., Lavrov, A. N. & Ando, Y. Achieving fast oxygen diffusion in perovskites by cation ordering. *Appl Phys Lett* **86**, 091910, doi:10.1063/1.1864244 (2005).

26 Choi, S. *et al.* Highly efficient and robust cathode materials for low-temperature solid oxide fuel cells: PrBa0.5Sr0.5Co(2-x)Fe(x)O(5+delta). *Scientific reports* **3**, 2426, doi:10.1038/srep02426 (2013).

27 Jeong, D. *et al.* Structural, Electrical, and Electrochemical Characteristics of LnBa0.5Sr0.5Co1.5Fe0.5O5+δ (Ln=Pr, Sm, Gd) as Cathode Materials in Intermediate-Temperature Solid Oxide Fuel Cells. *Energy Technology* **5**, 1337-1343, doi:10.1002/ente.201600618 (2017).

28 Park, S., Choi, S., Shin, J. & Kim, G. A collaborative study of sintering and composite effects for a PrBa0.5Sr0.5Co1.5Fe0.5O5+delta IT-SOFC cathode. *Rsc Adv* **4**, 1775-1781, doi:10.1039/c3ra45296d (2014).

29 Jiang, L., Wei, T., Zeng, R., Zhang, W. X. & Huang, Y. H. Thermal and electrochemical properties of PrBa0.5Sr0.5Co2-xFexO5+delta (x=0.5, 1.0, 1.5) cathode materials for solid-oxide fuel cells. *J Power Sources* **232**, 279-285, doi:10.1016/j.jpowsour.2013.01.064 (2013).

30 Chueh, W. C. & Haile, S. M. Electrochemistry of Mixed Oxygen Ion and Electron Conducting Electrodes in Solid Electrolyte Cells. *Annu Rev Chem Biomol* **3**, 313-341, doi:DOI 10.1146/annurev-chembioeng-073009-101000 (2012).

31 Jiang, S. P. Development of lanthanum strontium manganite perovskite cathode materials of solid oxide fuel cells: a review. *J Mater Sci* **43**, 6799-6833, doi:10.1007/s10853-008-2966-6 (2008).

32 Fleig, J. Microelectrodes in solid state ionics. *Solid State Ionics* **161**, 279-289, doi:Doi 10.1016/S0167-2738(03)00217-0 (2003).

33 Brichzin, V., Fleig, J., Habermeier, H. U. & Maier, J. Geometry dependence of cathode polarization in solid oxide fuel cells investigated by defined Sr-doped LaMnO3 microelectrodes. *Electrochem Solid St* **3**, 403-406, doi:Doi 10.1149/1.1391160 (2000).

34 Baumann, F. S. *et al.* Quantitative comparison of mixed conducting SOFC cathode materials by means of thin film model electrodes. *J Electrochem Soc* **154**, B931-B941, doi:Doi 10.1149/1.2752974 (2007).

35 la O', G. J. & Shao-Horn, Y. Thickness Dependence of Oxygen Reduction Reaction Kinetics on Strontium-Substituted Lanthanum Manganese Perovskite Thin-Film Microelectrodes. *Electrochem Solid St* **12**, B82-B85, doi:Doi 10.1149/1.3095681 (2009).

36 Sasaki, K. A., Hao, Y. & Haile, S. M. Geometrically asymmetric electrodes for probing electrochemical reaction kinetics: a case study of hydrogen at the Pt-CsH2PO4 interface. *Phys Chem Chem Phys* **11**, 8349-8357, doi:Doi 10.1039/B909498a (2009).

37 Crumlin, E. J. *et al.* Oxygen Reduction Kinetics Enhancement on a Heterostructured Oxide Surface for Solid Oxide Fuel Cells. *The Journal of Physical Chemistry Letters* **1**, 3149-3155, doi:10.1021/jz101217d (2010).

38 Wedig, A., Merkle, R. & Maier, J. Oxygen Exchange Kinetics of (Bi,Sr)(Co,Fe)O3-delta Thin-Film Microelectrodes. *J Electrochem Soc* **161**, F23-F32, doi:10.1149/2.017401jes (2014).

39 Kogler, S., Nenning, A., Rupp, G. M., Opitz, A. K. & Fleig, J. Comparison of Electrochemical Properties of La0.6Sr0.4FeO3-delta Thin Film Electrodes: Oxidizing vs. Reducing Conditions. *J Electrochem Soc* **162**, F317-F326, doi:10.1149/2.0731503jes (2015).

40 Poetzsch, D., Merkle, R. & Maier, J. Oxygen Reduction at Dense Thin-Film Microelectrodes on a Proton-Conducting Electrolyte I. Considerations on Reaction Mechanism and Electronic Leakage Effects. *J Electrochem Soc* **162**, F939-F950, doi:10.1149/2.0951508jes (2015).

41 Usiskin, R. E., Maruyama, S., Kucharczyk, C. J., Takeuchi, I. & Haile, S. M. Probing the reaction pathway in (La0.8Sr0.2)(0.95)MnO3+delta using libraries of thin film microelectrodes. *J Mater Chem A* **3**, 19330-19345, doi:10.1039/c5ta02428e (2015).

42 Koinuma, H. & Takeuchi, I. Combinatorial solid-state chemistry of inorganic materials. *Nat Mater* **3**, 429-438 (2004).

Chapter 2

EXPERIMENTAL TECHNIQUE

This chapter details the experimental methods used to synthesize libraries of cathode material micro-electrodes and to acquire and analyze impedance data. The construction of the probe and its commissioning was principally the work of a previous student. The main contribution of this thesis work was to the systems used to analyze and visualize the large volumes of data resulting from high-throughput measurements and to the application of this technique to composition gradient materials libraries. An overview of the entire process will first be provided, followed by an in-depth description of the data analysis techniques used. The MATLAB code generated as a critical part of this thesis work is included in Appendix B.

1. Overview

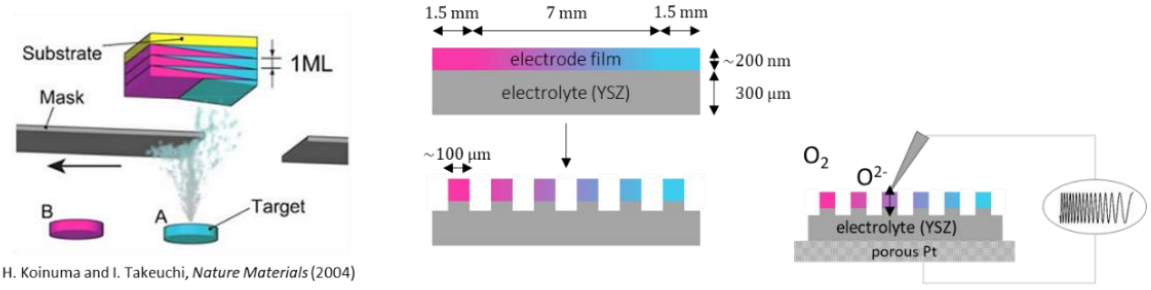

Figure 2-7. Schematic overview of synthesis and measurement of gradient film samples.

An overview of the process by which cathode material composition libraries are synthesized and characterized is shown in **Error! Not a valid bookmark self-reference.**. Pulsed laser deposition is used with an occluding shutter to deposit a film that varies in composition

between two target materials (left image). Photolithography and ion milling are used to etch the film into isolated micro-electrodes of a given geometry (center image). Finally, electrochemical impedance spectroscopy is performed in a scanning electrochemical impedance probe at high temperatures under oxidizing conditions to determine material parameters. After impedance spectra are measured, they are analyzed by fitting the data to a model circuit that represents electrochemical processes. The extracted fit parameters are used to quantify materials parameters such as electrochemical resistance (an inverse measure of catalytic activity) or chemical capacitance.

2. Library Synthesis

This section covers each step of the sample synthesis process in depth to allow for more concise coverage in later chapters.

Pulsed Laser Deposition

Pulsed laser deposition (PLD) is a physical vapor deposition technique for thin film deposition of a target material onto a substrate. First, a ceramic pellet (often called a target) of a material with a desired composition is ablated by a high-power laser and the resulting plasma plume is directed towards a heated substrate. When a composition gradient is desired, a shutter is drawn across the sample during this deposition, occluding the plume from a specific region. This results in a film with a thickness gradient across the substrate, with the thickest region calibrated to be approximately one monolayer of material. In a second step, the targets and the direction of the shutter are switched, resulting in a second gradient film atop the first. When repeated, this process yields a film of uniform thickness, for this study typically on the order of 200 nm, and a linear composition gradient in the middle region of

the substrate. The same general procedure applies to synthesizing films of a single composition, as the gradient shutter is omitted and only one composition is used. In addition, many films characterized employed an interfacial film layer of some kind, in particular for films containing lanthanum to avoid the formation of resistive lanthanum zirconate[1].

Growth of either a gradient or single-composition film to a desired thickness requires calibration of the film growth rate which depends on laser power, gas environment, laser repetition rate, target material, interlayer material, substrate material, and substrate temperature. For this thesis, the substrate material is either single-crystal YSZ with an SDC20 interlayer, $BaZr_{0.8}Y_{0.2}O_3$ (BZY20), or $BaZr_{0.4}Ce_{0.4}Y_{0.1}Yb_{0.1}O_3$ (BZCYYb4411). For each target/substrate pair, calibration was performed by depositing a fixed number of pulses onto the substrate and measuring the thickness of the resulting film using x-ray reflectance, yielding a thickness per pulse used to determine the number of pulses required for a given thickness of a given material.

Target Synthesis

To perform pulsed laser deposition, dense single-phase targets approximately 1 inch in diameter and 4-10 mm in height are required. The targets are created by traditional ceramic processing techniques including powder synthesis, pellet formation, and sintering. Powders were prepared by either a solid-state reaction process or a modified Pechini process, each of which is described below.

Solid State Reaction

Appropriate stoichiometric amounts of source powders, typically carbonates or raw oxides, were ball milled for 8h with ethanol and yttria-stabilized zirconia balls as the milling medium

in a 2:2:1 weight ratio of powder:YSZ balls:ethanol. The resulting powder was dried, sieved, and lightly pressed into a pellet. The resulting green pellet was calcined, typically at 600-800°C. The calcined pellet was crushed, and the milling and pressing steps were repeated until the desired phase was formed.

Modified Pechini/Sol-gel process

The Pechini process[2] is an aqueous synthesis method useful for creating powders with very small particle sizes and good chemical homogeneity. In this work, the original Pechini method was modified to what is often termed a modified sol-gel synthesis. Ethylene diamine tetra acetic acid (EDTA) is used as a chelating agent to bind dissolved metal cations. Ammonium hydroxide is used to fully dissolve the EDTA and to act as a buffer against citric acid, which is used to separate the EDTA molecules to ensure fine particle dispersion.

To utilize this sol-gel routine, water-soluble precursors for the necessary metal cations must be found. Often, these metal cations are present in hydrated nitrate precursors, which under storage deviate from their nominal water content. Therefore, to ensure precise stoichiometry, the water content of these precursors must be measured. This is carried out by thermogravimetric analysis. A weighed amount of precursor powder is placed in a TGA precursor and the weight loss is observed upon heating to high temperatures (often 800°C). The evaporated amount of water is then calculated and used to determine the appropriate amount of powder to weigh.

After water stoichiometry is determined, the precursors are dissolved in stoichiometric amounts in a stirred and heated water solution. The molar ratio of metal cations to EDTA and citric acid was 1:1:2. The solution was heated at 65°C until a thick gel formed. The gel

was then calcined at 200-300°C in an alumina crucible until a crunchy black char was formed. This char was again calcined at 600°C, resulting in a fine powder. If the desired phase was not achieved, the powder was again calcined at higher temperatures.

Target pressing

Green body pellets were formed by pressing 20-25 grams of powder in a uniaxial press using a steel pressing die with a 1.25" hole and plungers. The powder was placed into the die with a bottom plunger held up by spacers so that the top of the powder could be levelled off with a razor blade. This ensured uniform pressure was applied to the entire face of the pellet by the plunger, reducing the chance of cracking. Tamping the powder to create a level surface was avoided because the act of tamping serves to separate powders with different particle sizes, i.e., small particles fall to the bottom and large particles rise to the surface, creating a gradient which can result in cracks. The uniaxial press was slowly applied to the pellet until a pressure of 20 MPa was reached. The pellet was allowed to rest for 10 minutes and the pressure was then very slowly removed.

After a green body pellet was formed, isostatic pressing was conducted. The pellet was vacuum sealed in a latex barrier (typically an unlubricated condom) under water aspiration to avoid excess vacuum pressure. The sealed pellet was then placed in a cold isostatic press (American Isostatic Presses CP-360) and pressurized to 250 MPa for 20 minutes.

The green pellet was then fired in a tube furnace to an appropriate sintering temperature, typically 1200°C, for 8-24 hours to form a densely sintered pellet. The temperature was ramped at 1-5°C/min to avoid cracking.

Photolithography & Ion Milling

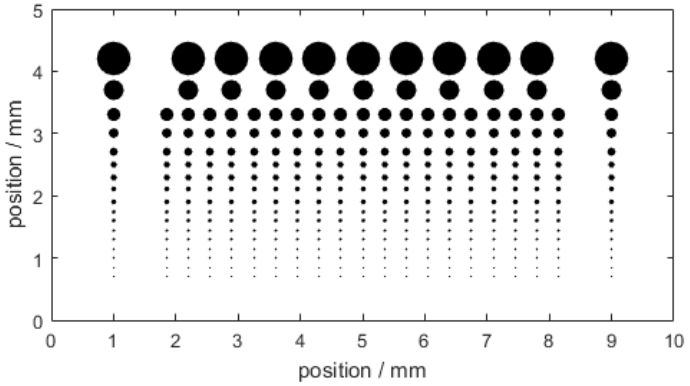

Figure 2-8. Schematic of photolithographic microdot pattern.

Once a film is synthesized on a substrate, the film is prepared for electrochemical characterization by creating electronically isolated microelectrodes. Photolithography and ion milling were carried out according to previously described techniques[3]. First, a photolithographic mask is created that defines the shape of the microelectrodes (Figure 2-8. Schematic of photolithographic microdot pattern.Figure 2-8). In this work, the pattern consists of circles varying in diameter from 500 μm to 30 μm with logarithmically even spacing (see Table 2-3). The largest dots (500 μm and 300 μm) are alternated every other column to avoid micro-electrode overlap, while the smaller dots are more finely spaced to improve composition resolution. In this geometry, the dependence of electrochemical parameters such as resistance on electrode surface area can be determined to elucidate reaction pathways. A layer of positive photoresist (Shipley 1813) is applied and exposed to UV light through this mask to harden the areas containing the circular electrodes. The photoresist is then developed using MF-319 developer, after which only the dark areas of the mask remain. Ion milling was then carried out at the University of Maryland in a modified

TEM mill which uses directed argon ions to etch the oxide in the uncovered regions to form the film pattern.

Table 2-3. Positions and diameters of each of the 337 micro-dots in the photolithographic pattern. Positions (mm) in bold in first row and column, diameters (μm) are all other values.

	1	**1.85**	**2.2**	**2.55**	**2.9**	**3.25**	**3.6**	**3.95**	**4.3**	**4.65**	**5**	**5.35**	**5.7**	**6.05**	**6.4**	**6.75**	**7.1**	**7.45**	**7.8**	**8.15**	**9**
4.2	500		500		500		500		500		500		500		500		500		500		500
3.7	300		300		300		300		300		300		300		300		300		300		300
3.3	200	200	200	200	200	200	200	200	200	200	200	200	200	200	200	200	200	200	200	200	200
3	150	150	150	150	150	150	150	150	150	150	150	150	150	150	150	150	150	150	150	150	150
2.7	125	125	125	125	125	125	125	125	125	125	125	125	125	125	125	125	125	125	125	125	125
2.5	100	100	100	100	100	100	100	100	100	100	100	100	100	100	100	100	100	100	100	100	100
2.3	100	100	100	100	100	100	100	100	100	100	100	100	100	100	100	100	100	100	100	100	100
2.1	80	80	80	80	80	80	80	80	80	80	80	80	80	80	80	80	80	80	80	80	80
1.9	80	80	80	80	80	80	80	80	80	80	80	80	80	80	80	80	80	80	80	80	80
1.75	60	60	60	60	60	60	60	60	60	60	60	60	60	60	60	60	60	60	60	60	60
1.6	60	60	60	60	60	60	60	60	60	60	60	60	60	60	60	60	60	60	60	60	60
1.45	50	50	50	50	50	50	50	50	50	50	50	50	50	50	50	50	50	50	50	50	50
1.3	50	50	50	50	50	50	50	50	50	50	50	50	50	50	50	50	50	50	50	50	50
1.15	40	40	40	40	40	40	40	40	40	40	40	40	40	40	40	40	40	40	40	40	40
1	40	40	40	40	40	40	40	40	40	40	40	40	40	40	40	40	40	40	40	40	40
0.85	30	30	30	30	30	30	30	30	30	30	30	30	30	30	30	30	30	30	30	30	30
0.7	30	30	30	30	30	30	30	30	30	30	30	30	30	30	30	30	30	30	30	30	30

3. Impedance Measurements

Scanning Impedance Probe

As in all of science, no one researcher's work stands alone in a vacuum; as is said often, we all stand on the shoulders of giants. This work was made possible through the efforts of previous students, and in particular Robert Usiskin, who describes the design, construction, and operation of the scanning impedance probe in his thesis[4]. What follows is a brief explanation of this instrument; for a complete description, please see Dr. Usiskin's thesis.

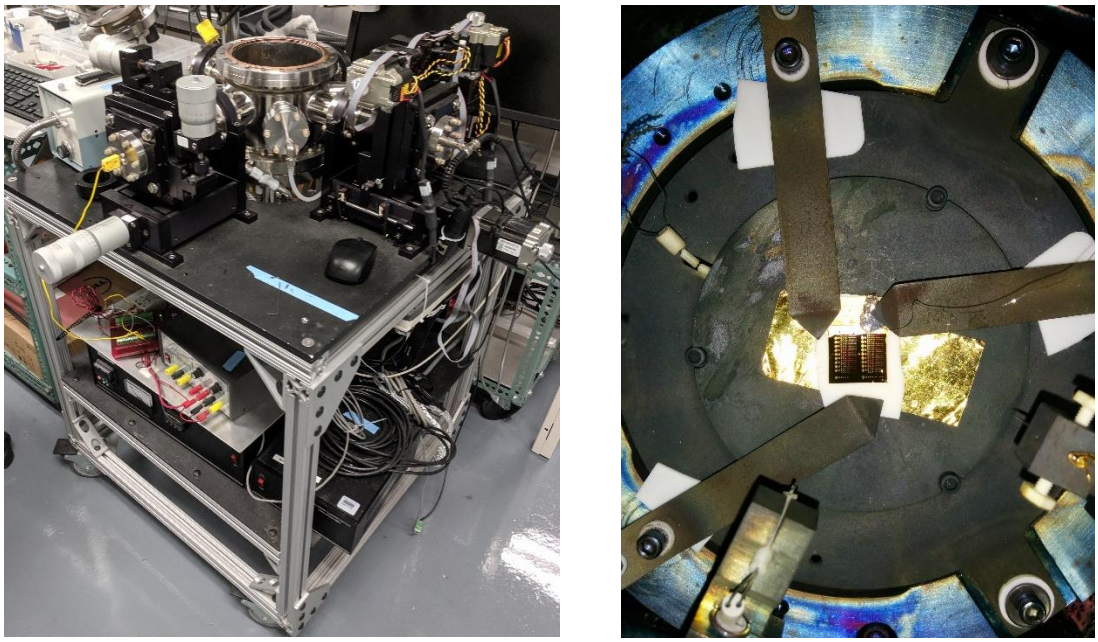

Figure 2-9. Images of the scanning impedance probe system. (left) Exterior view showing manual and robotic manipulators. (right) Top view of stage showing clipped sample.

The scanning environmental impedance probe used in this work consists principally of an environmental chamber with gas inlet and outlet and a stage heated by a $MoSi_2$ heating element. Viewing from above, one observes four large-diameter ports attached to the central cylindrical chamber along the main cardinal directions and four small-diameter ports between each pair of large ports. Two mutually orthogonal arms of the chamber are attached with flexible flanges which permit attached probe arms to move while maintaining a vacuum-tight seal (Figure 2-9). One of these probes uses manual adjustment for motion, while the other uses robotic stepper motors to control its position. The former is attached to a surface thermocouple probe, described in detail later. The latter houses the impedance probe electrode tip which is used to make contact, in serial fashion, with each of the micro-electrodes.

The scanning head contains an assembly designed to hold a tip that makes contact with each of the micro-electrodes. The tip can be seen in the right side of Figure 2-9. The tip is an 80:20 Pt:Ir mixture (Moser) which was found previously to have sufficient hardness to withstand repeated probing while not scratching the surface of the micro-electrodes. The sample is clipped to the heated stage using electronically isolated Inconel clips. A sheet of gold foil is placed between the sample and the stage to improve thermal contact and transport. The counter-electrode wire is clipped onto the sample using one of the Inconel clips.

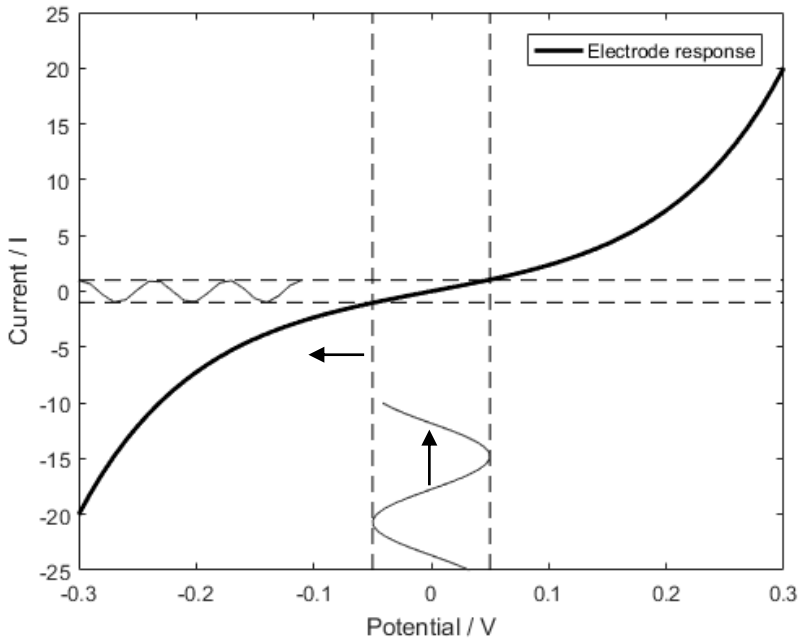

Figure 2-10. Schematic of electrochemical impedance spectroscopy. A sinusoidal voltage perturbation (bottom) is applied to the electrode and the resulting current signal (left) is measured. This schematic represents a measurement at zero bias.

Impedance Spectroscopy

Obtaining precise knowledge and complete understanding of the reaction pathways and mechanisms for these devices is an immense task. Completely describing the interactions of

multiple chemical and electronic species through multiple gas-solid and solid-solid interfaces is exceedingly difficult. While many tools have emerged to make parts of this characterization tractable (including oxygen tracer diffusion[5], secondary ion mass spectroscopy[6], FIB-SEM 3D reconstruction[7]), impedance spectroscopy is the technique chosen for the bulk of this work as it presents the correct mixture of versatility, precision, and throughput needed to characterize a wide range of materials[8-16].

The operating principle of electrochemical ac impedance spectroscopy is that the application of a small sinusoidal perturbation allows measurement of a sufficiently linear region of the electrode response to extract an impedance. Furthermore, reactions proceeding at different rates can be separated by perturbing the driving force for that process on or near its characteristic time scale. Thus, processes with different time scales can be separated by observing their impact on the impedance at different frequencies. A schematic of the operation of ac impedance spectroscopy is shown in **Error! Reference source not found.**. T he sinusoidal voltage perturbation is applied to the electrode, and the resulting current response is measured. The pictured condition is at "zero bias" – note that the resistance changes if a dc bias is applied, as is the case *in operando*.

An example of a measured impedance spectrum is shown in Figure 2-11 on a Nyquist plot (left) and a Bode plot (right). In the Nyquist plot, which plots the real versus the imaginary parts of the impedance spectrum at different frequencies, two distinct arcs appear corresponding to two distinct processes. To make this example more concrete, we might imagine that this corresponds to the measurement of the conductivity of a symmetric fuel cell. The offset of the arcs from the origin would be attributed to the electrolyte conductivity.

The small, high-frequency arc would be attributed to a slower process, such as charge transport at grain boundaries. Finally, the largest arc at lowest frequencies would correspond to the slow kinetics at the electrodes where redox reactions occur. The observed impedance behavior of an electrochemical cell can vary widely based on its properties. For example, in Lai et al[14], the authors discuss how the mixed-conducting properties of ceria in different temperature and oxygen environments leads to different observed behavior. We will see later that for another cathode material, $La_{1-x}Sr_xMnO_3$ (LSM), the impedance spectra adhere to a rather complex physical model.

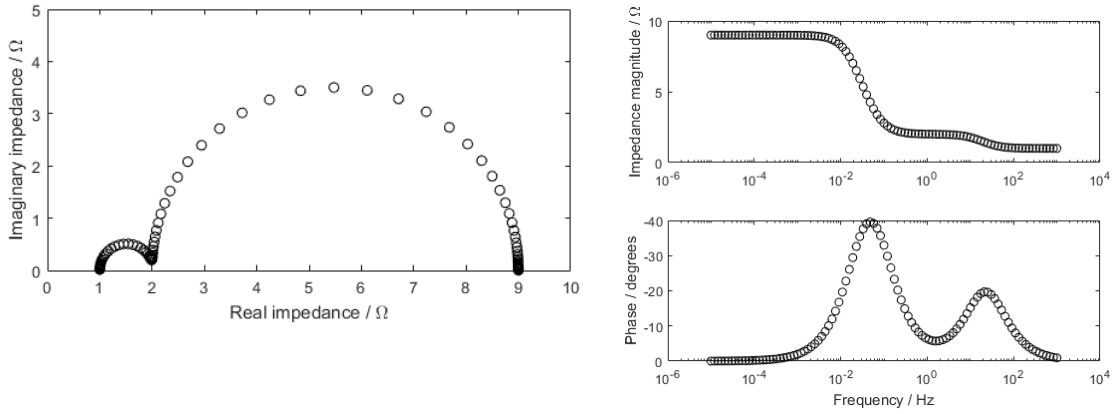

Figure 2-11. (left) Nyquist plot of a measured impedance spectrum. (right) Bode magnitude and phase plots of the same spectrum.

Mathematically, ac impedance spectroscopy is represented in Equation 2.1:

$$Z(\omega) = \frac{V(\omega)}{I(\omega)} = \frac{V_0 e^{i\omega t}}{I e^{i(\omega t + \phi)}} = \frac{V_0}{I} e^{-i\phi} \qquad 2.1$$

where Z is the measured impedance, V_0 is the voltage perturbation, I is the measured current, ω is the frequency, and ϕ is the phase shift of the current response. The magnitude and phase shift of the response can be plotted on a Bode plot, shown on the right side of Figure 2-11.

The top diagram, which shows the magnitude as a function of frequency, directly shows the frequency dependence of the impedance magnitude and helps correctly interpret that the larger arc in the Nyquist plot is associated with low frequencies. The phase plot helps separate the two processes in frequency space by showing where large imaginary impedance values (corresponding to capacitance) peak.

There are multiple geometries suitable for performing AC impedance spectroscopy. The geometry selected for use in this thesis is an asymmetric geometry, as distinct from the more typical symmetric geometry.

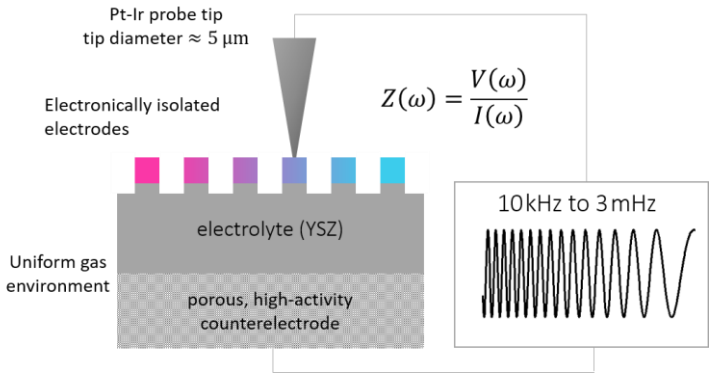

Figure 2-12. Schematic of ac impedance spectroscopy on a gradient film in an asymmetric geometry.

The asymmetric geometry has been used previously to isolate the properties of individual materials[13,17-31]. This technique relies on the fact that since the measured properties of these materials scale with geometry (i.e., the resistance of an electrode decreases as its area increases), engineering a sample in an intentionally asymmetric way can skew the measured properties towards the largest ones. By making a top electrode significantly smaller than its counter-electrode, the measured properties can be attributed almost entirely to the small

electrode. This sense of "smaller" and "entirely" has been formalized by Sasaki et al[17] to depend on the properties of the electrode, electrolyte, and counter-electrode in question.

Positioning the Probe Tip

In the course of obtaining measurements of many microelectrodes, correct positioning of the probe tip became problematic. The initial procedure developed to locate microelectrodes was to measure the positions of three microelectrodes and then predict the positions of the remaining microelectrodes based on the known photolithographic pattern[3] (Figure 2-8). However, small errors in measuring any of these positions would propagate to the entire pattern. To mitigate this problem, a more advanced methodology for locating all microelectrode positions was developed. Specifically, the positions of an arbitrary number of microelectrodes (at least three) are recorded by the user along with the corresponding row and index label. Next, a least-squares fit is performed to the measured positions using the known positions of the pattern as a reference and seven fit parameters including all possible translations (in x, y, and z directions), rotations (about each major axis) and thermal expansion of the lattice. Code for conducting this fitting is included in Appendix B. Use of this particular fitting routine resulted in significantly more accurate dot positioning and fewer impedance scans lost due to poor contact. The order of the microdot measurements was randomized to prevent convolution of time-dependent parameters with position.

4. Data Analysis

Equivalent Circuit Models

The impedance spectra resulting from impedance spectroscopy are interpreted by modelling the physiochemical processes as resistance and capacitance in a model electronic circuit. Many equivalent circuits have been proposed and evaluated for extracting meaningful information from electrochemical systems. However, the fit of a particular model to a measured impedance spectrum is not sufficient to judge whether the model accurately represents physical processes. A more accurate process begins with a physical model of a system and makes simplifying assumptions based on the characteristics of the material being measured.

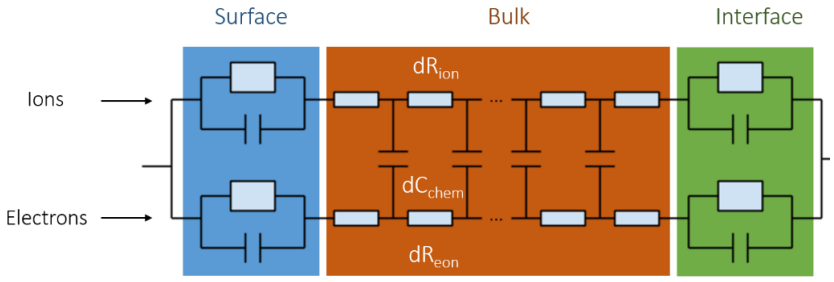

Figure 2-13. Mixed-conducting impedance model.

A mixed conducting model for ions and electrons is constructed as follows, and as shown in **Error! Reference source not found.**. Ionic and electronic conduction are modelled as p arallel paths in a circuit, with corresponding differential resistances R_{ion} and R_{eon}. These parallel conducting paths are coupled by a capacitance C_{chem} termed the chemical capacitance[16]. This chemical capacitance is analogous to , e.g., electrical capacitance $C = dQ/dV$, where simple charge is replaced by any ionic chemical species. This circuit model can then be solved by making simplifying assumptions to reduce the complexity, or by solving mathematical equations as needed[14].

Table 2-4. Examples of model circuits and their impedance formulas.

Model	**Equation**
Resistor	$Z(\omega) = R$ (2.2)
Series RC Circuit	$Z(\omega) = R + \frac{1}{i\omega C}$ (2.3)
Parallel RC Circuit	$Z(\omega) = \frac{R}{1 + i\omega RC}$ (2.4)
Offset RC Circuit	$Z(\omega) = R_1 + \frac{R_2}{1 + i\omega R_2 C}$ (2.5)
Offset RC circuit with constant phase element	$Z(\omega) = R_0 + \frac{R_1}{1 + YR(i\omega)^n}$ (2.6)
Two processes with R/CPE circuits and an offset	$Z(\omega) = R_0 + \frac{R_1}{1 + i\omega R_1 C_1} + \frac{R_2}{1 + i\omega R_2 C_2}$ (2.7)
Baumann Model[24]	$Z(\omega) = \frac{R_s + R_i + i\omega R_i R_s C_s}{1 - \omega^2 R_s C_s R_i C_i + i\omega(R_i C_i + R_s C_i + R_s C_s)}$ (2.8)
Boukamp Model[32]	$Z(\omega) = \frac{R_l + i\omega R_l R_p (C_l + C_p)}{1 - \omega^2 R_l C_l R_p C_p + i\omega\left(R_p C_p + (R_l + R_p) C_l\right)}$ (2.9)
LSM Model[3]	$Z(\omega) = \frac{R_{ion} Z_D + Z_D Z_A a \coth(a)}{R_{ion} + \frac{Z_A Z_D a^2}{R_{ion}} + (Z_A + Z_D) a \coth(a)}$ (2.10) where $Z_D(\omega) = \frac{1}{i\omega C_{eon}^{int}}$ (2.10b) $Z_A(\omega) = \frac{R_{ion}^{surf}}{1 + R_{ion}^{surf} Y_{ion}^{surf} (i\omega)^n}$ (2.10c) $a(\omega) = \sqrt{i\omega R_{ion} C_{chem}}$ (2.10d)

Matlab Fitting Code

To determine fits to impedance spectra for models, several commercial software programs are available, including ZView and Solartron ECS software. However, this software is limited to circuits that can take a constrained physical form or specific pre-defined circuits, and are unable to fit to an arbitrary impedance model. This limitation prevented fitting of impedance spectra collected for LSM microelectrodes[3]. Thus, it was necessary to develop new fitting software capable of fitting to an arbitrary model circuit. A significant contribution to the work on this thesis was the development of such software in MATLAB designed to fit arbitrary impedance models and plot the resulting fitting circuits as a function of arbitrary sample characteristics.

The software uses the non-linear least squares minimization function `lsqnonlin` to obtain the set of parameters that minimize the result of a given function. Multiple circuit models were implemented along with this minimization function in a framework that allowed a user to switch between the model circuit used for fitting. This minimization function also results in a Jacobian matrix of all fitted parameters which can be fed into the `nlparci` function (for non-linear parameter confidence interval) to calculate the error associated with the value of a given fit parameter.

The fitting procedure proceeds as follows. The raw impedance data (frequency, real, and imaginary component) is fed into a generalized function that performs the fitting. This function, `customImpedanceFit`, defines the absolute bounds of the parameters used by each model circuit. For example, resistances and capacitances are bounded such that they are always positive, and the *n* parameter of constant phase elements is bounded from 0 to 1. The

function then accepts a set of starting parameters that are used to guess the initial values of the parameters used to calculate the model circuit. These parameters are normalized before they are fed into `lsqnonlin` so that they are all on the order of 1, since it was observed that feeding in the raw values of resistance and capacitance often yielded poor fitting, likely due to the underlying implementation of the optimization algorithm and the vastly different scale of the values for these quantities (which often vary by more than 10 orders of magnitude). Then, for a given model circuit and these starting parameters, an impedance spectrum is generated and compared to the measured impedance spectra. The residual errors are calculated based on the normalization of each spectrum by the norm of the impedance such that for each frequency point, $Z_{norm}(\omega) = \frac{Z(\omega)}{Z_{re}^2(\omega)+Z_{im}^2(\omega)}$. This weighting by the modulus of the impedance prevents large impedance values at low frequency, which are sometimes orders of magnitude larger than high-frequency data points, from dominating the fit.

5. Experimental challenges

Flowing gas at somewhat reducing conditions (< 0.01 atm O_2) and high temperatures (> 700°C) is problematic for the $MoSi_2$ heater element, as the silicon oxide layer that forms to protect degradation wears away and exposes molybdenum which is subsequently volatilized. Molybdenum is then deposited, in the form of a white crystalline powder, across various surfaces in the system, including the surface of the substrate. While this tends not to impact the measured electrochemical properties (see Rob's paper), it's not a good look.

Previous work had used thermovoltage to estimate the surface temperature. However, it was observed that the temperature drop between the stage and the alumina was larger than the temperature drop between the sample surface and the platinum counter-electrode to which the thermovoltage was referenced. Therefore, despite precise knowledge of sample geometry and the Seebeck coefficient of YSZ, precise measurement of the thermovoltage did not yield accurate measurement of the temperature difference between the stage and the sample.

Accurate temperature measurement also proved difficult. Surface temperature is a difficult quantity to measure accurately. The act of measurement via physical contact with a thermocouple changes the temperature of the surface because the thermocouple acts as a heat-sink. Non-contact measurement, such as with a pyrometer, requires accurate measurement of the emissivity of the sample in the temperature range of interest and detailed knowledge of the optical transmission properties of any viewing windows. For this study, two different techniques were used to address these issues. First, multiple temperature-indicating lacquers (Omega LAQ-0225G – LAQ-1300G) were painted on the surface of the sample after measurement, and the sample was re-heated to experimental temperatures. The transition of the lacquers from opaque to translucent occurs at specific, well-defined temperatures, and this transition was noted and correlated to the surface temperature to develop a calibration curve, albeit sparse and rudimentary. The second technique was to purchase a surface thermocouple (Omega 88106K-RE), a device which consists of thin, flat chromel and almumel sheets welded in a diagonal seam and attached with thin lead wires to the mobile arm of the microprobe. As the thermocouple itself mimicked the surface of the sample, and the lead wires used to connect the thermocouple were as thin as was practical,

this solution provided a reasonably accurate method for measuring surface temperature in-situ. Accurate surface temperature measurement remains an outstanding issue for precise determination of activation energy and benchmarking performance to other microelectrode film studies.

6. References

1 Jiang, S. Development of lanthanum strontium manganite perovskite cathode materials of solid oxide fuel cells: a review. *J Mater Sci* **43**, 6799-6833, doi:10.1007/s10853-008-2966-6 (2008).

2 Pechini, M. P. Method of preparing lead and alkaline earth titanates and niobates and coating method using the same to form a capacitor. USA patent (1967).

3 Usiskin, R. E., Maruyama, S., Kucharczyk, C. J., Takeuchi, I. & Haile, S. M. Probing the reaction pathway in (La0.8Sr0.2)(0.95)MnO3+delta using libraries of thin film microelectrodes. *J Mater Chem A* **3**, 19330-19345, doi:10.1039/c5ta02428e (2015).

4 Usiskin, R. E. *Surface Activity and Bulk Defect Chemistry of Solid Oxide Fuel Cell Cathodes* Doctor of Philosophy thesis, California Institute of Technology, (2015).

5 Navickas, E. *et al.* Fast oxygen exchange and diffusion kinetics of grain boundaries in Sr-doped LaMnO3 thin films. *Phys Chem Chem Phys* **17**, 7659-7669, doi:10.1039/c4cp05421k (2015).

6 Kubicek, M. *et al.* Cation diffusion in La(0.6)Sr(0.4)CoO(3-delta) below 800 degrees C and its relevance for Sr segregation. *Phys Chem Chem Phys* **16**, 2715-2726, doi:10.1039/c3cp51906f (2014).

7 Marinha, D. *et al.* Microstructural 3D Reconstruction and Performance Evaluation of LSCF Cathodes Obtained by Electrostatic Spray Deposition. *Chem Mater* **23**, 5340-5348, doi:Doi 10.1021/Cm2016998 (2011).

8 Im, H. N., Choi, M. B., Singh, B., Lim, D. K. & Song, S. J. Investigation of Oxygen Reduction Reaction on La0.1Sr0.9Co0.8Fe0.2O3-delta Electrode by Electrochemical Impedance Spectroscopy. *J Electrochem Soc* **162**, F728-F735, doi:10.1149/2.0581507jes (2015).

9 Endler-Schuck, C., Joos, J., Niedrig, C., Weber, A. & Ivers-Tiffee, E. The chemical oxygen surface exchange and bulk diffusion coefficient determined by impedance spectroscopy of porous La0.58Sr0.4Co0.2Fe0.8O3 (-) (delta) (LSCF) cathodes. *Solid State Ionics* **269**, 67-79, doi:10.1016/j.ssi.2014.11.018 (2015).

10 Kubicek, M. *et al.* Electrochemical properties of La0.6Sr0.4CoO3−δ thin films investigated by complementary impedance spectroscopy and isotope exchange depth profiling. *Solid State Ionics* **256**, 38-44, doi:10.1016/j.ssi.2013.12.016 (2014).

11 Antunes, R., Jewulski, J. & Golec, T. Full Parametric Characterization of LSM/LSM-YSZ Cathodes by Electrochemical Impedance Spectroscopy. *J Fuel Cell Sci Tech* **11**, doi:10.1115/1.4025533 (2014).

12 Cronin, J. S. *et al.* Effect of Firing Temperature on LSM-YSZ Composite Cathodes: A Combined Three-Dimensional Microstructure and Impedance Spectroscopy Study. *J Electrochem Soc* **159**, B385-B393, doi:Doi 10.1149/2.053204jes (2012).

13 Baumann, F. S., Fleig, J., Habermeier, H. U. & Maier, J. Ba0.5Sr0.5Co0.8Fe0.2O3-delta thin film microelectrodes investigated by impedance spectroscopy. *Solid State Ionics* **177**, 3187-3191, doi:10.1016/j.ssi.2006.07.057 (2006).

14 Lai, W. & Haile, S. M. Impedance spectroscopy as a tool for chemical and electrochemical analysis of mixed conductors: A case study of ceria. *J Am Ceram Soc* **88**, 2979-2997, doi:DOI 10.1111/j.1551-2916.2005.00740.x (2005).

15 Fleig, J. Impedance spectroscopy on solids: The limits of serial equivalent circuit models. *J Electroceram* **13**, 637-644, doi:DOI 10.1007/s10832-004-5170-3 (2004).

16 Jamnik, J. & Maier, J. Generalised equivalent circuits for mass and charge transport: chemical capacitance and its implications. *Phys Chem Chem Phys* **3**, 1668-1678, doi:Doi 10.1039/B100180i (2001).

17 Sasaki, K. A., Hao, Y. & Haile, S. M. Geometrically asymmetric electrodes for probing electrochemical reaction kinetics: a case study of hydrogen at the Pt-CsH2PO4 interface. *Phys Chem Chem Phys* **11**, 8349-8357, doi:Doi 10.1039/B909498a (2009).

18 Brichzin, V., Fleig, J., Habermeier, H. U. & Maier, J. Geometry dependence of cathode polarization in solid oxide fuel cells investigated by defined Sr-doped LaMnO3 microelectrodes. *Electrochem Solid St* **3**, 403-406, doi:Doi 10.1149/1.1391160 (2000).

19 Brichzin, V., Fleig, J., Habermeier, H. U. & Maier, J. Electrode kinetics of SOFC cathodes investigated by using geometrically defined strontium-doped lanthanum manganite microelectrodes. *Schr Fz Jul Energ* **15**, 711-714 (2000).

20 Brichzin, V., Fleig, J., Habermeier, H. U. & Maier, J. Investigation of the cathodic polarization mechanism in SOFCs by means of LSM-microelectrodes. *Solid Oxide Fuel Cells Vii (Sofc Vii)* **2001**, 555-563 (2001).

21 Brichzin, V., Fleig, J., Habermeier, H. U., Cristiani, G. & Maier, J. The geometry dependence of the polarization resistance of Sr-doped LaMnO3 microelectrodes on yttria-stabilized zirconia. *Solid State Ionics* **152**, 499-507, doi:10.1016/S0167-2738(02)00379-X (2002).

22 Fleig, J. Microelectrodes in solid state ionics. *Solid State Ionics* **161**, 279-289, doi:10.1016/S0167-2738(03)00217-0 (2003).

23 Baumann, F. S. *et al.* Strong performance improvement of La0.6Sr0.4Co0.8Fe0.2O3-delta SOFC cathodes by electrochemical activation. *J Electrochem Soc* **152**, A2074-A2079, doi:Doi 10.1149/1.2034529 (2005).

24 Baumann, F. S., Fleig, J., Habermeier, H. U. & Maier, J. Impedance spectroscopic study on well-defined (La,Sr)(Co,Fe)O3-delta model electrodes. *Solid State Ionics* **177**, 1071-1081, doi:DOI 10.1016/j.ssi.2006.02.045 (2006).

25 Fleig, J. *et al.* Thin film microelectrodes in SOFC electrode research. *Fuel Cells* **6**, 284-292, doi:DOI 10.1002/fuce.200500209 (2006).

26 Baumann, F. S. *et al.* Quantitative comparison of mixed conducting SOFC cathode materials by means of thin film model electrodes. *J Electrochem Soc* **154**, B931-B941, doi:Doi 10.1149/1.2752974 (2007).

27 Januschewsky, J., Ahrens, M., Opitz, A., Kubel, F. & Fleig, J. Optimized La0.6Sr0.4CoO3-delta Thin-Film Electrodes with Extremely Fast Oxygen-Reduction Kinetics. *Adv Funct Mater* **19**, 3151-3156, doi:DOI 10.1002/adfm.200900362 (2009).

28 Kubicek, M., Limbeck, A., Fromling, T., Hutter, H. & Fleig, J. Relationship between Cation Segregation and the Electrochemical Oxygen Reduction Kinetics of La0.6Sr0.4CoO3-delta Thin Film Electrodes. *J Electrochem Soc* **158**, B727-B734, doi:10.1149/1.3581114 (2011).

29 Opitz, A. K. *et al.* Thin film cathodes in SOFC research: How to identify oxygen reduction pathways? *Journal of Materials Research* **28**, 2085-2105, doi:Doi 10.1557/Jmr.2013.216 (2013).

30 Kogler, S., Nenning, A., Rupp, G. M., Opitz, A. K. & Fleig, J. Comparison of Electrochemical Properties of La0.6Sr0.4FeO3-delta Thin Film Electrodes: Oxidizing vs. Reducing Conditions. *Journal of the Electrochemical Society* **162**, F317-F326, doi:10.1149/2.0731503jes (2015).

31 Rupp, G. M. *et al.* Surface chemistry of La0.6Sr0.4CoO3-delta thin films and its impact on the oxygen surface exchange resistance. *Journal of Materials Chemistry A* **3**, 22759-22769, doi:10.1039/c5ta05279c (2015).

32 Boukamp, B. A., Hildenbrand, N., Bouwmeester, H. J. M. & Blank, D. H. A. Impedance of thin film cathodes: Thickness and current collector dependence. *Solid State Ionics* **283**, 81-90, doi:10.1016/j.ssi.2015.10.013 (2015).

Chapter 3

TRADITIONAL CATHODE MATERIALS ON OXIDE-ION CONDUCTING ELECTROLYTES

In this chapter, the properties of a state-of-the-art cathode material, $La_{0.6}Sr_{0.4}Co_{1-x}Fe_xO_{3-\delta}$ (LSCF64), on an oxygen-ion conducting electrolyte (YSZ) are investigated using the techniques outlined in Chapter 2.

1. Motivation

Despite, or perhaps due to, the breadth and depth of literature concerning this material family, measurements of materials properties for LSCF64 show substantial variation dependent upon both the measurement technique utilized and the group performing the measurement. For example, due to morphology variation, area-specific resistance measurements of LSC64 with varying microstructure collected by Kilner and Burriel[1] show variation of more than two orders of magnitude. Discrepancies still exist even when morphology is accounted for: in Gao et al.[2], reviewed measurements of k* and D*, the reported surface kinetic parameter and the diffusion constant respectively, are shown to vary by orders of magnitude for nominally identical LSCF64 compositions.

Previous attempts to remove morphology variation in thin film studies have been attempted, as have microelectrode studies on LSCF[3-7] though in these and other thin-film studies different equivalent circuits are fit to the measured impedance data which artificially varies the calculated value for physical parameters. For example, for LSCF64 thin-film microelectrodes with a gadolinia-doped ceria interlayer, Crumlin et al.[8] use an R(RQ)(RQ)

circuit model consisting of two sets of parallel resistors and constant phase elements in series with an offset resistor, whereas for thin-film LSCF6428 with a gadolinia-doped ceria interlayer, Boukamp et al.[9,10] fit to a derived generic diffusion model circuit. In a study of LSCF64 microelectrodes, Baumann et al.[4] use a model circuit derived from a parallel transmission model[11] with further simplifications assuming fast ionic and electronic transport. The authors also comment on the instability of measured parameters and estimate that experimental error is approximately a factor of 3 between upper and lower limits because of the large scatter observed between measurements of nominally identical microelectrodes.

Thus, an experiment that can demonstrate stable, repeatable, accurate, and precise measurements of different electrode compositions under fuel cell-relevant conditions, so far lacking in the literature, is vital to understanding how material parameters vary with composition.

2. Library preparation and preliminary characterization

Targets for pulsed laser deposition were prepared by a solid state reaction method. Appropriate stoichiometric amounts of $LaCO_3$ (99.9%, Alfa Aesar), $SrCo_3$ (99.99%, Alfa Aesar), Co_3O_4 (99.7%, Alfa Aesar), and Fe_2O_3 (99.9%, Alfa Aesar) powders were ball milled for 8h using ethanol and yttria-stabilized zirconia balls as the milling medium. The resulting powder was sieved, then uniaxially pressed into a ~25 mm diameter pellet at 20 MPa. The resulting green pellet was calcined at 800°C for 8 hours. The calcined pellet was crushed, the milling and pressing steps were repeated, and sintering was carried out at 1200°C for 8 hr. To create a 20% samarium-doped ceria (SDC20) target, as-received commercial powder was compacted in the same manner as described above and directly sintered at 1600°C for 24 hr.

Phase purity of the pellets was confirmed by X-ray diffraction (Figure 3-14, left) and composition was measured by energy-dispersive X-ray spectroscopy (EDS, Oxford INCAx-act) in a scanning electron microscope (SEM, Hitachi S-3400N-II).

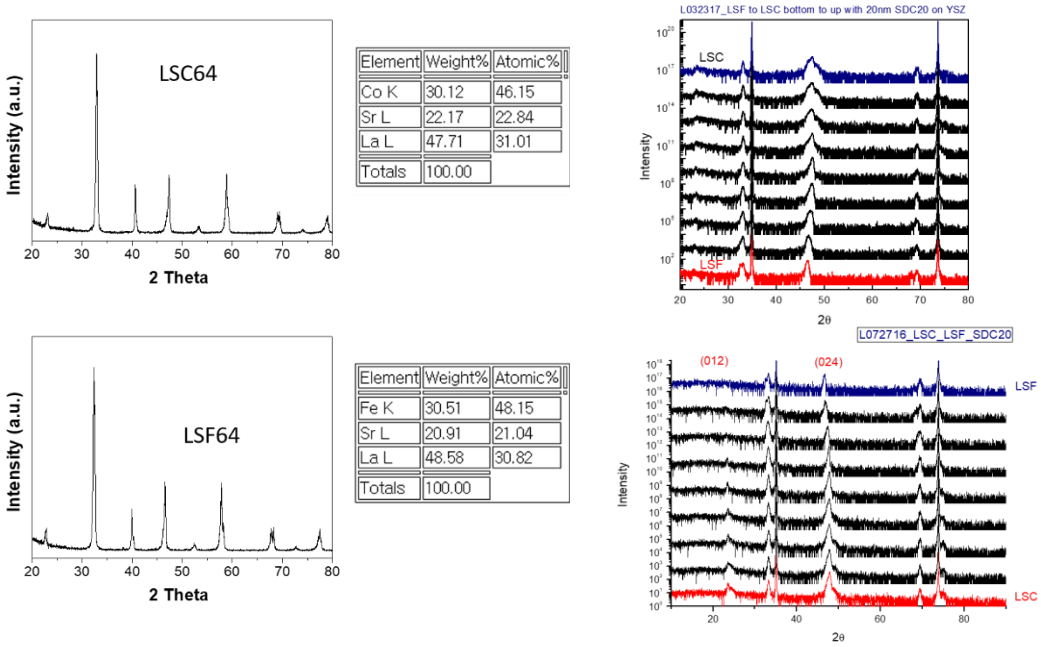

Figure 3-14. (left) X-ray diffraction patterns of PLD targets of LSC and LSF. (right) Thin-film X-ray diffraction patterns of deposited film gradients for both libraries.

Pulsed laser deposition was used to create two compositionally graded sample libraries (hereafter designated Library i and Library ii), employing a methodology described previously, in which a traveling shutter results in sequential, graded deposition from targets with chemistries corresponding to the end-member compositions.[12,13] Films were grown on 10 mm W x 5 mm D x 500 µm H (100)-oriented 8 mol%-Y_2O_3-ZrO_2 (8YSZ) substrates (MTI). Prior to LSCF deposition, a SDC20 interlayer, 20 nm in thickness, was deposited to

serve as an ion-conducting reaction barrier. All films were deposited with a KrF-excimer laser at a power of 22 mJ and a 5 Hz pulse rate under 30 mTorr oxygen partial pressure, with a post-anneal at 600°C. Library i was designed with a linear composition gradient, whereas the composition gradient of Library ii was skewed for finer spacings in the cobalt-dominant composition range by depositing a thicker layer of LSC than LSF on each shutter pass.

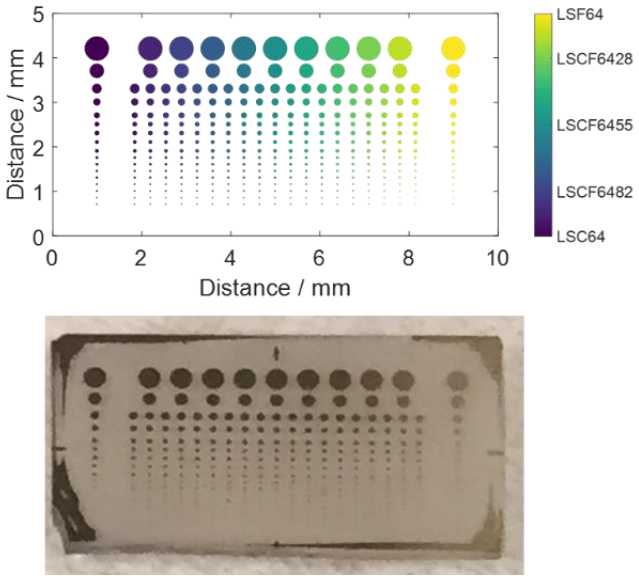

Figure 3-15. Schematic (top) and image (bottom) of LSCF composition library.

Thin-film X-ray diffraction (Figure 3-14, right) shows the films to be crystalline, with a slight lattice parameter increase from LSC to LSF as expected due to the replacement of cobalt with larger iron atoms[14]. Atomic force microscopy (AFM, TKTK from UMD) reveals the films are smooth and crack-free, with rectangular grains approximately 40 nm x 80 nm in the LSF film that transition into grains with an even aspect ratio (approximately 40 nm x 40 nm) in the LSC film (Figure 3-16). It has been postulated previously[13] that grain boundaries may serve as active sites for oxygen reduction, and this difference in surface grain structure corresponding to a ~33% increase in surface grain boundary density should be

incorporated into any observed difference in the electrochemical activity of the films. However, as shown later, the observed variation in surface electrochemical resistance exceeds this value, and grain boundary density is therefore determined to be insufficient to explain the observed difference despite the contribution it may provide.

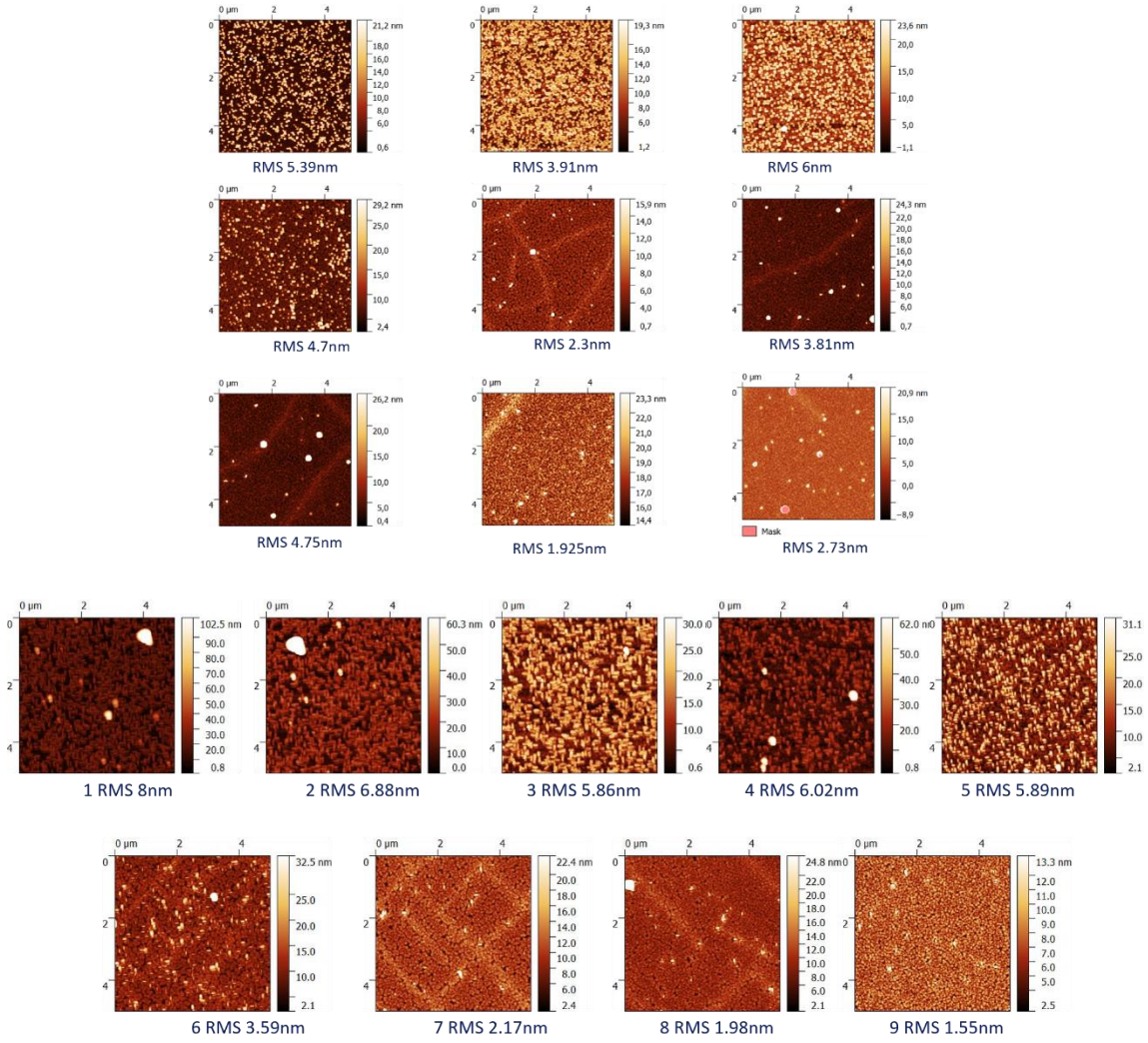

Figure 3-16. Atomic-force microscopy images of the post-deposition surface of the LSF64 film (top left) through the LSF64 film (bottom right) of Library i (top) and Library ii (bottom) in ~10% composition steps. The rms roughness of each surface is given indicating flat, crack-free surfaces.

Following these physical characterization procedures, the film was patterned using photolithography and ion milling to create a library of circular microelectrodes spanning 21 unique compositions and ranging in diameter from 500 µm to 30 µm, though only microelectrodes with a 100 µm or larger diameter were electrochemically probed. A sample schematic and image of Library i is shown in Figure 3-15. For electrochemical studies, the YSZ supported libraries were adhered to an alumina substrate using porous platinum paste (Heraeus, CL11-5349) and fired for 1 h at 800°C ramped up and down at 1°C/min. The samples were then clamped onto the high-temperature stage in the scanning electrochemical impedance probe chamber, and the circuit was closed by clamping a counter-electrode wire to the platinum paste.

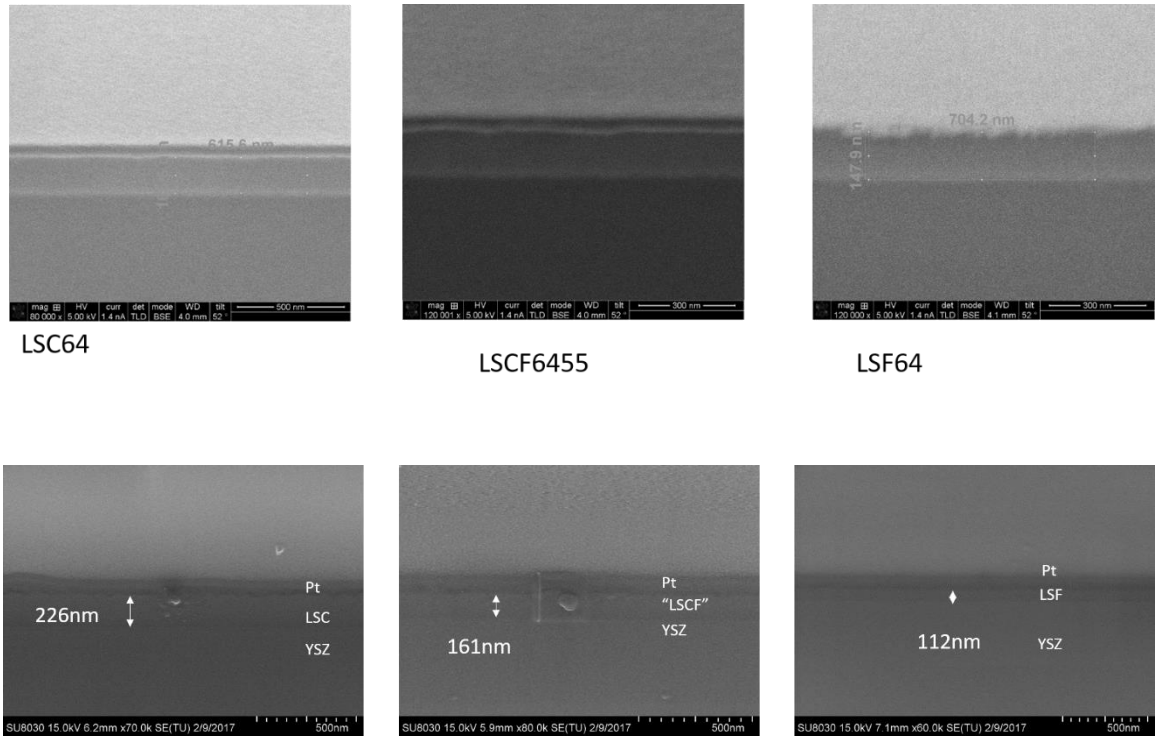

Figure 3-17. FIB-SEM cross-sectional images of top) Library i and bottom) Library ii showing variation in thickness between the LSC64 (left) and LSF64 (right) films.

After completion of the electrochemical measurements (described below), further physical characterization was carried out by cross-sectional FIB-SEM (FEI Helios Nanolab) and chemical analysis was performed by EDS-SEM (Oxford INCAx-act, Hitachi S3400N-II). The Library i film was found to have an average film thickness of 190 nm with a 10% variation across the film (Figure 3-17) with an approximately linear composition profile (Figure 3-18). A film grown in a manner identical to Library ii was found to have a thickness gradient, being 220 nm thick at the LSC end and 110 nm thick at the LSF end (Figure 3-19). This gradient fully accounts for the experimentally measured non-linear compositional profile.

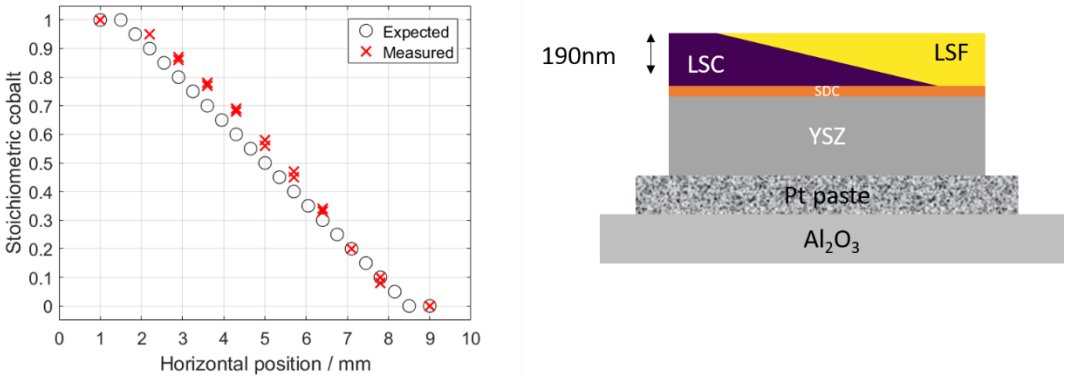

Figure 3-18. Schematic and measured composition for Library i. Composition measured by EDS as a function of horizontal position (red X's) and expected values for a perfect linear gradient (open circles).

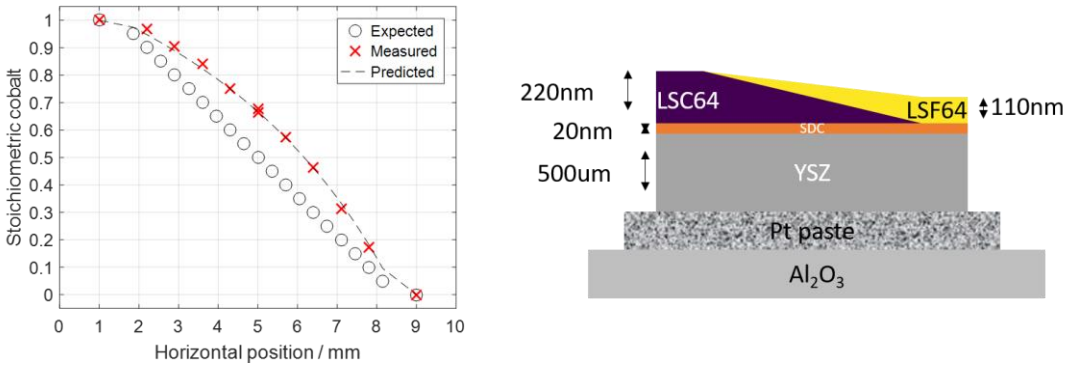

Figure 3-19. Schematic and measured composition for Library ii. Composition measured by EDS as a function of horizontal position (red X's) and expected values for a perfect linear gradient (open circles). The dashed line shows a prediction for the composition profile given the uneven thicknesses of each film.

3. Electrochemical characterization

Impedance measurements in scanning impedance probe

Impedance measurements were carried out in a custom-designed scanning impedance probe station described previously.[13] Impedance data were collected over a frequency range of 10 kHz to 10 mHz (Bio-Logic SP-200), with the lowest frequency for any particular scan adjusted in real time according to the characteristic frequency of the low-frequency electrochemical response. This technique was applied in the following manner: once a maximum along the imaginary axis was detected below a sufficiently low frequency (typically 1 Hz), the impedance analyzer was programmed to measure an additional half-decade in frequency before terminating the measurement. The number of time-consuming low-frequency measurements was therefore reduced.

Measurements were performed at film temperatures ranging from 600-675°C and oxygen atmospheres ranging from 0.04 – 1 atm O_2, balance argon. Gas mixtures were obtained by mixing pure O_2, pure Ar, and 0.1% O_2 balance Ar using mass flow controllers (Aera), with flow rates between 100 sccm (at 1 atm O_2) and 400 sccm (at 0.04 atm). Each library was first equilibrated at 650°C and 1 atm O_2 for 24 hours before measurement. Subsequent to this initial period, at each temperature and p_{O_2} condition each of the 97 microelectrodes with a diameter of 100 μm or greater was measured. At the end of the experiment, measurements at the original condition of 650°C and 1 atm O_2 were repeated to evaluate the possibility of film evolution contributing to observed trends. The libraries were equilibrated for two hours after each change in condition, and the order in which micro-dots were measured was randomized at each condition to prevent any convolution of measured parameters with time. For technical

reasons, Library ii was studied over a wider range of environmental conditions than Library i.

After the measurements were completed, the temperature of the microdots, which are heated through the YSZ substrate, was calibrated using Library ii in conjunction with temperature-indicating lacquer (Omega LAQ-1300G). The lacquer was painted onto the surface of the sample, and its transition from opaque to translucent, which occurs upon reaching a temperature of 704 °C, was tracked. This procedure indicated a 100 °C difference between the stage temperature and the surface temperature of the sample at this transition, and a fixed correction factor of 100 °C is applied to the reported temperatures. Upon removing the lacquer from the sample, the film was damaged, precluding post-measurement analysis; for this reason post-measurement characterization of Library ii features is performed on an identical sample prepared at the same time but not electrochemically measured.

Impedance spectra fitting

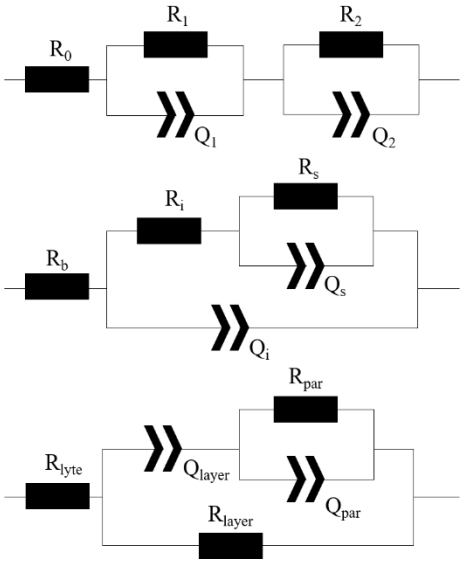

Figure 3-20. (a) R(RQ)(RQ) circuit (after Crumlin et al.). (b) Circuit derived from transmission line model after Baumann et al. (c) Model from Boukamp et al.

The resulting impedance data were analyzed by equivalent circuit fitting using nonlinear least-squares fitting MATLAB code developed in house. The suitability of three different equivalent circuits, shown in Figure 3-20,was examined: (1) an R(RQ)(RQ) circuit, where Q is a constant phase element characterized by parameters Q_0 and n with impedance $Z_Q(\omega) = (Q_0(i\omega)^n)^{-1}$, and (RQ) indicates a resistor and constant phase element in parallel; (2) the circuit described by Baumann et al.[4]; and (3) the circuit described by Boukamp et al.[9] A quantitative goodness-of-fit, *g*, defined as the sum of squares of normalized residuals, Eq. #, was used to evaluate the suitability of the circuit models:

$$g = \sum_i \left(\frac{Z_{re}(\omega_i) - Z_{re}^{fit}(\omega_i)}{Z_{re}(\omega_i)} \right)^2 + \left(\frac{Z_{im}(\omega_i) - Z_{im}^{fit}(\omega_i)}{Z_{im}(\omega_i)} \right)^2 \qquad (3.1)$$

where Z_{re} and Z_{im} are the real and imaginary components of the impedance, superscript 'fit' indicates the computed values, and ω_i is the frequency of the i^{th} element. This formalism

implies that error at high frequency and low frequency are equally weighted, with lower *g* indicating a better fit. The error of the fit parameters is calculated from the Jacobian resulting from the least-squares fit. All error bars shown in this work are the estimated 1σ confidence interval, with errors added in quadrature when values are averaged together.

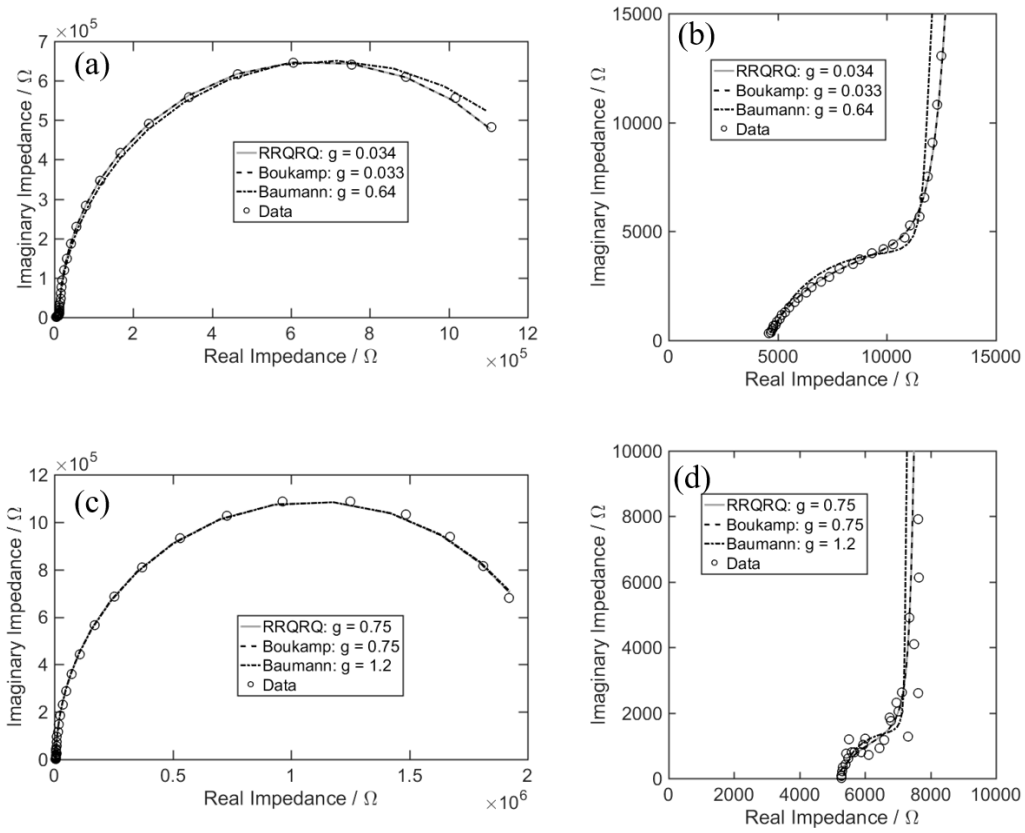

Figure 3-21. Impedance spectra for a 200μm LSCF64 microdot electrode a) in Library i with magnification in b) and c) Library ii with magnification in d) measured at 600°C and 1 atm pO2 fitted to various model circuits.

In all cases, fits were performed with the substitution of constant phase elements for capacitors, thus allowing capacitive processes to deviate from ideality. As mentioned above, doing so renders each of the three circuits mathematically distinct. Examples of model fits to

data from both libraries are shown in Figure 3-21. The R(RQ)(RQ) circuit and the Boukamp circuit resulted in nearly identical fitting parameters and equally good fits, whereas the Baumann circuit yielded different values and higher variance. The distinction between the Baumann and the other two circuits was higher for Library i, for which a distinct high frequency feature is evident in addition to the main low frequency response, than Library ii, for which the high frequency response is barely visible. The suppression of this high-frequency feature in Library ii limited the impact of the interfacial processes on the fit, and the Baumann circuit yielded fits with lower *g* for this library. For Library i, the value of *g* for the Baumann circuit is generally about an order of magnitude higher than that for the R(RQ)(RQ) circuit or the Boukamp circuit and the fits for the latter two circuits are somewhat more visually satisfactory.,

It therefore appears that, though the Baumann circuit was physically derived, the assumptions that led to its form are either not valid or otherwise violated for a system with a doped ceria interlayer, and that, as Boukamp observed, the electronic double-layer capacitance is negligible. Mathematically, the poor fitting results from the coupling of the *n* parameter of the constant phase element representing electronic double-layer capacitance to the parameters controlling the low-frequency arc. In contrast, as discussed above the Boukamp circuit appears practically identical in fit and the resulting fitting parameters to the R(RQ)(RQ) circuit. In fact, as is shown in Appendix A, if one resistance is significantly larger than the other, as is the case here, the values for the Boukamp circuit approach those of the R(RQ)(RQ) circuit. Given the similarity of the Boukamp circuit to the R(RQ)(RQ) circuit in the range of parameters investigated, it is not clear whether the Boukamp circuit represents a physically meaningful set of assumptions or whether it is well-fitting by

coincidence. The remainder of this work utilizes the fit parameters obtained for an R(RQ)(RQ) model circuit with the low-frequency arc attributed to electrochemical resistance and chemical capacitance and the high-frequency arc attributed to interfacial processes.

4. Results and Discussion

General impedance features

Impedance spectra collected from 200 μm diameter microelectrodes in Library i across the entire composition regime at 600°C and a p_{O_2} of 1 atm are shown in Figure 3-22 in the form of Nyquist and Bode plots. In the Nyquist representation, the spectra display a high-frequency offset, a very small high-frequency arc, and a large low-frequency arc. The high-frequency offset is primarily due to the resistance of the YSZ electrolyte. The magnitude of the high-frequency arc is particularly small in comparison to what has been reported by Baumann et al.[4], suggesting this feature has been suppressed by the addition of the SDC interlayer. The large low-frequency arc is attributed to the electrochemical reaction resistance, and a monotonic decrease in this resistance with increasing Co content is immediately evident. The least-squares fits derived from the R(RQ)(RQ) circuit model are shown as solid lines through the points and show excellent agreement to the measured data points.

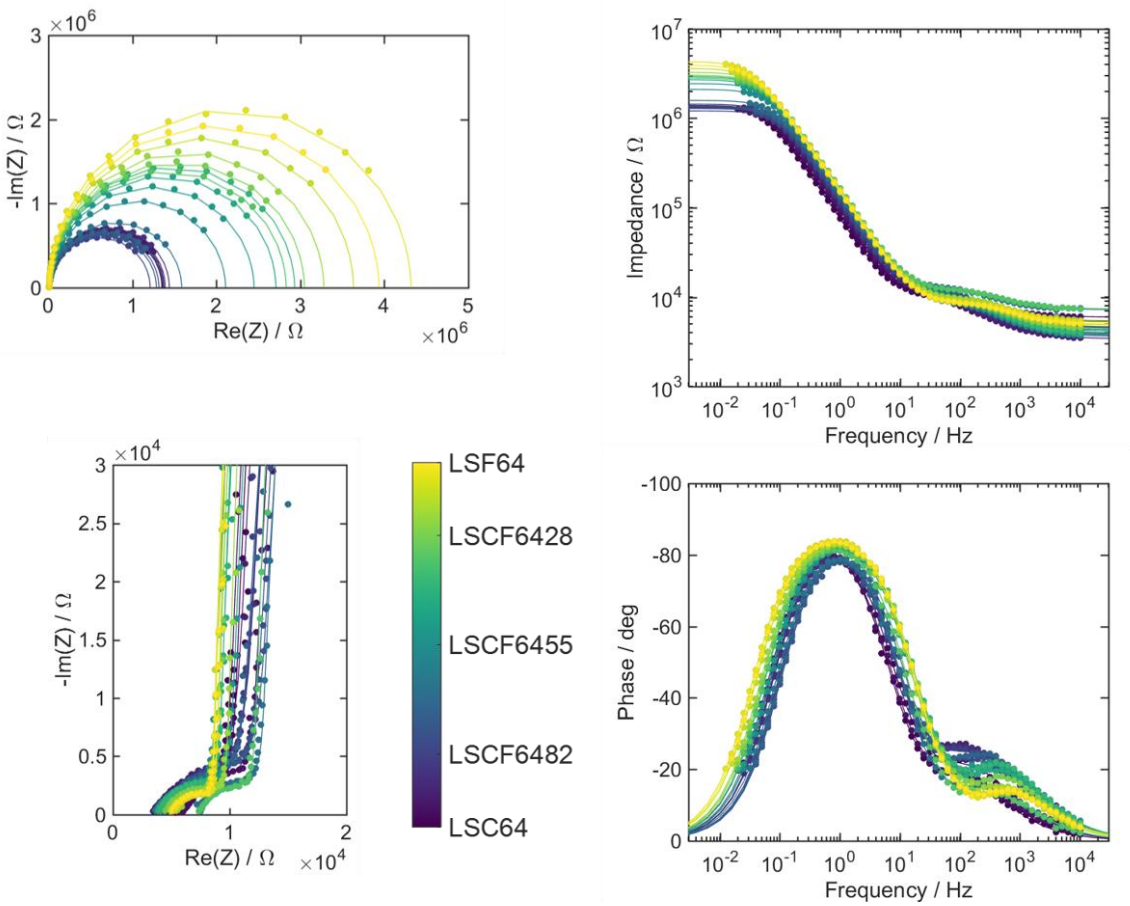

Figure 3-22. (a) Nyquist plot of impedance spectra from 200 µm diameter LSCF microelectrodes in Library i, taken at 600°C under 1 atm O2. Solid lines indicate fit to R(RQ)(RQ) model circuit. Color corresponds to composition as shown in color bar.

The fit parameters derived from least-squares fitting to the RRQRQ circuit model are shown for Library i in Figure 3-23. The data markers schematically represent the microelectrode associated with the data point, i.e., the size and color of the data marker correspond respectively to the diameter and composition of the microelectrode it represents. These figures confirm quantitatively what was shown qualitatively in Figure 3-22, namely the

increase in electrochemical resistance with increasing iron content. In addition, an increase in capacitance is shown with increasing cobalt content.

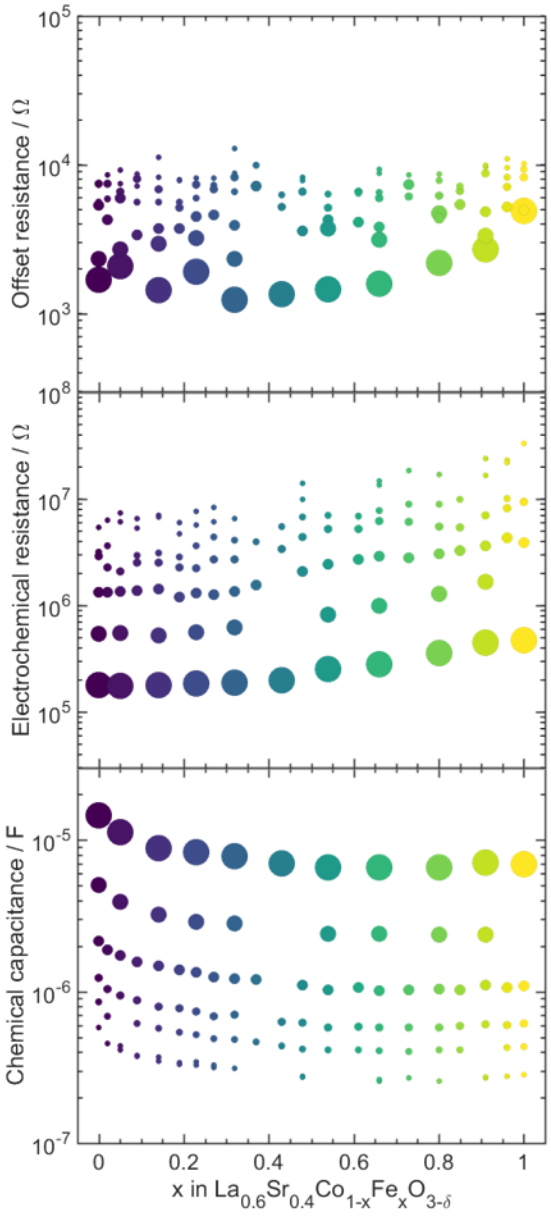

Figure 3-23. Parameters resulting from fitting impedance data obtained at a film temperature of 600°C and 1 atm O2 to an R(RQ)(RQ) circuit as a function of composition: (a) high frequency offset resistance; (b) electrochemical resistance; and (c) chemical capacitance. Data marker diameters correspond to the diameter of the measured microelectrode (from 500 to 100 um), while colors correspond to microelectrode composition.

The offset resistance values show large scatter, a result of the automated process of making contact with a microelectrode. To prevent dot damage, the probe tip is lowered in small

increments until contact is detected by measuring a sufficiently low impedance spectrum. Due to slight variations in dot height and motor position, contact of the probe tip to the micro-dot varies with microdot location and this has a significant effect on the measured offset resistance. Despite this noise, there is a noticeable trend of increasing offset resistance with iron content for the 500μm micro-dot electrodes. This is likely the result of sheet resistance, as LSCF64 has been shown to exhibit metallic conductivity in the cobalt-dominant regime and semi-conducting behavior in the iron-dominant regime[15]. While this may have an effect on the measured electrochemical resistance for the largest micro-electrodes, the smaller micro-dots do not exhibit this behavior and are likely unaffected. Hence, we will ignore the effects of sheet resistance when considering these results, and for comparisons between compositions will use an appropriately normalized average of values from all micro-dot electrodes of a given composition. Before discussing in depth the compositional trends, we provide an assessment of the stability and evaluate the geometric trends.

Stability

To evaluate the stability of these measured parameters, Library ii was subjected to measurement at 650°C and 1 atm O_2 after 24 hours of equilibration and again after 120 hours of continuous testing under other environmental conditions. Figure 3-24 shows the results of this repeated measurement, with the original values shown with open circles and repeat measurements show in filled circles. There is a small increase in the measured electrochemical reaction resistance of, on average, 13%, and nearly no detectable change in the total capacitance, indicating good stability over the entire course of the measurement. Given the sometimes severe degradation observed in some studies[7], it is likely that the ceria performs adequately as a reaction barrier between LSCF64 and 8YSZ, and that if surface degradation via strontium segregation does occur, it is sufficiently slow in the window of the measurement to relate values measured at different times to one another. Sufficient, in this

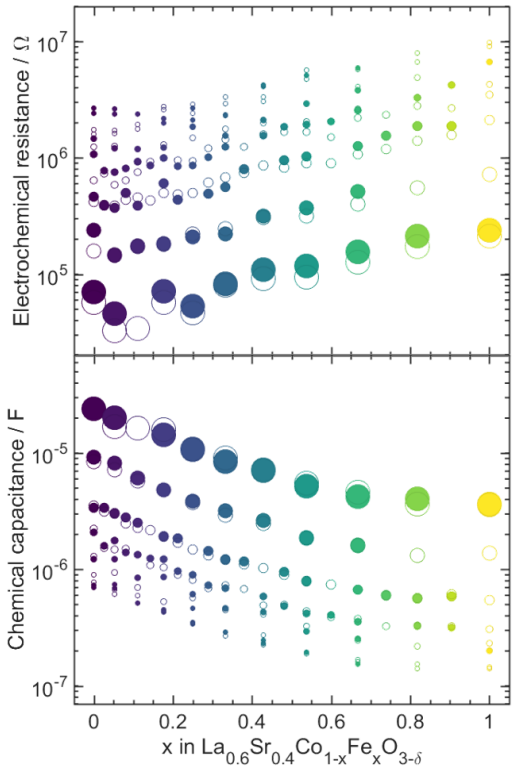

Figure 3-24. Library stability. Initial (open circles) and final (filled circles) values, after 24 hours and 120 hours under environmental conditions respectively, of electrochemical properties of LSCF (Library ii) as a function of composition at a film temperature of 650°C and 1 atm O2 obtained from fitting impedance data to an R(RQ)

case, means that the observed degradation is significantly less than the observed difference between composition end-members and that the degradation appears uniform.

Geometric variation

As in other studies, microelectrode geometry variation is used to determine the dominant electrochemical pathway through the scaling of electrochemical resistance with diameter. In particular, plotting various fit parameters as a function of diameter on a log-log scale yields the power law dependence of that fit parameter on geometry. Figure 3-25 shows such plots for offset resistance, electrochemical resistance, and chemical capacitance for Library i at 675°C and 1 atm O_2. For offset resistance, a slope of negative one is expected from the Newman equation[16,17], and the measured slopes broadly agree with this relationship. For electrochemical resistance, we expect a slope of -2 if the dominant electrochemical process occurs through the surface and a slope of -1 if it occurs at the triple-phase boundary. We

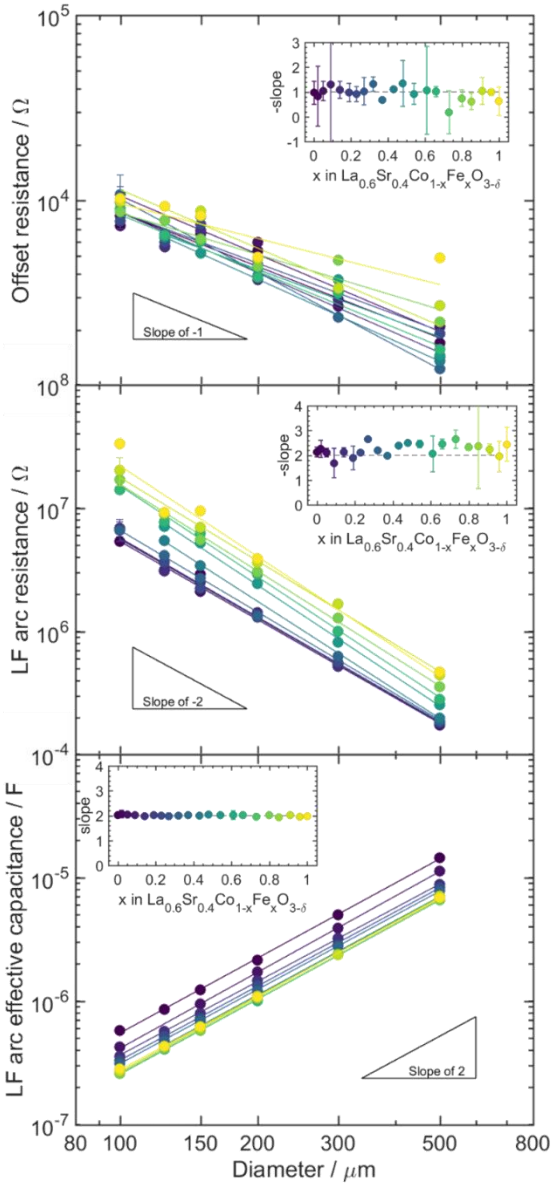

Figure 3-25. Diameter dependence. Electrochemical properties of LSCF (Library i) as a function of film diameter shown as double-logarithmic plots, at a film temperature of 600 °C and atmosphere of 1 atm pO2, obtained from fitting impedance data to an R(RQ)(RQ) circuit: (a) high frequency off-set resistance; (b) electrochemical resistance; and (c) chemical capacitance. Insets in each panel show absolute value of the slope of the linear best fit line to the data on a double logarithmic scale as a function of composition.

indeed observe a slope uniformly near -2, though slightly more negative due to a cooling effect induced by the tip on the microelectrode affecting smaller micro-dots more so than larger micro-dots and thus artificially increasing the measured resistance of smaller-diameter micro-dots[13]. The finding that LSCF in a thin-film configuration is two-phase boundary dominant agrees well with other literature results[3,18].

In previous thin-film studies,[19,20] the total capacitance has been shown to be comprised largely of the chemical capacitance for these mixed conducting materials. This chemical capacitance results from the coupling of the ion- and electron- conducting rails in the model circuit[11], and is given for each conducting species as[21]

$$C_{chem,i} = \frac{(z_i e)^2}{k_B T} c_i V \; ; C_{chem} = \left(\sum_i C_{chem,i}^{-1} \right)^{-1} \tag{3.2}$$

where c_i is the concentration for the i^{th} conducting species and the other variables have their usual meanings. The chemical capacitance is a volumetric quantity and is expected in this case to scale with the area of the microdot electrodes. The observed slope of precisely two for all compositions confirms this relationship and provides further evidence that the total capacitance for the low-frequency arc is almost entirely attributable to chemical capacitance.

In the following results, fit parameters are averaged together by their appropriate normalized value (normalized by area for resistance and by volume for capacitance) across multiple microelectrodes with nominally identical compositions. This averaging serves to ameliorate the difference in the tip cooling effect observed by the deviation of the slope from -2 and therefore include the resulting variation as a systematic uncertainty. As the error from fitting for individual spectra is typically quite small, the error calculated by averaging together the error from multiple microelectrodes in quadrature should result in a more accurate estimate of the total error.

Surface reaction resistance

Figure 3-26 shows the dependence on composition for both libraries measured under 1 atm O_2. For both libraries, the surface reaction resistance monotonically increases from LSC64 to LSF64, with LSF64 about four times more resistive (and hence less active) than LSC64. This factor of four exceeds the difference expected due to increase in grain boundary density alone, if indeed the grain boundaries are the primary active sites for LSCF64, and thus a difference in the inherent activity of these compounds is implied. Furthermore, in the measured temperature range LSC64 is more than then times as electronically conductive as LSF64,[22] a difference more than twice as large as that observed for activity. This result is consistent with what would be observed for strontium segregation which limits the electronic (and ionic) conductivity on the surface, and could also explain the large variation observed in other thin film studies. If films are not given adequate time to stabilize before measurement, the degree of segregation may vary and, along with it, the measured activity.

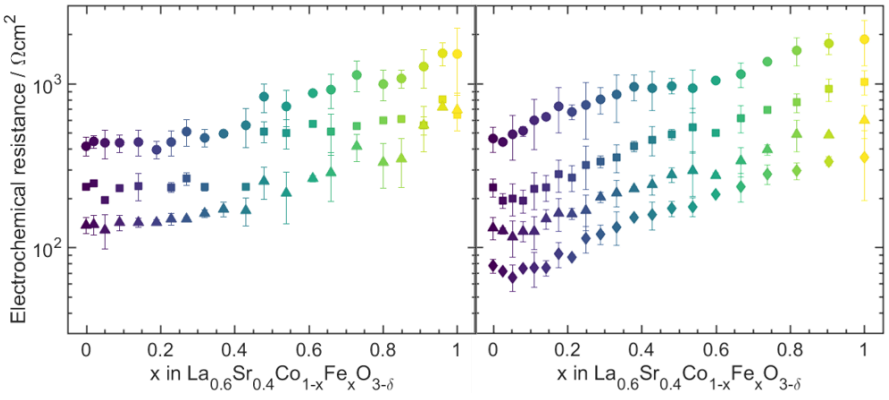

Figure 3-26. Comparison of the area-specific electrochemical resistance of LSCF at 600°C (●), 625°C (■), 650°C (▲), and 675°C (◆) and 1 atm O2 obtained for both libraries. Plotted points are averaged over all microelectrodes with the same composition. (left) Library i; (right) Library ii.

The effectiveness of film synthesis and characterization under identical conditions in minimizing sample-to-sample variation of measured parameters is clearly evident from the comparison of results from both libraries, which show broad agreement in both magnitude and trend across the entire composition range. These results present, to the best of our knowledge, the highest-resolution data on the activity of LSCF64 as a function of cobalt content. In principle, these results can be used to make precise trade-offs in device design.

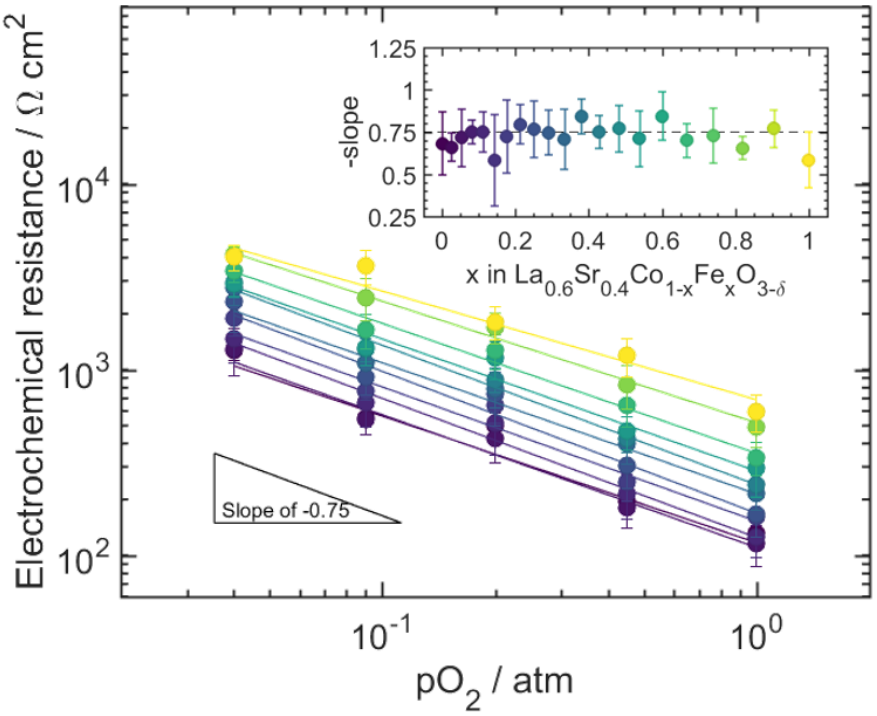

Figure 3-27. Oxygen dependence. Area-normalized electrochemical resistance for Library ii as a function of oxygen partial pressure shown as double-logarithmic plots, at a film temperature of 650 °C. Inset shows slope as a function of composition, with a guideline at ¾. Color corresponds to microelectrode composition. Plotted values are averaged over multiple microelectrodes with the same composition.

For example, the effect of a 5% change in cobalt content on the performance of a fuel cell can be modelled and calculated when trading off activity for thermal expansion coefficient matching.

Included in the systematic variation of environmental conditions were changes in p_{O_2} and temperature which can be used to differentiate rate-limiting reaction mechanisms. In particular, trends in area-specific resistance with p_{O_2} can be used to determine mechanistic information[23]. Figure 3-27 shows the dependence of the area-specific as a function of p_{O_2}. A measured slope around -0.75 agrees with previous results and suggests that diatomic oxygen species are involved in the rate-determining step and is consistent with values measured for other LSCF compounds.[23] In addition, since the trend of resistance with p_{O_2} remains

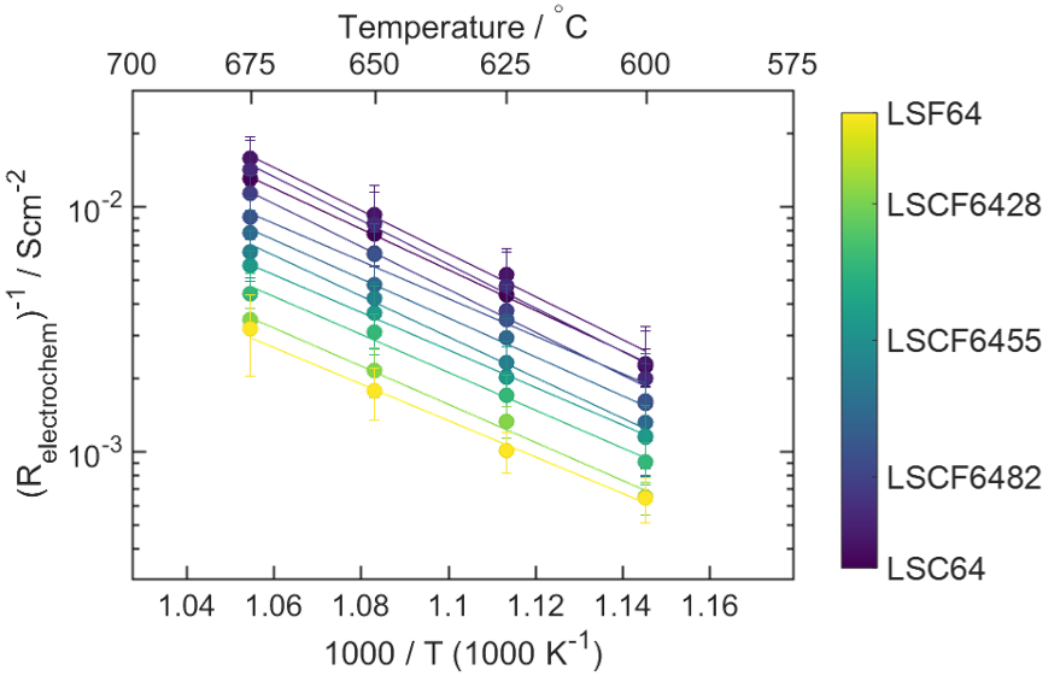

Figure 3-28. Arrhenius behavior. Temperature dependence of electrode resistance in LSCF at 1 atm pO2.

consistent across all compositions, it does not appear as though the rate-limiting step for the dominant pathway is changing, or at the very least show that if a change does occur, the rate-limiting step still involves diatomic oxygen.

The Arrhenius dependence of the area-specific activity (the inverse of the resistance) is plotted in Figure 3-28, along with the calculated activation energies and pre-exponential factors. While the cobalt-dominant compositions demonstrate slightly higher activation energies than the iron-dominant compositions, the activation energies are generally found to be between 1.4 and 2.1 eV in good agreement with those found in the literature (Table 3-1). However, we find the opposite trend of Baumann et al., who found that LSF64 exhibits a higher activation energy than LSC64. Indeed, *a priori* a low activation energy is desired so that resistance increase at lower temperatures is limited, though in this case is shown to be insufficient as the low activation energy for LSF64 is paired with a small pre-exponential factor that dominates in the investigated temperature range.

Further parsing of these results yields an intriguing correlation between the activation energy and pre-exponential factor, shown in Figure 3-29. This relationship, observed as a linear correlation of E_a, the activation energy, and ln(A), the log of the Arrhenius pre-factor, is consistent with the Cremer-Constable compensation relation[24] observed for multiple catalyst compositions across many different reactions. This relation is thought to arise, at least in part, from surface coverage of adsorbed species – the "compensation" between observed activation energy and prefactor comes directly from the tradeoff between the concentration of adsorbed species on the surface and the availability of reaction sites. Thus, according to

Bond et al.[24], the measured activation energies are likely only apparent activation energies that must be converted into true activation energies by taking into account the concentration of occupied surface reactant sites. Given the empirical nature of the relation and the many possible suggested interpretations, we do not attempt to draw any physio-chemical conclusions from this observation. This relation, however, does imply a so-called "isokinetic" temperature at which the values of resistance for all materials will be equal. This temperature is obtained by linearly fitting the Cremer-Constable plot of ln A versus E_a and equating the slope to $\frac{1}{k_B T}$. The isokinetic temperature for LSCF64 is calculated to be

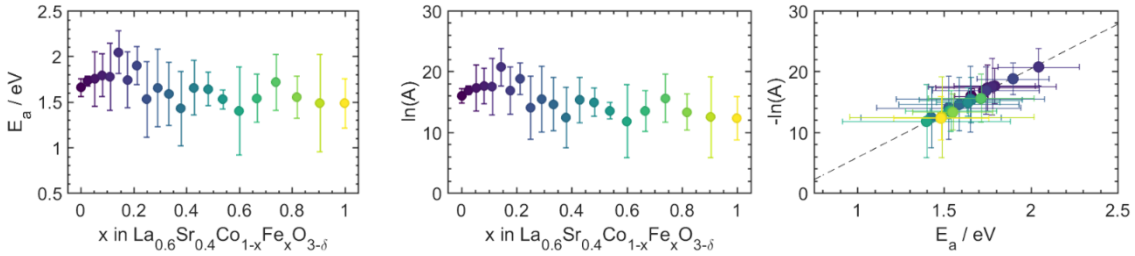

Figure 3-29. (left) activation energy and (middle) pre-exponential factor as functions of composition determined from Arrhenius scaling. Plotted values are averaged over multiple microelectrodes with the same composition. (right) Log of the pre-exponential factor versus activation energy.

approximately 510°C, at which temperature the electrochemical resistance for these materials is equal and below which, barring a change in mechanism, LSF64 should exhibit a lower resistance than LSC64. However, Bond et al. warn that the isokinetic temperature can only be established with statistical rigor for datasets with many temperature points over a wide temperature range, which the present study lacks.

Chemical capacitance

Figure 3-30 shows the variation in chemical capacitance with cobalt content. The chemical capacitance of LSC64 is between two and three times larger than that of LSF64, consistent with previous results showing higher oxygen non-stoichiometry for the cobalt end-member.[15] Notably, this increase is not linear – capacitance begins to change significantly once cobalt atoms outnumber iron atoms. Furthermore, the trend of capacitance with cobalt stoichiometry agrees with results from Hashimoto et al. which show, between 600 and 700°C at 1 atm O_2, that oxygen non-stoichiometry only changes appreciably once cobalt occupies the majority of the B-site.[25] This contrasts with the results for surface resistance (Figure 3-26) which show significant change between LSCF6455 and LSF64. In this composition regime, it seems that the ionic conductivity does not significantly impact the observed activity. This result motivates further study of the lanthanum-strontium ratio on the A-site which largely controls low-temperature vacancy concentration through the defect reaction, written in Kroger-Vink notation,

$$2SrO_2 \xrightarrow{LaCo_{1-x}Fe_xO_3} 2Sr'_{La} + 3O_O^X + V_O^{\cdot\cdot} \tag{3.3}$$

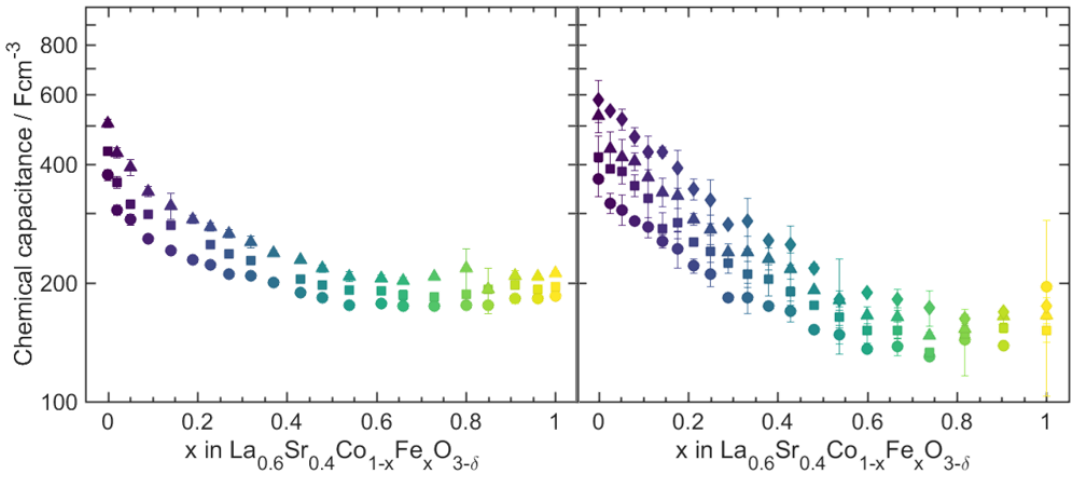

Figure 3-30. Repeatability. Comparison of the volume-normalized chemical capacitance of LSCF at 600°C (●), 625°C (■), 650°C (▲), and 675°C (◆) and 1 atm O2 obtained for both libraries. Plotted points are averaged over all microelectrodes with the same composition. (left) Library I; (right) Library ii.

where a dash superscript indicates effective negative charge, a dot superscript represents positive charge, an X represents neutral charge, and V_M represents a vacancy for species M. If the ionic conductivity resulting from high vacancy concentration is not limiting the two-phase boundary reaction, then perhaps the amount of strontium can be reduced to limit the effect of strontium segregation. Further study is warranted in this area.

As before, environmental variation can validate the interpretation of these capacitance results. Figure 3-31 shows the dependence of capacitance on oxygen partial pressure. The capacitance of cobalt-dominant compositions is more sensitive to changes in oxygen partial pressure than LSF64, indicating higher reducibility consistent with their respective capacitance values. In addition, though it is not carried out here, Kawada et al.[26] have used chemical capacitance measurements to calculate the thin-film oxygen vacancy concentration

of LSC64, as shown in Crumlin et al[8]. That the values in this work are consistent with those results suggests the same conclusion, namely that the oxygen vacancy concentration in thin-film LSC64 is smaller than that in the bulk material.

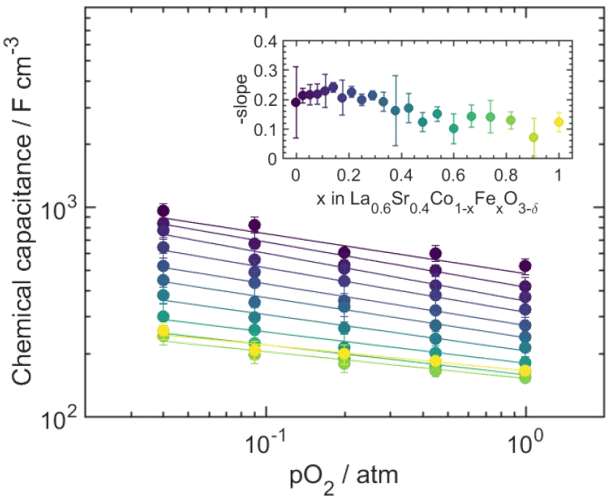

Figure 3-31. Oxygen dependence. Volume-normalized chemical capacitance for Library ii as a function of oxygen partial pressure shown as double-logarithmic plots, at a film temperature of 650 °C. Inset shows slope as a function of composition, with a guideline at ¾. Color corresponds to microelectrode composition. Plotted values are averaged over multiple microelectrodes with the same composition.

The Arrhenius dependence of the chemical capacitance is shown in Figure 3-32 and shows an activation energy ranging from 0.3 eV for LSF64 to 0.5 eV for LSC64. These values are consistent with those measured by Baumann et al.[5] However, it should be noted that the observed trend contradicts that found by Baumann, who observed the opposite trend of activation energy with cobalt content. The difference in these results may be attributable to

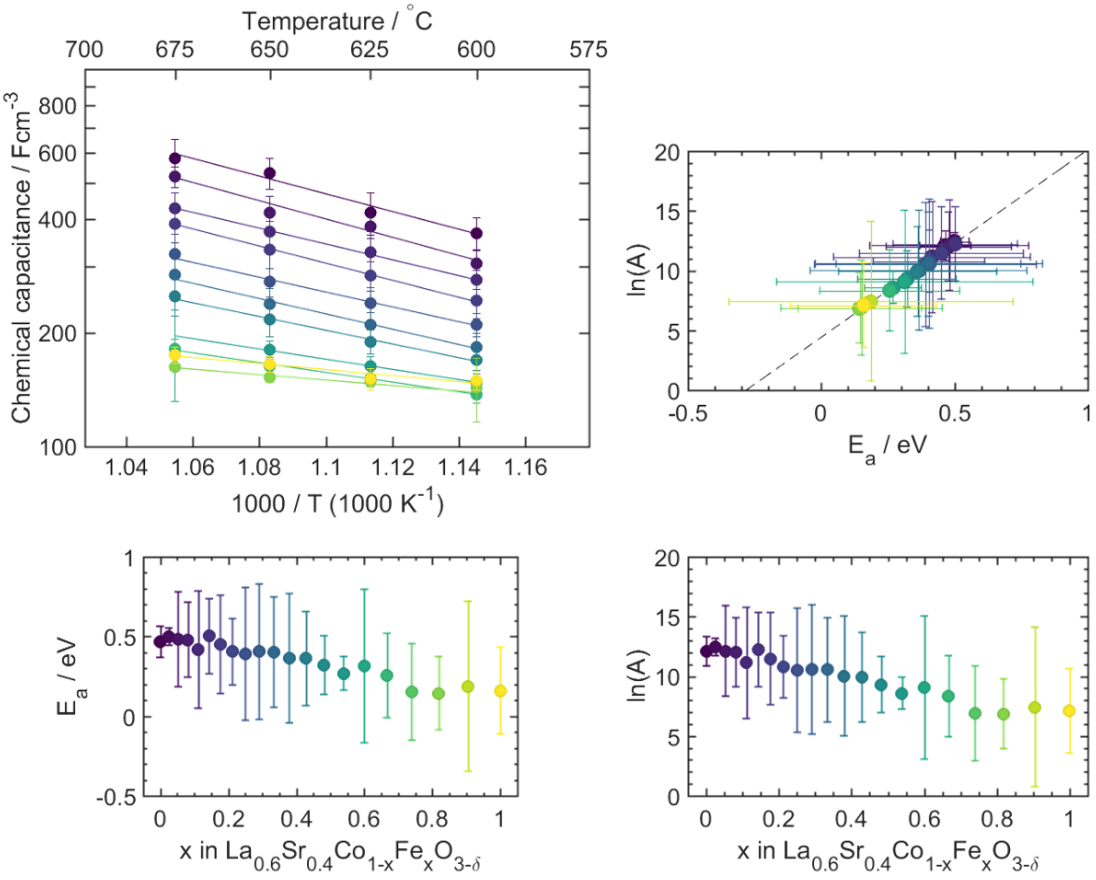

Figure 3-32. Arrhenius behavior. Temperature dependence of chemical capacitance in LSCF (Library ii) at 1 atm pO2. Plotted values are averaged over multiple microelectrodes with the same composition. (a) Arrhenius plot of volume-normalized chemical capacitance with electrode composition shown by color; (b) activation energy and (c) pre-exponential factor as functions of composition determined from Arrhenius scaling. (d) Log of the pre-exponential factor versus activation energy.

the ceria interlayer and inadequate equilibration, as it is commented by the authors that `micro-electrode measurements are carried out swiftly to avoid degradation. This is corroborated by the relatively low values for area-specific resistance they observe.

That the chemical capacitance also appears to obey the Cremer-Constable relation seems intriguing as it is not an inherently kinetic parameter. However, the observed relationship can be interpreted as relating to the kinetics of oxygen vacancy creation. As discussed above, the relationship between chemical capacitance and reducibility can be thought of as a direct relationship between chemical capacitance and non-stoichiometry, and thus the Arrhenius behavior of the non-stoichiometry maps directly to that of δ, the oxygen non-stoichiometry. Therefore, the observed activation energy directly relates to the activation energy of oxygen vacancy creation in the oxide. Viewed in this way, the observed trend in activation energy conveys that while the activation energy of oxygen vacancy creation is higher for cobalt-dominant LSCF64, the pre-factor more than compensates for this increase and a higher capacitance and non-stoichiometry is observed.

Comparison to literature values

Table 3-1 shows a comparison to literature values measured for individual compositions in the $La_{0.6}Sr_{0.4}Co_{1-x}Fe_xO_3$ family across a variety of conditions. The literature values show varying agreement with those measured in this work. Though the results from this work are between a factor of two and an order of magnitude different from those from Fleig et al.[3,20], the works from the author's group note that the measurements were taken shortly after achieving the environmental conditions and thus degradation was minimized. In Januschewsky et al.[7], values for 200nm thick LSC64 films deposited at 600°C reached 10

Ωcm^2 after 17 hours of measurement and may have continued to rise afterwards. All the measurements in this work occur after an initial 24-hour equilibration period at 650°C and 1 atm O_2, and given the stability seen in Figure 3-24, are taken after any initial degradation has occurred. The work of other groups falls well within the range of our measurements, indicating that this methodology does indeed correspond to literature values and therefore rigorous comparisons can be made between the different compositions measured here and by others.

Table 3-5. Comparison of LSCF literature results.

Reference	Composition	ASR (Ω cm^2)	Activation energy (eV)	C_{chem} (F cm^{-3})	Condition
(Plonczak, Sogaard et al. 2012)	$La_{0.58}Sr_{0.4}Co_{0.2}Fe_{0.8}O_3$	200	1.6 – 2.4	500	650°C, 1 atm O_2
(Baumann, Fleig et al. 2006)	$La_{0.6}Sr_{0.4}FeO_3$	4-11	1.8	1300	
	$La_{0.6}Sr_{0.4}Co_{0.2}Fe_{0.8}O_3$	2-9	1.6	1100	750°C, 0.2 atm O_2
	$La_{0.6}Sr_{0.4}Co_{0.8}Fe_{0.2}O_3$	5	1.3	1600	750°C, 0.2 atm O_2
	$La_{0.6}Sr_{0.4}CoO_3$	3-10	1.3	2700	750°C, 0.2 atm O_2
(Kawada, Suzuki et al. 2002)	$La_{0.6}Sr_{0.4}CoO_3$			200	700°C, 1 atm O_2
(Januschewsky, Ahrens et al. 2009)	$La_{0.6}Sr_{0.4}CoO_3$	0.1-100	1.4	2000	600°C, 0.2 atm O_2
(Crumlin et al. 2012)	$La_{0.6}Sr_{0.4}CoO_3$	1-2		300	550°C, 1 atm O_2
(Kogler, Nenning et al. 2015)	$La_{0.6}Sr_{0.4}FeO_3$	13.6*		1293	610°C, 1 atm O_2
This work	$La_{0.6}Sr_{0.4}Co_{1-x}Fe_xO_3$	100 – 600	1.4 – 2.1	100 – 600	650°C, 1 atm O_2

5. Summary

The entire binary composition phase space of LSCF64, a mixed ionic and electronic conducting solid oxide fuel cell electrode material, was synthesized and measured on a single electrolyte substrate under the same synthesis and experimental conditions. Measurements of material properties as determined by microelectrode impedance spectroscopy were demonstrated to be stable and repeatable. The electrochemical pathway for oxygen reduction in the thin-film morphology was confirmed to be dominated by a surface reaction followed by bulk condition of ions. LSF64 was shown to be four times less active than LSC64, while the latter was shown to be more than twice as easily reducible as the former by measurements of chemical capacitance. Little variation is observed between samples prepared with different composition gradings but synthesized and measured under the same conditions, indicating that this methodology provides robust and repeatable measurements of material properties. The truly like quantitative comparisons between materials systems shown by this study inform materials selection tradeoffs in real fuel cell systems and pave the way to high-throughput exploration of new material compositions.

6. Bibliography

1 Kilner, J. A. & Burriel, M. Materials for Intermediate-Temperature Solid-Oxide Fuel Cells. *Annual Review of Materials Research* **44**, 365-393, doi:10.1146/annurev-matsci-070813-113426 (2014).

2 Gao, Z., Mogni, L. V., Miller, E. C., Railsback, J. G. & Barnett, S. A. A perspective on low-temperature solid oxide fuel cells. *Energ Environ Sci* **9**, 1602-1644, doi:10.1039/c5ee03858h (2016).

3 Baumann, F. S. *et al.* Strong performance improvement of La0.6Sr0.4Co0.8Fe0.2O3-delta SOFC cathodes by electrochemical activation. *J Electrochem Soc* **152**, A2074-A2079, doi:Doi 10.1149/1.2034529 (2005).

4 Baumann, F. S., Fleig, J., Habermeier, H. U. & Maier, J. Impedance spectroscopic study on well-defined (La,Sr)(Co,Fe)O3-delta model electrodes. *Solid State Ionics* **177**, 1071-1081, doi:DOI 10.1016/j.ssi.2006.02.045 (2006).

5 Baumann, F. S. *et al.* Quantitative comparison of mixed conducting SOFC cathode materials by means of thin film model electrodes. *J Electrochem Soc* **154**, B931-B941, doi:Doi 10.1149/1.2752974 (2007).

6 Baumann, F. S., Maier, J. & Fleig, J. The polarization resistance of mixed conducting SOFC cathodes: A comparative study using thin film model electrodes. *Solid State Ionics* **179**, 1198-1204, doi:DOI 10.1016/j.ssi.2008.02.059 (2008).

7 Januschewsky, J., Ahrens, M., Opitz, A., Kubel, F. & Fleig, J. Optimized La0.6Sr0.4CoO3-delta Thin-Film Electrodes with Extremely Fast Oxygen-Reduction Kinetics. *Adv Funct Mater* **19**, 3151-3156, doi:DOI 10.1002/adfm.200900362 (2009).

8 Crumlin, E. J. *et al.* Oxygen Electrocatalysis on Epitaxial La0.6Sr0.4CoO3-delta Perovskite Thin Films for Solid Oxide Fuel Cells. *J Electrochem Soc* **159**, F219-F225, doi:Doi 10.1149/2.018207jes (2012).

9 Boukamp, B. A., Hildenbrand, N., Bouwmeester, H. J. M. & Blank, D. H. A. Impedance of thin film cathodes: Thickness and current collector dependence. *Solid State Ionics* **283**, 81-90, doi:10.1016/j.ssi.2015.10.013 (2015).

10 Boukamp, B. A., Hildenbrand, N., Nammensma, P. & Blank, D. H. A. The impedance of thin dense oxide cathodes. *Solid State Ionics* **192**, 404-408, doi:10.1016/j.ssi.2010.05.037 (2011).

11 Jamnik, J. & Maier, J. Generalised equivalent circuits for mass and charge transport: chemical capacitance and its implications. *Phys Chem Chem Phys* **3**, 1668-1678, doi:Doi 10.1039/B100180i (2001).

12 Koinuma, H. & Takeuchi, I. Combinatorial solid-state chemistry of inorganic materials. *Nat Mater* **3**, 429-438 (2004).

13 Usiskin, R. E., Maruyama, S., Kucharczyk, C. J., Takeuchi, I. & Haile, S. M. Probing the reaction pathway in (La0.8Sr0.2)(0.95)MnO3+delta using libraries of thin film microelectrodes. *J Mater Chem A* **3**, 19330-19345, doi:10.1039/c5ta02428e (2015).

14 Kuhn, M., Hashimoto, S., Sato, K., Yashiro, K. & Mizusaki, J. Thermo-chemical lattice expansion in La0.6Sr0.4Co1-yFeyO3-delta. *Solid State Ionics* **241**, 12-16, doi:DOI 10.1016/j.ssi.2013.03.023 (2013).

15 Kuhn, M. *et al.* Oxygen Nonstoichiometry and Thermo-Chemical Stability of Perovskite-Type La0.6Sr0.4Co1-yFeyO3-delta (y=0, 0.2, 0.4, 0.5, 0.6, 0.8, 1) Materials. *J Electrochem Soc* **160**, F34-F42, doi:10.1149/2.050301jes (2013).

16 Newman, J. Resistance for Flow of Current to a Disk. *J Electrochem Soc* **113**, 501-&, doi:Doi 10.1149/1.2424003 (1966).

17 Oh, T. S. & Haile, S. M. Electrochemical behavior of thin-film Sm-doped ceria: insights from the point-contact configuration. *Phys Chem Chem Phys*, doi:10.1039/c4cp05990e (2015).

18 Plonczak, P., Sogaard, M., Bieberle-Hutter, A., Hendriksen, P. V. & Gauckler, L. J. Electrochemical Characterization of La0.58Sr0.4Co0.2Fe0.8O3-delta Thin Film Electrodes Prepared by Pulsed Laser Deposition. *J Electrochem Soc* **159**, B471-B482, doi:10.1149/2.043204jes (2012).

19 Chueh, W. C. & Haile, S. M. Electrochemical studies of capacitance in cerium oxide thin films and its relationship to anionic and electronic defect densities. *Phys Chem Chem Phys* **11**, 8144-8148, doi:Doi 10.1039/B910903j (2009).

20 Kogler, S., Nenning, A., Rupp, G. M., Opitz, A. K. & Fleig, J. Comparison of Electrochemical Properties of La0.6Sr0.4FeO3-delta Thin Film Electrodes: Oxidizing vs. Reducing Conditions. *J Electrochem Soc* **162**, F317-F326, doi:10.1149/2.0731503jes (2015).

21 Lai, W. & Haile, S. M. Impedance spectroscopy as a tool for chemical and electrochemical analysis of mixed conductors: A case study of ceria. *J Am Ceram Soc* **88**, 2979-2997, doi:DOI 10.1111/j.1551-2916.2005.00740.x (2005).

22 Tai, L. W., Nasrallah, M. M., Anderson, H. U., Sparlin, D. M. & Sehlin, S. R. Structure and electrical properties of La1 − xSrxCo1 − yFeyO3. Part 1. The system La0.8Sr0.2Co1-xFexO3. *Solid State Ionics* **76**, 273-283, doi:https://doi.org/10.1016/0167-2738(94)00245-N (1995).

23 Chueh, W. C. & Haile, S. M. Electrochemistry of Mixed Oxygen Ion and Electron Conducting Electrodes in Solid Electrolyte Cells. *Annu Rev Chem Biomol* **3**, 313-341, doi:DOI 10.1146/annurev-chembioeng-073009-101000 (2012).

24 Bond, G. C., Keane, M. A., Kral, H. & Lercher, J. A. Compensation Phenomena in Heterogeneous Catalysis: General Principles and a Possible Explanation. *Catalysis Reviews* **42**, 323-383, doi:10.1081/CR-100100264 (2000).

25 Hashimoto, S. *et al.* Oxygen nonstoichiometry and thermo-chemical stability of La0.6Sr0.4Co1-yFeyO3-delta (y=0.2, 0.4, 0.6, 0.8). *Solid State Ionics* **181**, 1713-1719, doi:10.1016/j.ssi.2010.09.024 (2010).

26 Kawada, T. *et al.* Determination of Oxygen Vacancy Concentration in a Thin Film of La[sub 0.6]Sr[sub 0.4]CoO[sub 3−δ] by an Electrochemical Method. *J Electrochem Soc* **149**, E252, doi:10.1149/1.1479728 (2002).

Chapter 4

NOVEL CATHODE MATERIALS ON OXIDE-ION CONDUCTING ELECTROLYTES

As a widely-studied state-of-the-art material, LSCF is useful to use as a benchmark to compare against the performance of other materials. The full benefit of the high-throughput approach investigated in this thesis is realized through the application to novel materials as well as well characterized materials. An excellent candidate for this type of exploration is $PrBa_{0.5}Sr_{0.5}Co_{2-x}Fe_xO_{5+\delta}$ (PBSCF55).

As described in the introduction, PBSCF is a double-perovskite material recently shown to exhibit high performance as an SOFC cathode[1,2]. In this work, we use the same methodology employed in Chapter 3 to study PBSCF: we will use PBSC and PBSF PLD targets to deposit a gradient thin film of PBSCF on a YSZ substrate, and subsequently measure patterned microelectrodes using microelectrode impedance spectroscopy.

1. Sample Synthesis and Characterization

Samples were synthesized and characterized according to details found in the experimental section. The results of the characterization are shown below. Figure 4-33 shows a schematic of the prepared sample before ion milling. A layer of SDC20 approximately 20 nm in thickness is deposited as a reaction barrier between the (100)-oriented single-crystal 5x10mm YSZ substrate (MTI). A continuous composition gradient is then deposited from PBSF to PBSC by pulsed laser deposition.

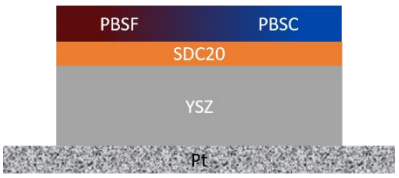

Figure 4-33. Sample schematic of PBSCF gradient sample.

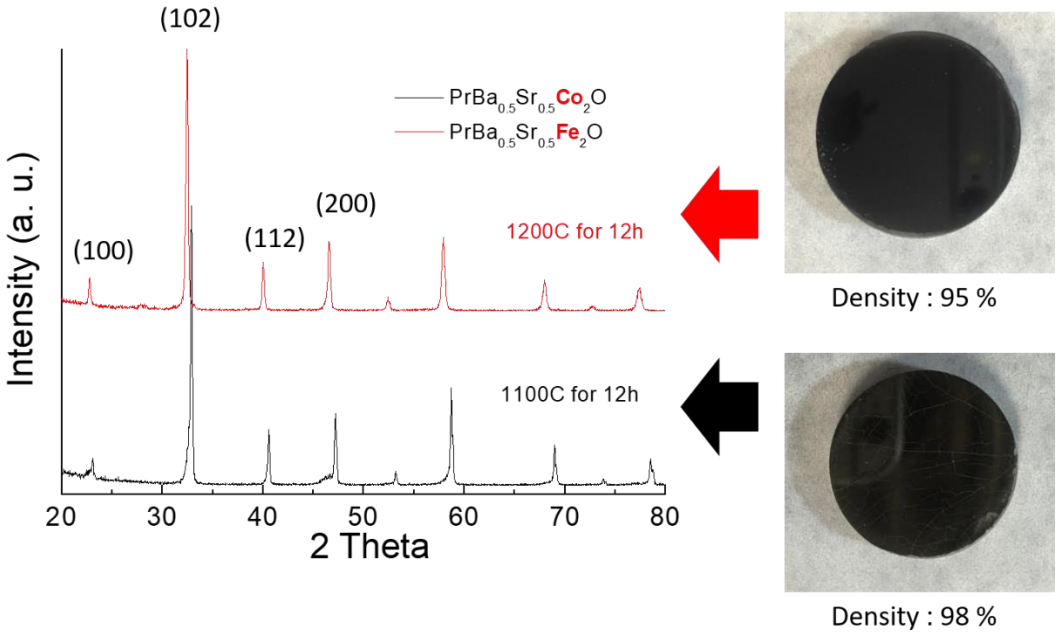

Figure 4-34. XRD patterns of PBSC and PBSF PLD targets. (Courtesy Sihyuk Choi)

XRD patterns confirming the phase purity of the prepared PLD targets is shown Figure 4-34 for both PBSF and PBSC. The first four main reflections of the P4/mmm tetragonal structure are labelled. There is a slight shift to higher angle and larger lattice parameter with substitution of iron for cobalt. The approximate density as a percentage of the theoretical density, $\rho_{\mathrm{PBSC}} = 6.66\ g/cm^3$ and $\rho_{\mathrm{PBSF}} = 6.48\ g/cm^3$, is shown below a photograph of each target. Despite some surface cracks, the targets were suitable for use in deposition. In

addition, a small shoulder is observed on several of the peaks in the PBSF target spectrum. These shoulders are attributed to sample alignment within the diffractometer.

Thin-film X-ray diffraction patterns for the deposited composition spread are shown in Figure 4-35. As expected, we observe a continuous increase in lattice parameter from the PBSC side of the film (top pattern, blue) to the PBSF side of the film (bottom pattern, red) as observed by the (102) reflection at 32-33° 2θ and the (204) reflection at 68-69° 2θ. The peaks at 35° 2θ and 74° 2θ are attributed to the YSZ substrate.

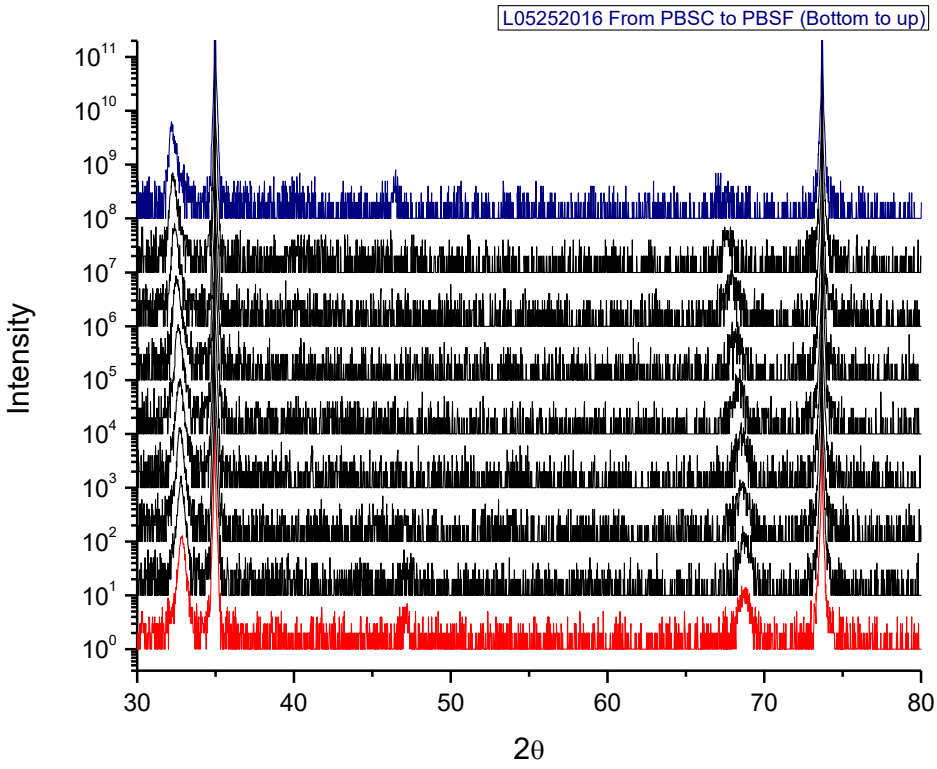

Figure 4-35. Thin-film XRD pattern of PBSC-PBSF composition spread. (Courtesy Yangang Liang, Xiaohang Zhang)

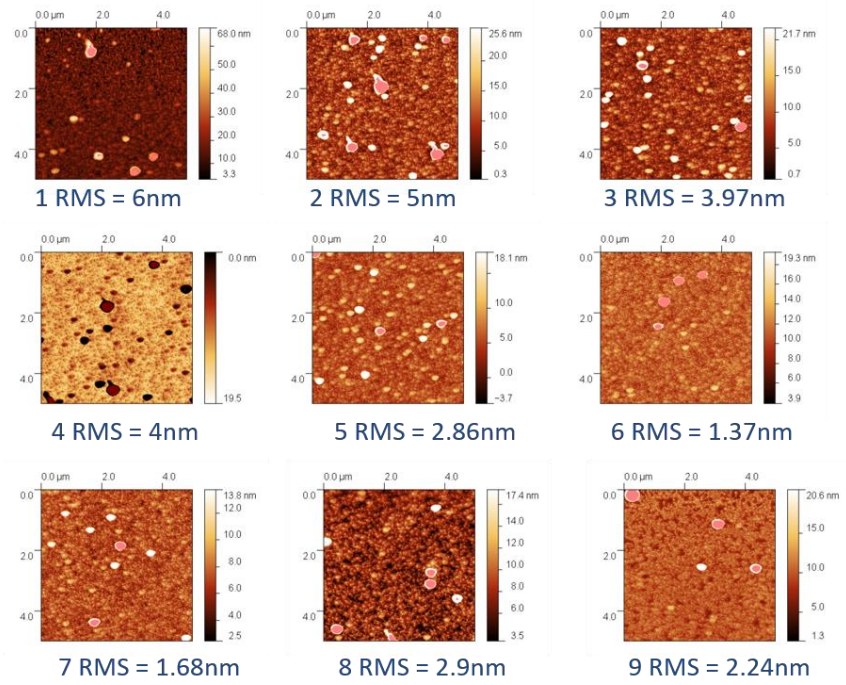

Figure 4-36. Atomic force microscopy (AFM) images of the PBSC-PBSF composition spread. (Courtesy Yangang Liang, Xiaohang Zhang).

Atomic force microscopy images (Figure 4-36) show a smooth film surface, with root-mean-squared roughness less than 6nm across the entire spread. This implies the film is smooth and dense. The images also show the film lacks any cracks that would lead to additional triple-phase boundaries. Similar to the case for LSCF, PBSCF grains are rectangular on the iron-dominant end, but nearly square or with equal aspect ratio on the cobalt-dominant end. As discussed for LSCF, this change in surface grain boundary density will be evaluated against the observed change in surface activity to determine whether it is sufficient to explain the measured variation.

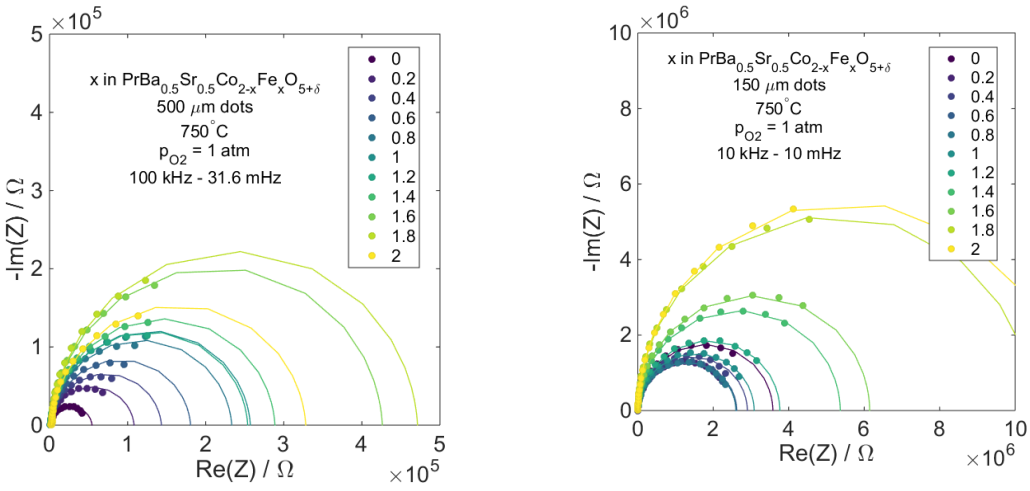

Figure 4-37. Nyquist spectra of (left) 500um and (right) 150um microelectrodes across PBSCF gradient. Solid lines represent fits to RRQ model circuit.

2. Impedance Results

Raw spectra

Figure 4-37 shows the results of impedance spectroscopy on PBSCF micro-electrodes taken at a stage temperature of 750°C (650°C film temperature) and 1 atmosphere pO_2 for both large diameter (500µm) and small diameter (150 um) micro-dots. Environmental conditions and frequency range of impedance measurement are shown in each figure. Composition is shown by color as blue (PBSC) to yellow (PBSF), though in this case x ranges from 0 to 2 due to double perovskite stoichiometry, rather than from 0 to 1. Qualitatively, again matching the LSCF results, an increase in total resistance is observed from cobalt to iron. Unlike the case for LSCF, however, no interfacial arc is observed, suggesting that interfacial processes at these conditions for these materials contribute little to the measured impedance. Therefore, the dots are fit with an RRQ circuit using non-linear least squares, rather than an RRQRQ circuit.

This sample, originally intended to be a preliminary measurement to a more complete study, was not characterized as fully as the LSCF sample. The results thus lack a few important details that would yield deeper insight, such as temperature and atmospheric dependence. Furthermore, physical characterization was likewise incomplete, lacking precise measurements by EDS of the composition range or FIB-SEM measurements of film thickness. However, much insight can still be obtained from this limited data set.

Geometry dependence

The geometry dependence of the offset resistance, electrochemical resistance, and chemical capacitance can be found in the right column of Figure 4-38. Observing these values yields many similar trends to what was found for LSCF. For the offset resistance, the slopes of resistance with diameter on a log-log plot are all close to -1, consistent with the Newman equation[3]. As was seen for LSCF, the trend deviates on the iron-dominant side, where the slope becomes more positive due to the increased sheet resistance of the iron-dominant end-member.

For electrode resistance, the slopes are all near -2, though there is significant deviation for some individual compositions (particularly for the end-members). Despite the noise, the bulk of the data suggests that, as expected, PBSCF is area-limited. The deviation in the slope may be due to difference in film growth or structure in the end-member films; perhaps the mixing of the B-site atoms in the gradient regime plays a role in altering the structure of the surface of the film.

Finally, for chemical capacitance, the slopes are all very close to 2, indicating as expected that the chemical capacitance scales with the volume (in this case, strictly area) of the micro-electrodes.

Composition depdence

A quick glance at the results of parameter fitting with respect to composition (Figure 4-38, left column) show a great degree of similarity to the results of the analysis of LSCF. Akin to those results, we observe an increase in electrochemical resistance and a decrease in the chemical capacitance with increasing iron content. This again emphasizes the important role that the more easily reducible cobalt plays in increasing both electronic conductivity and reducibility.

For offset resistance, we see more clearly the impact of sheet resistance evidenced by the creep values for the largest-diameter micro-electrodes upward at a rate faster than the smaller diameter dots. One explanation for this behavior is that the sheet resistance of the more insulating iron-dominant compositions renders the area effectively reached by the probe tip smaller than the dot itself. Thus, the value of the offset resistance behaves as though the dot were smaller than it is.

The composition trends for electrode resistance are more puzzling since the largest and smallest dots do not obey a monotonic increase. This provides further evidence that perhaps an important parameter changes in the linear crossover regime of the film. Further study is needed to capture whether this trend is noise or a reflection of a real property of the material.

Finally, the chemical capacitance shows very similar trends to LSCF: with increasing cobalt content, the chemical capacitance increases. In addition, there seems to be a value of iron content around 75% where the value of the capacitance stays constant. Further study is warranted to determine the effect of the different nature of oxygen vacancies between the two materials.

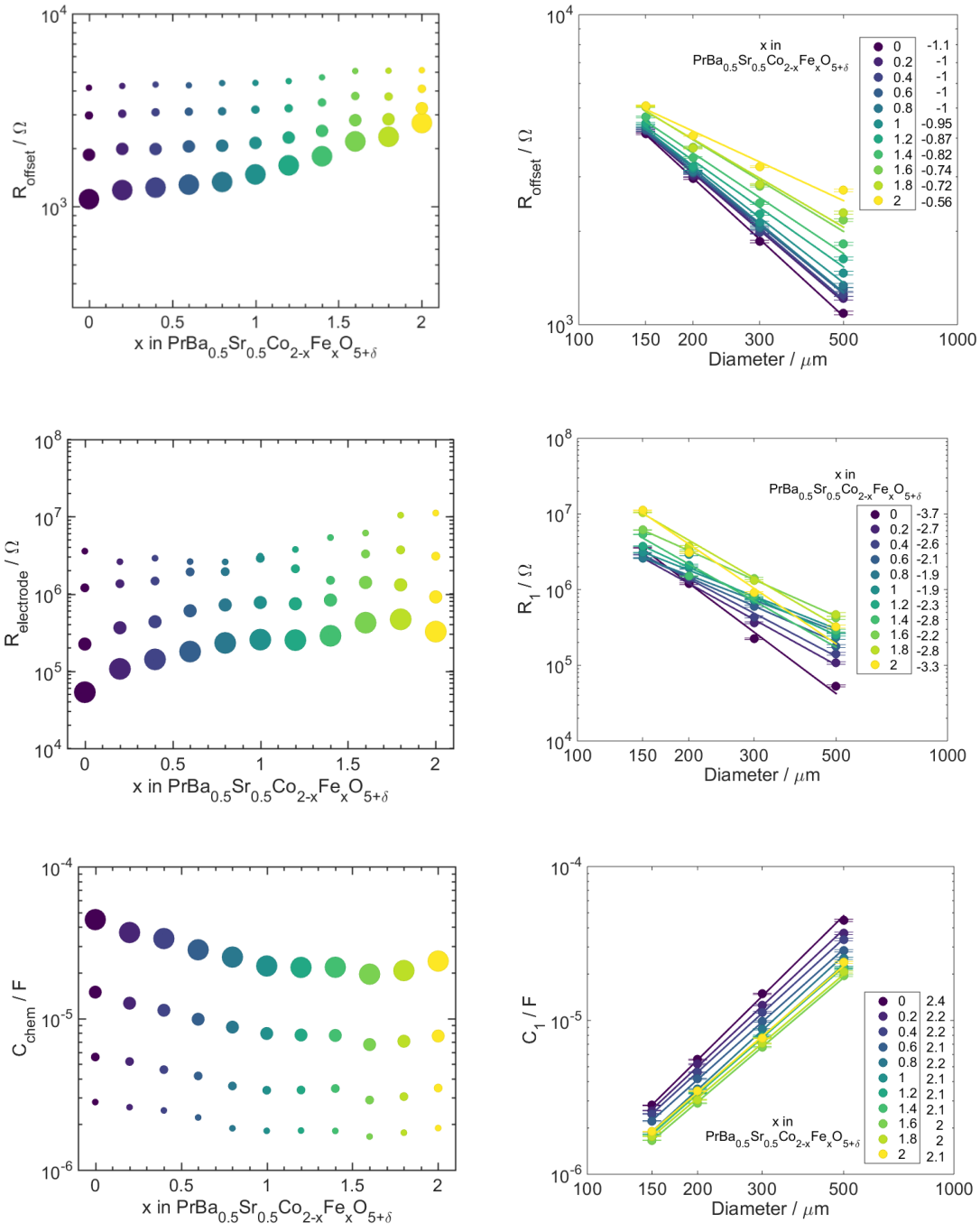

Figure 4-38. Results of fitting RRQ circuit to PBSCF microelectrode impedance spectra. From top to bottom, offset resistance, electrochemical resistance, and total capacitance. Left column shows composition dependence for all measured diameters; right column shows diameter dependence for all measured

compositions as well as values for fitted slopes. Composition values are nominal rather than as-measured.

3. Comparison to LSCF

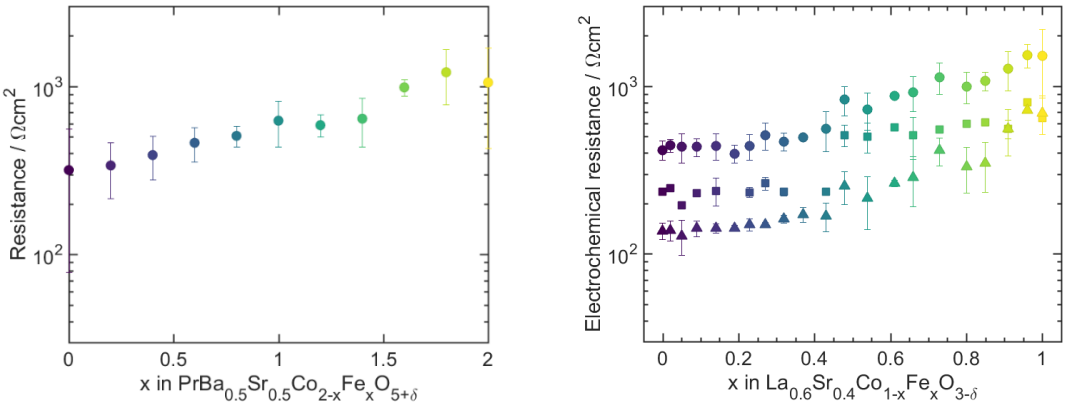

Figure 4-39. Comparison of area-specific resistance of PBSCF (left) and LSCF (right). The PBSCF is measured at 650°C, while the circles on the right figure represent LSCF measured at 650°C.

The area-specific resistance of PBSCF micro-electrodes appears comparable to that of LSCF micro-electrodes, as seen in Figure 4-39. The trend of increasing resistance with increasing iron content is also observed. The overall difference in area-specific resistance between the cobalt end-member and the iron end-member for both materials libraries appears to be a factor of four. This is consistent with the limited literature that exists comparing the performance of these materials in button cells[4]. For LSCF, it appeared as though the electrical conductivity was the determining factor in performance. For PBSCF, this also seems to be the case, though careful measurement of the electrical properties of PBSCF is still needed.

That PBSCF performs almost identical to LSCF in terms of electrochemical resistance is somewhat surprising, given the impressive fuel cell results using PBSCF as an electrode[1].

The performance difference can perhaps be explained by the structure difference between the two materials and the resulting impact on measurement geometry. As LSCF is a pseudocubic perovskite, its bulk grain orientation should have little effect on the observed diffusion rate of oxygen. However, as a double perovskite, PBSCF is non-isotropic, and preferential grain orientation arising from PLD could block the "pore channels" that are especially favorable to ionic conductivity. To confirm whether this is the case, a future study should compare the same two materials on different types of substrates, such as (110)-oriented YSZ or polycrystalline YSZ or even other electrolyte materials like ceria. These studies will show whether the difference is truly the result of bulk crystal orientation.

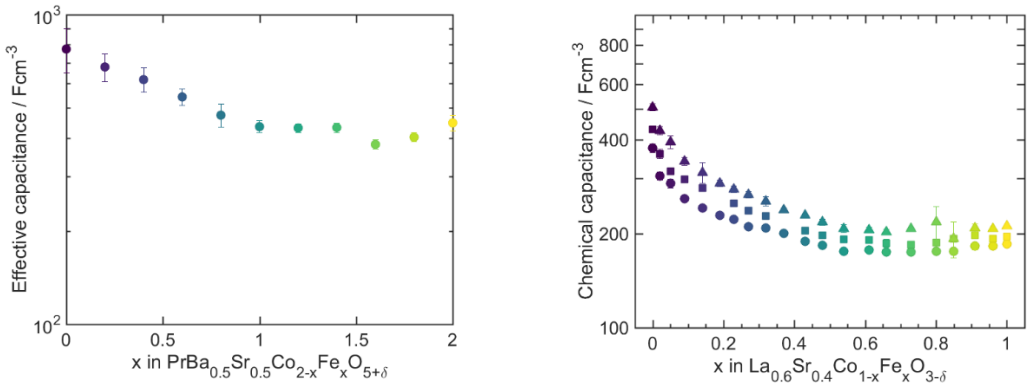

Figure 4-40. Comparison of chemical capacitance.

For chemical capacitance, PBSCF appears to have higher chemical capacitance than LSCF, as shown in Figure 4-40. The general trend with composition is again the same for both materials: as the iron content increases, the chemical capacitance decreases. This is again likely due to the decrease in electronic and ionic conductivity with increased iron content[5,6]. However, the factor of two difference in chemical capacitance between PBSCF and LSCF is

interesting. The difference may arise the from the difference in electronic conductivity between PBSCF and LSCF[2,7] or from the difference in ionic conductivity[8].

4. Summary

There is a great deal of similarity between the results for PBSCF and the results for LSCF. Increasing resistance and decreasing capacitance with increasing iron content was consistent between both libraries, down to the factor of four between the resistance of LSC and the resistance of LSF. This result is interesting in and of itself given the superior performance displayed by PBSCF in a recent fuel cell test. However, the measurement geometry and sample synthesis may have impacted the crystal structure in which PBSCF was measured, failing to take advantage of the high-conductivity channels. Future studies should be performed with PBSCF on polycrystalline or other oriented substrates to determine whether changing the growth orientation has an impact on the measured performance in this geometry.

5. References

1 Choi, S. *et al.* Highly efficient and robust cathode materials for low-temperature solid oxide fuel cells: PrBa0.5Sr0.5Co(2-x)Fe(x)O(5+delta). *Scientific reports* **3**, 2426, doi:10.1038/srep02426 (2013).

2 Jeong, D. *et al.* Structural, Electrical, and Electrochemical Characteristics of LnBa0.5Sr0.5Co1.5Fe0.5O5+δ (Ln=Pr, Sm, Gd) as Cathode Materials in Intermediate-Temperature Solid Oxide Fuel Cells. *Energy Technology* **5**, 1337-1343, doi:10.1002/ente.201600618 (2017).

3 Newman, J. Resistance for Flow of Current to a Disk. *J Electrochem Soc* **113**, 501-&, doi:Doi 10.1149/1.2424003 (1966).

4 Jiang, L., Wei, T., Zeng, R., Zhang, W. X. & Huang, Y. H. Thermal and electrochemical properties of PrBa0.5Sr0.5Co2-xFexO5+delta (x=0.5, 1.0, 1.5) cathode materials for solid-oxide fuel cells. *J Power Sources* **232**, 279-285, doi:10.1016/j.jpowsour.2013.01.064 (2013).

5 Teraoka, Y., Zhang, H. M., Okamoto, K. & Yamazoe, N. Mixed Ionic-Electronic Conductivity of La1-Xsrxco1-Yfeyo3-Delta Perovskite-Type Oxides. *Mater Res Bull* **23**, 51-58, doi:Doi 10.1016/0025-5408(88)90224-3 (1988).

6 Tai, L. W., Nasrallah, M. M., Anderson, H. U., Sparlin, D. M. & Sehlin, S. R. Structure and electrical properties of La1 − xSrxCo1 − yFeyO3. Part 1. The system La0.8Sr0.2Co1-xFexO3. *Solid State Ionics* **76**, 273-283, doi:https://doi.org/10.1016/0167-2738(94)00245-N (1995).

7 Tai, L. W., Nasrallah, M. M., Anderson, H. U., Sparlin, D. M. & Sehlin, S. R. Structure and electrical properties of La1 − xSrxCo1 − yFeyO3. Part 2. The system La1 − xSrxCo0.2Fe0.8O3. *Solid State Ionics* **76**, 273-283, doi:https://doi.org/10.1016/0167-2738(94)00245-N (1995).

8 Katsuki, M., Wang, S., Dokiya, M. & Hashimoto, T. High temperature properties of La0.6Sr0.4Co0.8Fe0.2O3−δ oxygen nonstoichiometry and chemical diffusion constant. *Solid State Ionics* **156**, 453-461, doi:https://doi.org/10.1016/S0167-2738(02)00733-6 (2003).

Chapter 5

TRADITIONAL CATHODE MATERIALS ON PROTON-CONDUCTING ELECTROLYTES

Though study of proton-conducting electrolytes has been ongoing for many years, attempts to design and optimize cathode materials for use with proton conductors have emerged only recently. Efforts to demonstrate p-SOFC performance have often utilized cathode materials developed for use on oxygen-ion conducting SOFC electrolytes, such as LSCF or LSM, though nearly always composited with a proton-conducting phase such as BZY[1-6]. In the last several years, so-called "triple-conducting" oxides – materials which conduct electrons, protons, and oxygen ions – have begun to be identified and tested for use in p-SOFC devices[7-10]. However, these novel materials are still investigated in a manner similar to SOFC cathode materials, in which individual compositions are manufactured and tested separately to produce a single result. Given the complicated nature of such triple-conducting systems, it is even more critical that care be taken when interpreting the results of experimental methods designed to measure the kinetic properties of these systems.

For the purposes of studying traditional oxide-ion conducting materials on proton-conducting electrolytes, LSCF was again chosen as the candidate material. Modelling efforts have been made to predict proton uptake in compositions of LSF[11] which show that the enthalpy of hydration of LSF is much smaller than the enthalpy of hydration for typical proton-conducting materials such as BZY. This explains why LSCF is rarely used as the sole cathode material in a proton conducting fuel cell, and is nearly always composited with a proton-conducting phase such as BZY or BZPY: it lacks sufficient proton conductivity to

serve as a mixed proton- and electron-conductor. Such composite morphologies again serve to maximize the density of triple phase boundaries to improve reaction kinetics.

To confirm whether LSCF does indeed have sufficient proton conductivity to serve as a mixed conductor in a thin film geometry, experiments were carried out using the scanning impedance probe as described in the previous chapters. However, modifications to the technique were necessary to ensure that the measurements conducted were accurate reflections of the physical parameters of the material. After discussing the challenges that arose in carrying out this measurement, results for LSCF on a proton-conducting substrate are presented.

1. Challenges

There are several difficulties in measuring proton-conducting electrode activity[12]. First of all, proton-conducting electrolytes are notoriously refractory. This makes synthesis of substrates for deposition of proton conducting materials difficult. For oxygen-ion conducting electrolytes, commercial single-crystal substrates are readily available; however, no commercial sources exist for proton-conducting materials and serial synthesis in-house can lead to similar issues of variation in morphology that this technique was developed to avoid. Second, proton-conducting materials must be measured in humidified atmospheres to allow uptake of protons, and humidified environments pose experimental challenges as all surfaces that contact gas must be heated to prevent condensation.

Steps were taken to alleviate these issues. For instance, on initial proton-conducting substrates, a thick layer of yttrium-doped barium zirconate was deposited by PLD between the substrate and the electrode layer in an attempt to achieve a smooth surface onto which to

deposit the electrode. Eventually, a new proton-conducting electrolyte composition, BZCYYB4411, was developed through a parallel effort and, as it was easier to manufacture, used as the primary electrolyte. To mitigate condensation, the amount of humidity is restricted to equivalent water temperatures below room temperature as the scanning probe is too large to have all its surfaces heated.

2. Single-composition library

Synthesis and characterization

Figure 5-41. Sample schematic.

LSCF6428 was deposited onto a BZY20 substrate with a BZY20 interlayer to promote a smooth surface. The film was patterned into the micro-dot morphology in the manner described in Chapter 2. Impedance measurements were taken under humidified atmospheres ($p_{H_2O} \approx 0.016$ at a bubbler temperature of 15°C) at high temperatures (450-550°C). Impedance measurements were taken from 1 MHz to 0.032 mHz in frequency.

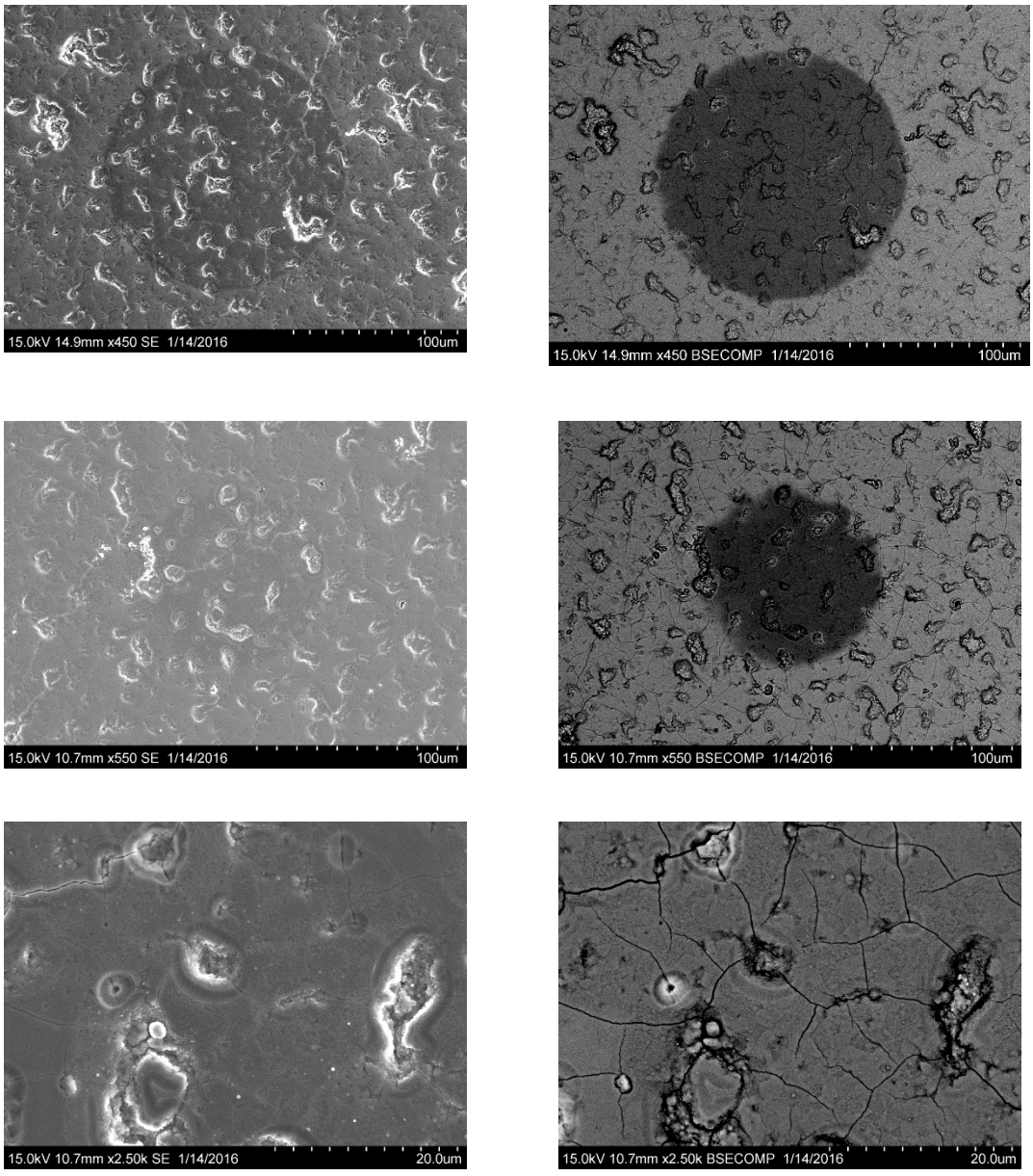

Figure 5-42. LSCF6428 microelectrode on BZY20/BZY20PLD substrate. (left) Secondary electron images. (right) Backscattered electron images.

SEM images of a LSCF6428 micro-electrodes on a BZY20 substrate with a BZY20 interlayer are shown in Figure 5-42. The left column shows images taken with a secondary electron detector sensitive to surface morphology; the right column shows images taken with

a backscatter electron detector yielding composition contrast. As can easily be seen, the interlayer was insufficient, to remove large-scale cracks and pores in the surface of the electrolyte, as the layer was on the order of 1 micron thick and the structural defects were larger. This rendered the assumption of a smooth, crack-free surface false, and analysis of the data more difficult as a result since the geometry was not as rigorously defined. As a result, triple phase boundaries are introduced into the area of the microdot electrode, and the edge boundary is not as crisply defined. Indeed, perhaps due to issues with the photolithographic film on the surface, the edges in the back-scattered electron images appear significantly distorted. This makes trends with geometry much less precise and interpretable.

Impedance results

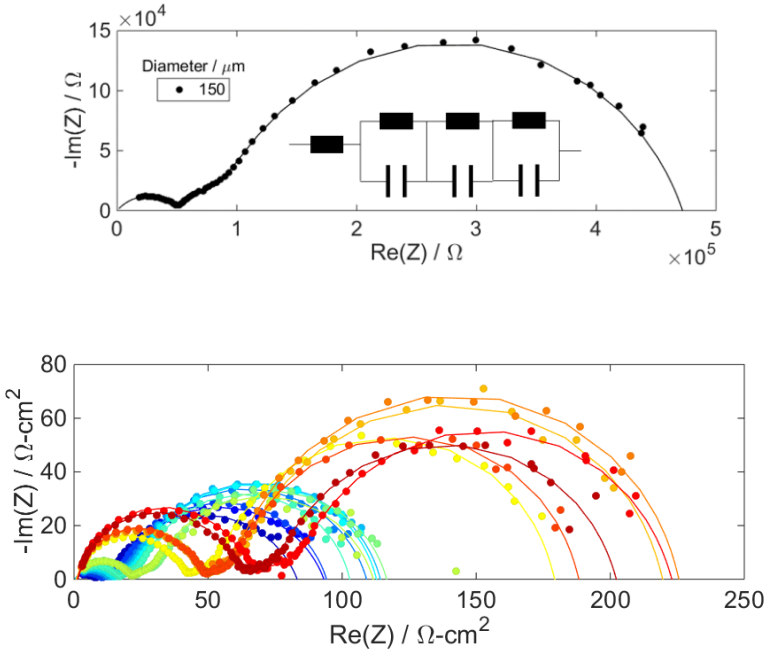

Figure 5-43. LSCF spectrum (top) and spectra over initial 24 hours (bottom).

Nyquist spectra and are shown in Figure 5-43. The spectra indicate processes with three distinguishable time constants at high-, mid-, and low-frequencies. This is similar to the spectra observed by other groups of cells containing LSCF[13]. Degradation was observed over the course of the first 24 hours of measurement as seen in the bottom figure, where the colors shift from blue to yellow to red as time progresses, but the spectra subsequently stabilized. The circuit model used to fit this data was an RRQRQRQ circuit, capturing all three of these distinct processes. Although the fits capture the behavior of the arc quite well, the use of so many fit parameters makes it very difficult to assign physically interpretable meanings to each of them. As a result, the analysis that follows will consider only the total resistance as measured by the entire width of the impedance spectrum.

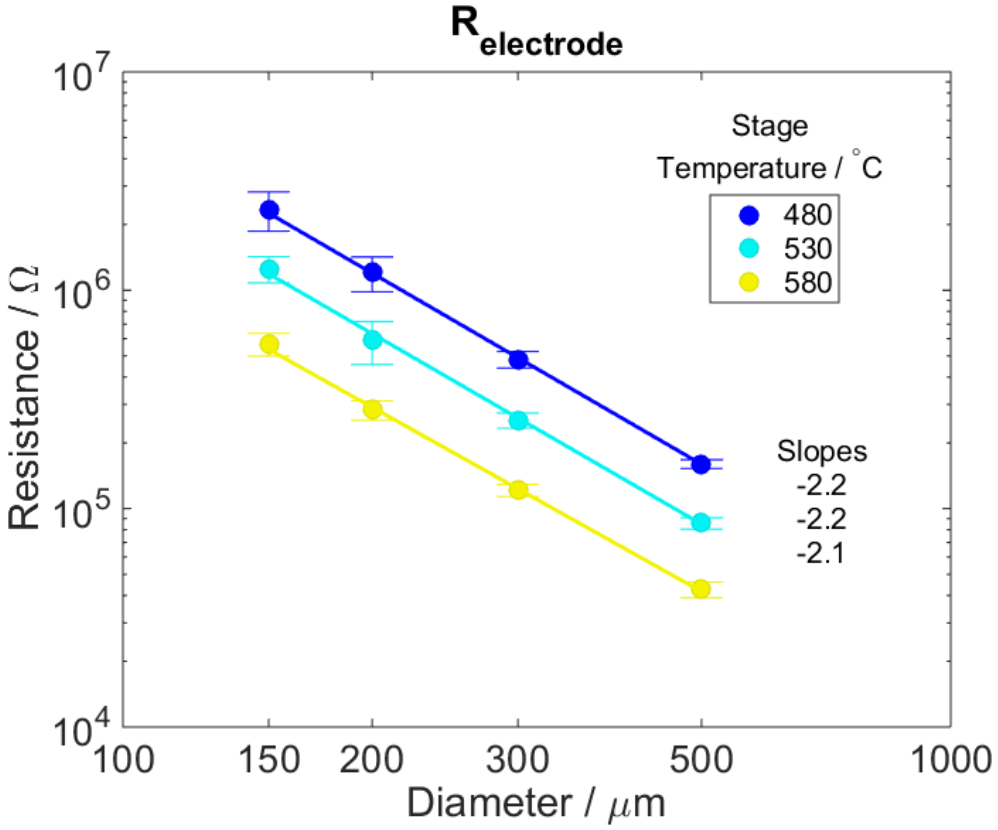

Figure 5-44. Diameter dependence of LSCF6428

The diameter dependence of the measured resistance of LSCF6428 is shown at three different temperatures in Figure 5-44. As shown on the figure, the slope near -2 suggests that LSCF may be area-limited and that, in fact, protons are being conducted through the bulk. However, as mentioned above, the cracks, pores, and poorly defined geometry give pause before definitively drawing conclusions about the proton conductivity of LSCF.

3. Composition-gradient library

Sample synthesis and characterization

In addition to microelectrodes of a single composition, a second sample was prepared with a gradient in cobalt content, analysis to the previously described samples on oxygen ion conducting substrates. This sample was measured under a limited set of environmental conditions, restricted to only one temperature (~570°C) and one oxygen atmosphere (1e-3 atm). A different electrolyte material was used (BZCYYb1711) in the hopes of yielding a smoother surface and a more well-defined film. Figure 5-45 shows a schematic of the gradient sample.

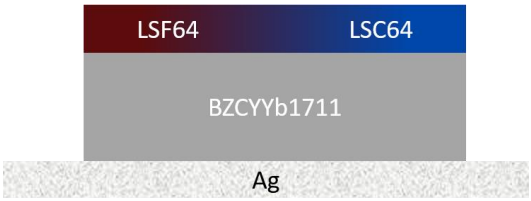

Figure 5-45. Schematic of gradient composition library sample.

Figure 5-46 shows a secondary electron image of a microelectrode from this sample library. Though some cracks remain, the cracking is much more well contained than the previous sample. Furthermore, though pores also remain, their size and dimension are less than the

previous sample as well. This sample also lacks the surface agglomerations present on the last sample that distorted the surface geometry of the micro-electrodes.

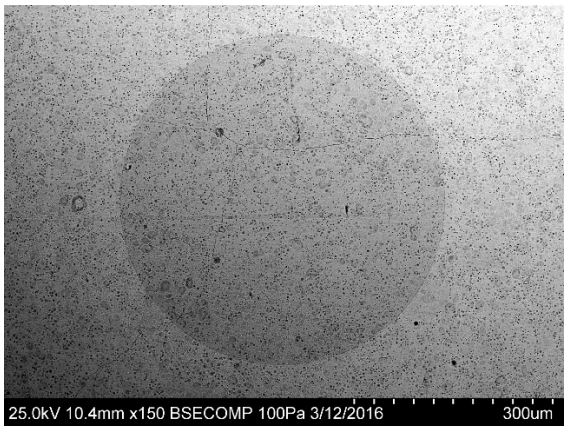

Figure 5-46. Secondary electron image of 300 μm LSCF electrode showing reduced cracking but remaining pores.

Impedance results

Nyquist plots of impedance spectra for multiple LSCF compositions are shown in Figure 5-47. The solid lines represent fits to an RRQRQ model circuit. The spectra differ slightly from those presented above for LSCF6428. Only two arcs are clearly visible – the mid-frequency arc has been either suppressed or the associated physical process is negligible under these hotter and less oxidizing conditions. In addition, the relative magnitude of the two features has changed, with the interfacial high-frequency feature now significantly smaller than the electrode arc.

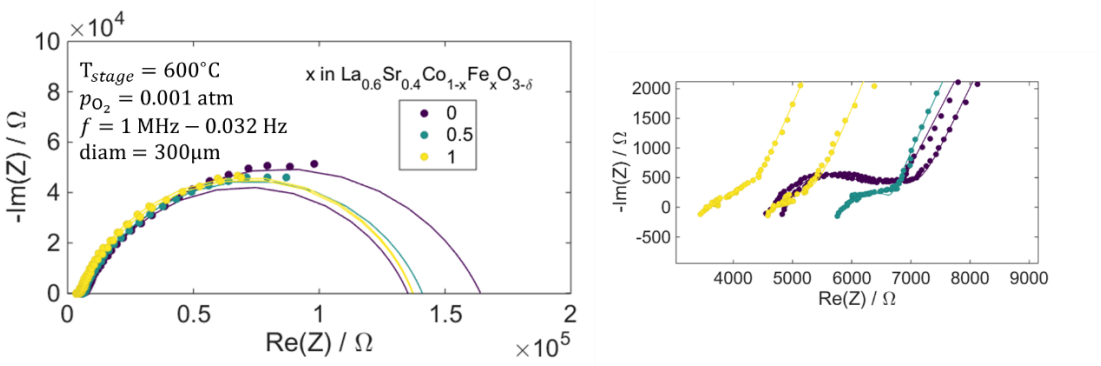

Figure 5-47. Nyquist spectra of LSCF64 microelectrodes on BZCYYb1711 substrate.

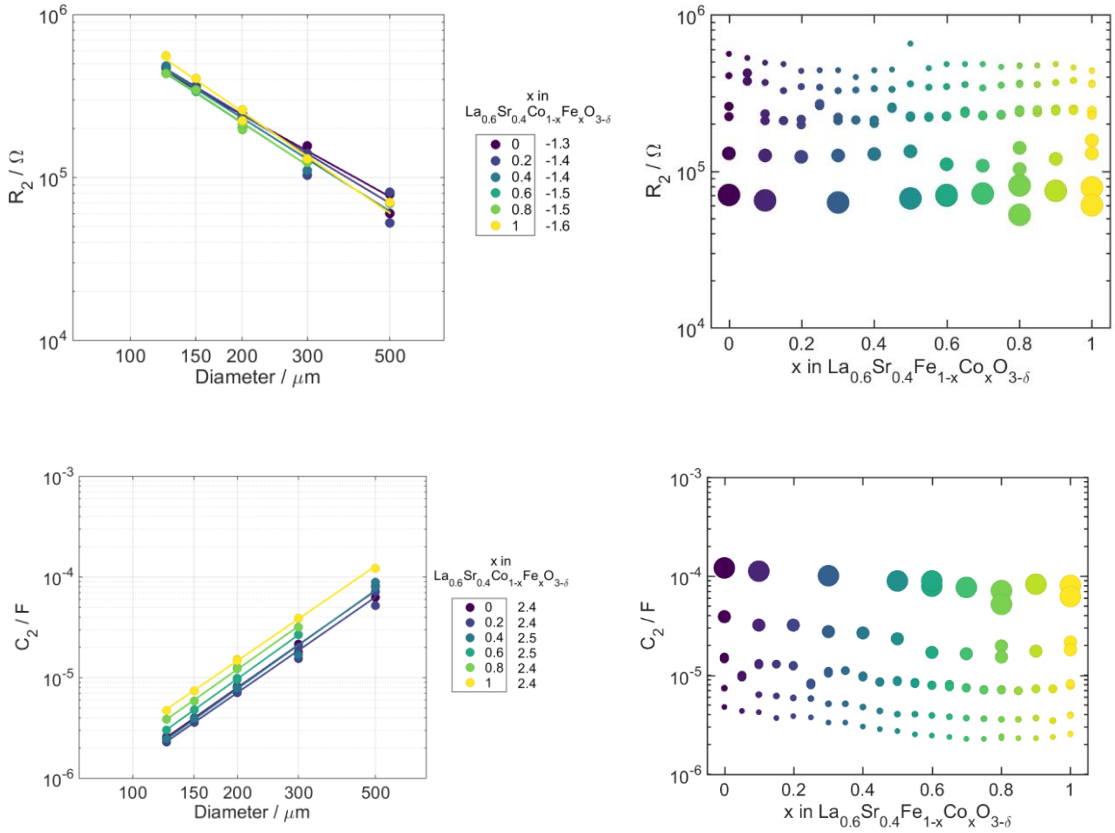

Figure 5-48. Resistance (top) and capacitance (bottom) values extracted from fits to impedance spectra as a function of diameter (left) and composition (right).

Figure 5-48 shows collective results for resistance and capacitance as extracted from RRQRQ model fits to the data. The larger values were attributed to the electrode arcs. The slope of resistance with diameter on a log-log plot is between -1 and -2, leaving interpretation difficult. If the substrate is still slightly cracked, as it was for the sample above, but less so, such a slope may manifest. Interestingly, the trend of electrode resistance with composition is relatively flat, indicating that there is not much difference in performance between the two end members on proton-conducting substrates under these conditions. Perhaps this result can be exploited to obtain better matching of other parameters like thermal expansion and reactivity by tailoring the amount of cobalt in LSCF.

The capacitance data further complicate the interpretation of this data, as the slope of capacitance with diameter falls between 2 and 3 on the loglog plot. This deviation has many possible interpretations. One interpretation is that the geometry we are measuring is not the patterned geometry, due either to mechanical issues with the substrate or contact between the electrode and the electrolyte. This variation, however, must occur uniformly for all microelectrodes as the slopes have very similar values.

4. Summary

Although measurement of cathode materials on proton-conducting substrates proved challenging, some meaningful insights were extracted from these experiments. In particular, little significant difference in the electrochemical resistance was observed across the composition spread for LSCF on a proton-conducting electrolyte. This conclusion is robust even without a perfect sample geometry, as all micro-electrodes were synthesized and measured under identical conditions. This implies that if LSCF is to be used as a cathode

material for p-SOFCs, other considerations such as thermal expansion matching should dominate the selection of a precise composition rather than activity.

5. References

1 Ricote, S., Bonanos, N., Rorvik, P. M. & Haavik, C. Microstructure and performance of La0.58Sr0.4CO0.2Fe0.8O3-delta cathodes deposited on BaCe0.2Zr0.7Y0.1O3-delta by infiltration and spray pyrolysis. *J Power Sources* **209**, 172-179, doi:10.1016/j.jpowsour.2012.02.090 (2012).

2 Fabbri, E., Bi, L., Pergolesi, D. & Traversa, E. High-performance composite cathodes with tailored mixed conductivity for intermediate temperature solid oxide fuel cells using proton conducting electrolytes. *Energ Environ Sci* **4**, 4984-4993, doi:10.1039/c1ee02361f (2011).

3 Fabbri, E., Licoccia, S., Traversa, E. & Wachsman, E. D. Composite Cathodes for Proton Conducting Electrolytes. *Fuel Cells* **9**, 128-138, doi:10.1002/fuce.200800126 (2009).

4 Yang, C. *et al.* Electrochemical properties of BaZr0.1Ce0.7Y0.1Yb0.1O3 − δ-Nd1.95NiO4 + δ composite cathode for protonic ceramic fuel cells. *International Journal of Hydrogen Energy* **40**, 2800-2807, doi:10.1016/j.ijhydene.2014.12.084 (2015).

5 Peng, R., Wu, T., Liu, W., Liu, X. & Meng, G. Cathode processes and materials for solid oxide fuel cells with proton conductors as electrolytes. *J Mater Chem* **20**, 6218-6225, doi:10.1039/C0JM00350F (2010).

6 Fabbri, E., Pergolesi, D. & Traversa, E. Electrode materials: a challenge for the exploitation of protonic solid oxide fuel cells. *Science and Technology of Advanced Materials* **11**, doi:10.1088/1468-6996/11/4/044301 (2010).

7 Sanders, M. & O'Hayre, R. Development of a multi-species transport space theory and its application to permeation behavior in proton-conducting doped perovskites. *J Mater Chem* **20**, 6271-6281, doi:10.1039/C0JM00064G (2010).

8 Shang, M., Tong, J. H. & O'Hayre, R. A promising cathode for intermediate temperature protonic ceramic fuel cells: BaCo(0.4)Fe(0.4)Zr(0.2)O3-delta. *Rsc Adv* **3**, 15769-15775, doi:10.1039/c3ra41828f (2013).

9 Duan, C. *et al.* Readily processed protonic ceramic fuel cells with high performance at low temperatures. *Science* **349**, 1321-1326, doi:10.1126/science.aab3987 (2015).

10 Poetzsch, D., Merkle, R. & Maier, J. Proton Conductivity in Mixed-Conducting BSFZ Perovskite from Thermogravimetric Relaxation. *Phys Chem Chem Phys*, doi:10.1039/c4cp00459k (2014).

11 Gryaznov, D., Merkle, R., Kotomin, E. A. & Maier, J. Ab initio modelling of oxygen vacancies and protonic defects in La1-xSrxFeO3-delta perovskite solid solutions. *Journal of Materials Chemistry A* **4**, 13093-13104, doi:10.1039/c6ta04109d (2016).

12 Poetzsch, D., Merkle, R. & Maier, J. Investigation of oxygen exchange kinetics in proton-conducting ceramic fuel cells: Effect of electronic leakage current using symmetric cells. *J Power Sources* **242**, 784-789, doi:10.1016/j.jpowsour.2013.05.108 (2013).

13 Fabbri, E., Bi, L., Tanaka, H., Pergolesi, D. & Traversa, E. Chemically Stable Pr and Y Co-Doped Barium Zirconate Electrolytes with High Proton Conductivity for Intermediate-Temperature Solid Oxide Fuel Cells. *Adv Funct Mater* **21**, 158-166, doi:10.1002/adfm.201001540 (2011).

Chapter 6

NOVEL CATHODE MATERIALS ON PROTON-CONDUCTING ELECTROLYTES

As mentioned in the previous chapter, efforts to make use of materials with the ability to conduct electrons, protons, and oxygen ions have developed only recently. As part of this development, candidate materials which may conduct protons have been identified. Such candidates include some perovskite materials such as $Ba_{0.5}Sr_{0.5}Fe_{1-x}Zn_xO_{3-\delta}$ (BSFZ)[1] and certain double perovskite materials such as, potentially, $PrBa_{0.5}Sr_{0.5}Co_2O_{5+\delta}$ (PBCO)[2]. The identification of the activity of these materials and whether they are proton conductors is vital to the continued progress of proton-conducting solid oxide fuel cell performance. The scanning impedance probe is an ideal technique for conducting such tests for its ability to rigorously compare materials performance and reliably characterize large portions of unexplored composition phase space.

In this chapter we will investigate the novel double perovskite material PBSCF for its electrochemical activity on proton-conducting electrolytes and compare the results to those obtained from measurements of LSCF in the previous chapter. An additional candidate material will be measured, $Ba(Zr_{1-x}Pr_x)_{0.8}Y_{0.2}O_{3-\delta}$ (BZPY). BZPY takes the known proton conductor BZY and transforms it into a better electron conductor through the use of the more easily reducible Pr ion. It is difficult to definitively show by many methods whether proton uptake actually occurs if proton uptake is small. For materials which are good electronic conductors, analyzing the geometry dependence of the electrochemical activity to look for a bulk pathway is one way to provide evidence of bulk proton conduction.

1. Single-composition PBSCF Library

As with the previous studies on oxygen-ion conducting electrolytes, in this study we compare the results obtained for LSCF on proton-conducting electrolytes to those obtained for PBSCF. As noted before, PBSCF forms in the double perovskite structure and may uptake more protons than LSCF due to the size of the oxygen sites near the oxygen pore channels[2]. This may lead to significant proton conductivity and thus to a two-phase boundary dominant reaction pathway.

Sample preparation

Samples of PBSCF5531 (75% cobalt, 25% iron on the B-site) were prepared by a similar method as described in previous chapters. A BZCYYb4411 pellet was used as the proton-conducting electrolyte substrate, having been polished using a 0.5 μm grit polishing cloth. A 600 nm layer of PBSCF5531 was deposited onto this substrate and the film was subsequently patterned into the same circular micro-dot electrode pattern used in previous studies, with micro-electrodes ranging in diameter from 500 μm to 30 μm. A schematic of the sample is shown in Figure 6-49.

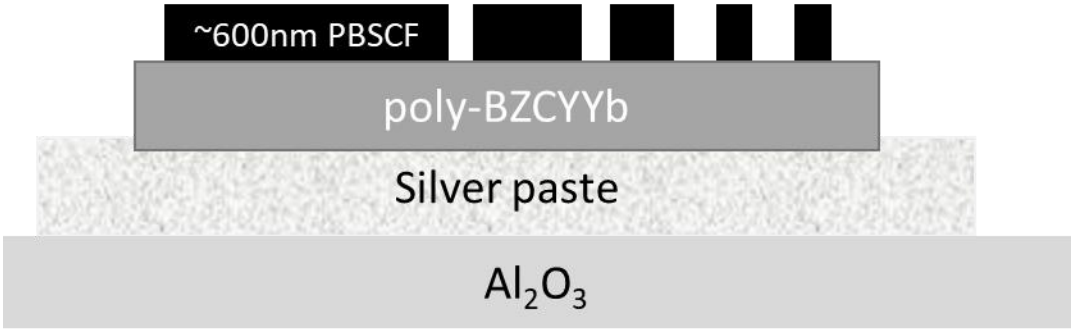

Figure 6-49. Sample schematic of PBSCF microelectrodes on BZCYYb electrolyte

Results of thin-film X-ray diffraction and atomic force microscopy are shown in Figure 6-50. Due to deposition on a polycrystalline substrate, the film is also polycrystalline, but shows good crystallinity as evidenced by the sharp peaks in the pattern. The AFM results show that the film is again significantly rougher than films grown on smooth, polished (100) YSZ. However, the roughness and peak-to-peak variation is still smaller than the film thickness, suggesting that the films are a sufficient thickness to remain continuous without the cracking observed for LSCF films in the previous chapter.

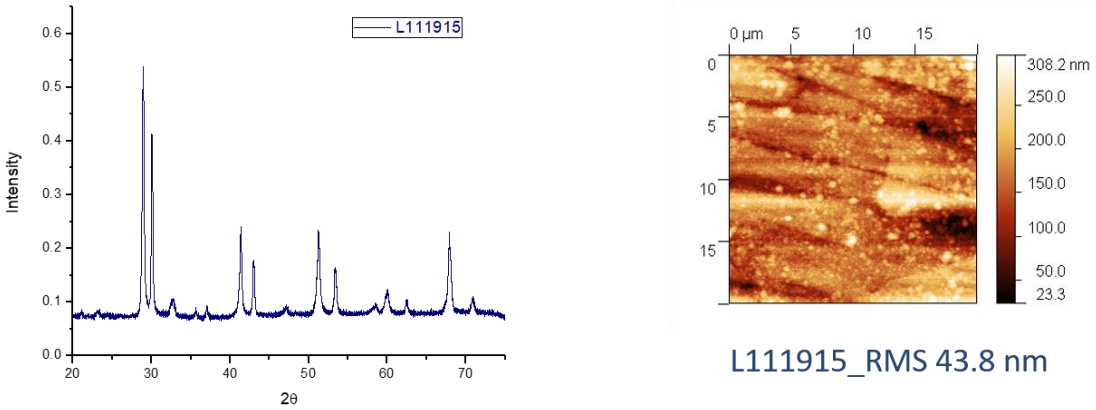

Figure 6-50. XRD pattern (left) and AFM image of surface (right) for L111915.

Measurements were carried out at a film temperature of 500°C under oxygen atmospheres ranging from 0.001 to 0.2 atm. Gas was bubbled through water held at 15°C resulting in a water partial pressure of 0.016 atmospheres. The sample was equilibrated at 500°C and 0.2 atm O_2 for 12 hours before measuring multiple microelectrodes. Impedance data were acquired from 10 kHz to 1 mHz with a 30 mV voltage perturbation using a Solartron 1260 impedance analyzer.

Impedance results

Figure 6-51 shows the results of electrochemical impedance spectroscopy on PBSCF micro-electrodes ranging in diameter from 125 μm to 300 μm on a Nyquist plot. Two distinct processes are observed, one at high frequency and another at low frequency. The spectra are fit with an RRQRQ circuit, shown as solid lines through the circular data points. At very low frequency, a potential third feature appears as a tail trailing toward higher real resistance. This tail is attributed to degradation over the course of the long low-frequency measurement and not a separate physical process.

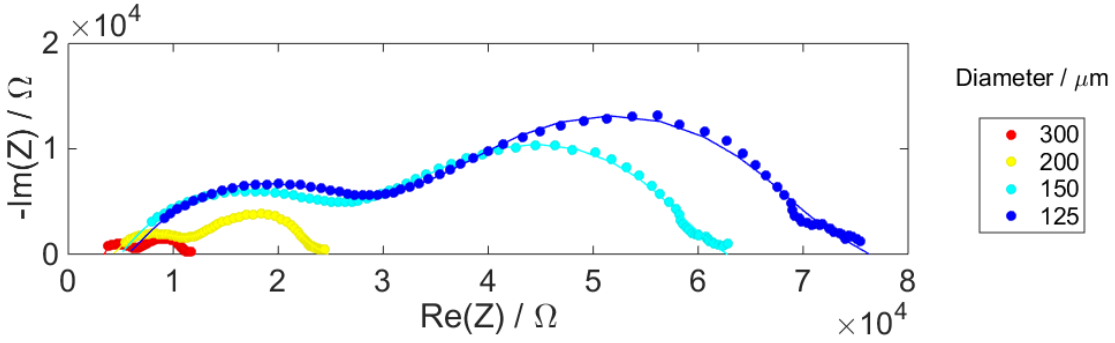

Figure 6-51. Nyquist spectra of PBSCF micro-electrodes on BZCYYb

Degradation can be attributed to this low frequency measurement because it is observed over the initial equilibration period, as shown in Figure 6-52. Nyquist spectra corresponding to repeated measurements of a single 500 μm micro-electrode during the first 12 hour equilibration period are shown in Figure 6-52. The total resistance of the microelectrode response, i.e., the total width of the impedance data from high frequency to low frequency along the real axis, increases by more than a factor of 4 during this time period. Repeated measurements of multiple micro-electrodes with varying diameters show the same trend, as

seen in Figure 6-53. Micro-dot electrodes of varying diameters show the same trend in resistance increase, the likely result of some form of degradation over the initial equilibration period, though measurements taken after this time, shown after the 15 hour mark as small clusters, appear to have stabilized within a small range.

The precise nature of this degradation was not determined, though could be caused by a limited number of factors. Reactivity between PBSCF and BZCYYb was shown to be negligible[3] and is unlikely as a major contributing factor. PBSCF was also shown to be stable under humidifying atmospheres. Coarsening of the film or delamination from the substrate could contribute to this degradation. The stability of the BZCYYb electrolyte may have contributed to this degradation if the ratios of the constituent elements were not accurate, since this material can decompose in carbon-containing atmospheres[4].

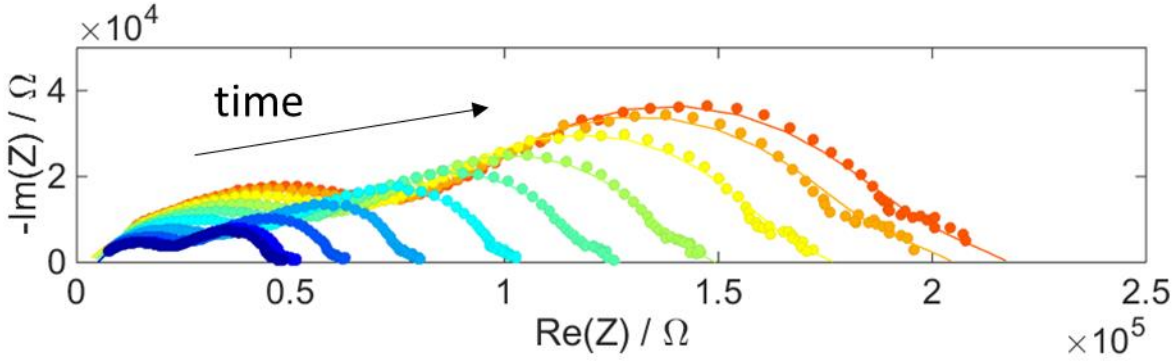

Figure 6-52. Nyquist spectra over time showing degradation in PBSCF microelectrodes.

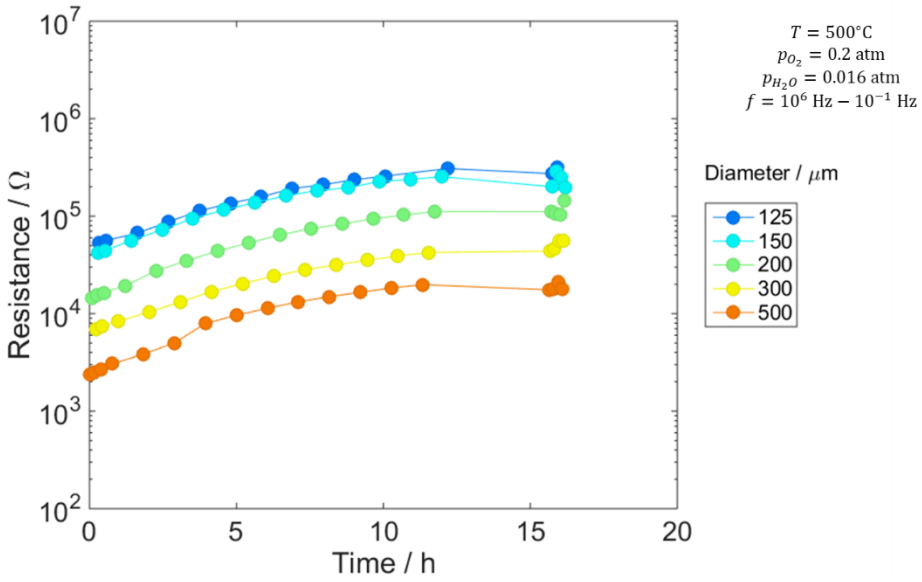

Figure 6-53. Degradation in PBSCF microelectrode resistance over time.

However, the degradation process stops after approximately 15 hours and dots measured subsequently show stable values. Measurements taken after this point in time are assumed to be at a stable state and thus enable comparisons to other compositions of electrodes measured in a similar geometry.

The dependence of resistance on diameter is shown in Figure 6-54. Several microdots measured are averaged together to calculate the measured datapoint, and the error of these multiple measurements is represented by the error bars. The error bars also incorporate in quadrature the error of the fit itself. Measurements were carried out at multiple oxygen atmospheres but a fixed water partial pressure. At each of the oxygen atmospheres, a slope of -2 is observed, indicating that PBSCF is in fact conducing protons through the surface of the microelectrode and then incorporating these protons into the bulk of the electrolyte. This

provides strong evidence that PBSCF is indeed conducting protons through the bulk and is surface-active towards oxygen reduction on a proton-conducting electrolyte.

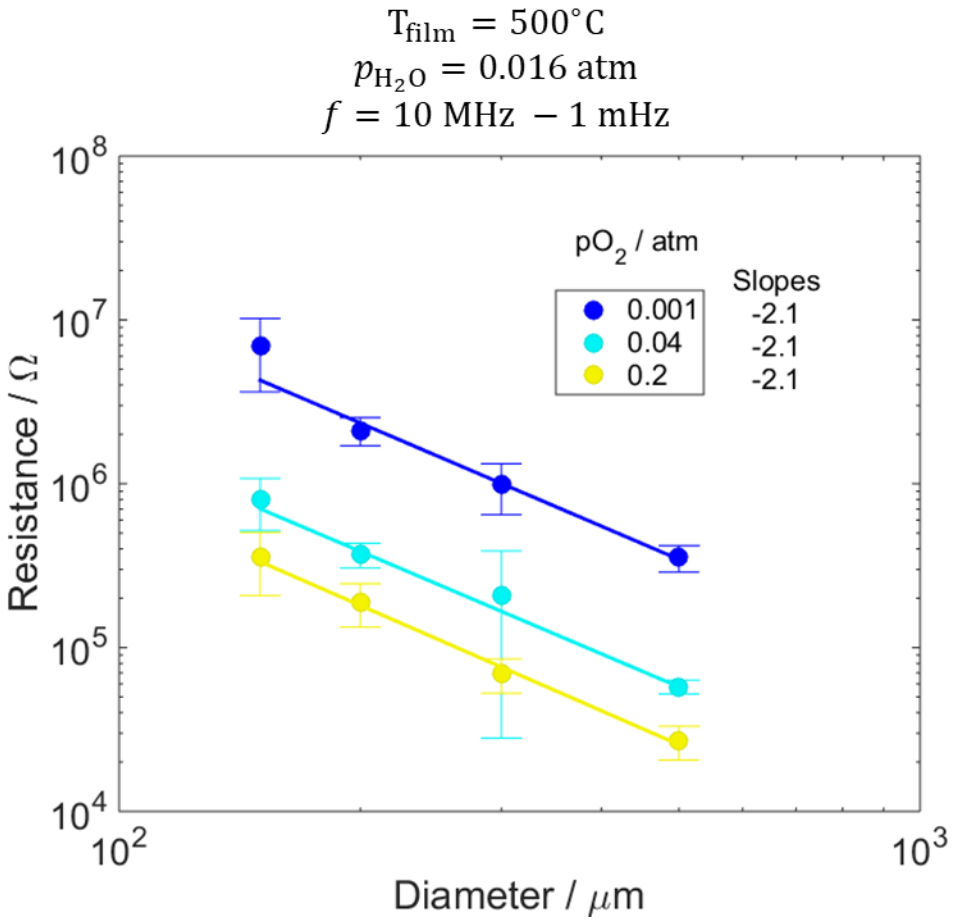

Figure 6-54. Diameter dependence of PBSCF microelectrodes at different pO2 conditions.

2. BZPY Library

Another potential triple-conducting cathode material is $Ba(Zr_{1-x}Pr_x)_{0.8}Y_{0.2}O_{3-\delta}$. By doping praseodymium onto the zirconium site, electronic conductivity is improved[5-8]. However, it is not known whether there is sufficient electronic conductivity for BZPY to behave as a

mixed conductor in the thin film geometry, where substantial electronic conductivity is required in order to conduct electron in the thin film to all areas on the thin film surface.

A schematic of the BZPY gradient is shown in Figure 6-55. A linear gradient between BZY and BPY was deposited on a polycrystalline BZCYYb substrate. This substrate was then adhered using silver paste to an alumina substrate. The porous silver paste was used as the counter-electrode. The sample was then heated to a stage temperature of 530°C and a water partial pressure of 0.016 atm corresponding to a bubbler temperature of 15°C.

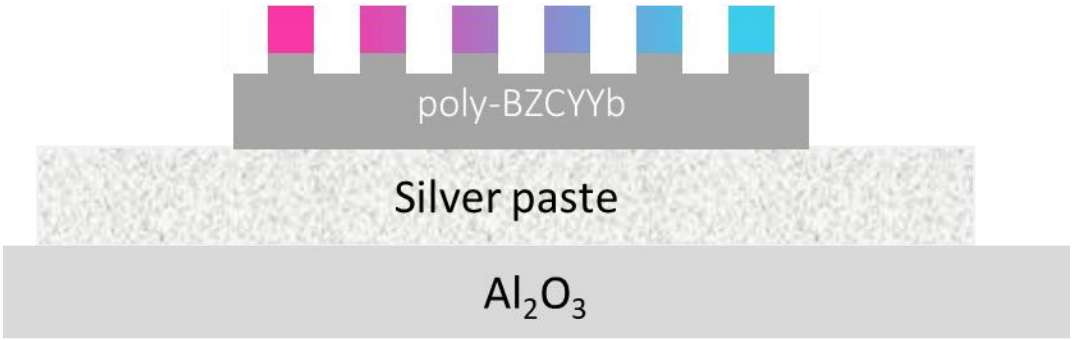

Figure 6-55. Sample schematic of BZPY microelectrodes.

Figure 6-56 shows Nyquist spectra collected at a film temperature of 500°C and a pO_2 of 0.2 atm. The left figure shows Nyquist spectra collected for dots of different diameters for microelectrodes with a composition of 90% Pr. Two consistent features are observed, a low-frequency arc and a high-frequency arc, with the low-frequency feature corresponding to oxygen reduction and the high-frequency feature likely to interfacial factors or sheet resistance. Furthermore, the magnitude of the resistance for all spectra are quite similar, indicating an interesting lack of geometric variation. The right figure shows the Nyquist spectra collected from micro-electrodes with varying Pr content, from x=0.5 to x=1. Both

the low-frequency and high-frequency portions of the spectra increase in width with decreasing Pr content, indicating that the electronic conductivity of the material plays a significant role in determining its activity toward reduction.

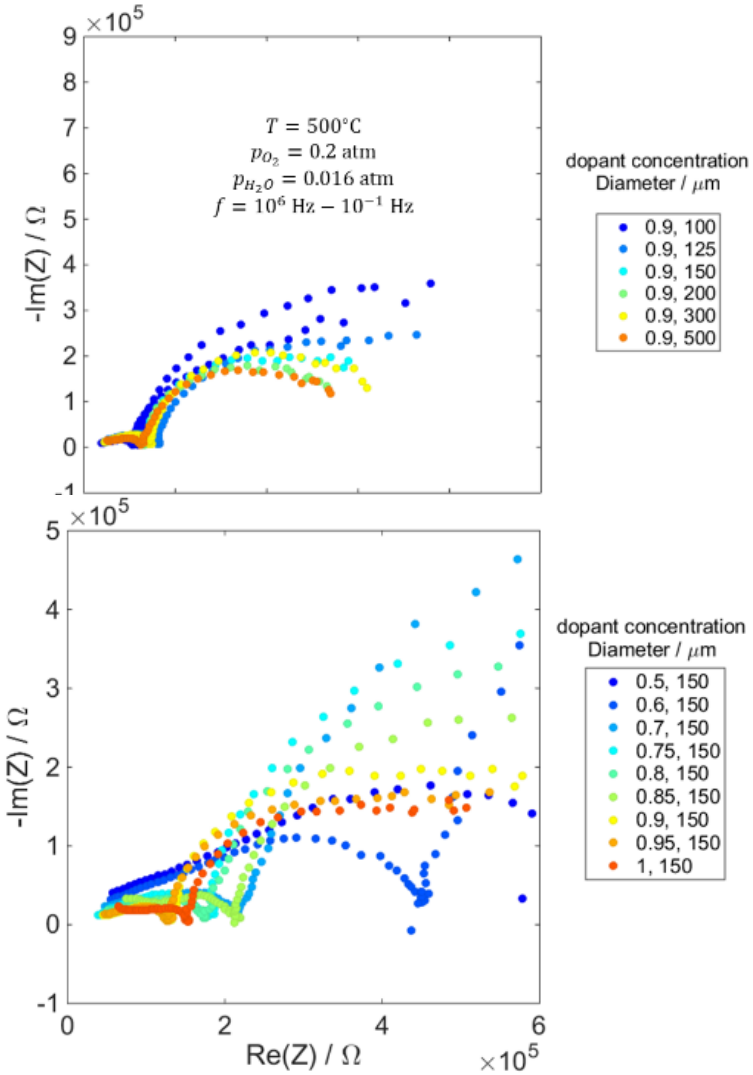

Figure 6-56. Nyquist spectra for BZPY microelectrodes. (left) multiple diameter microelectrodes at one composition, (right) multiple compositions at 150 um

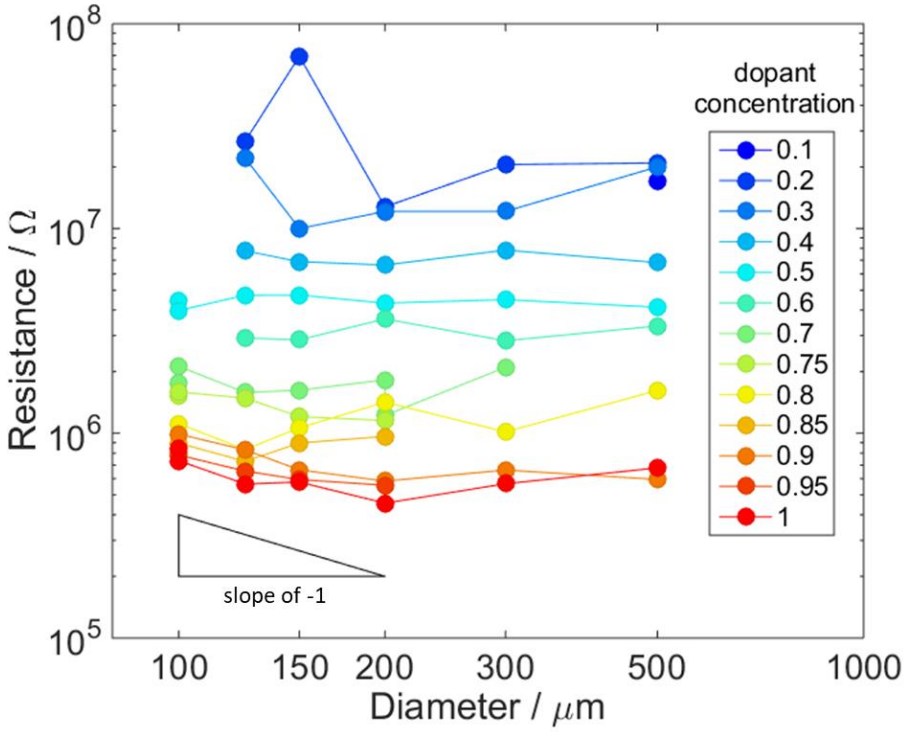

Figure 6-57. Resistance vs diameter for all microelectrode compositions.

Figure 6-58 shows the geometry dependence of the electrochemical resistance for all compositions. For microelectrodes with a diameter larger than 150 µm, the magnitude of the resistance is roughly equivalent for all diameters. This interesting result suggests that there is insufficient electronic conductivity in the BZPY to conduct electron to the outer portions of the thin film, and all electrochemical activity is thus limited to a small region around the probe tip. This is also consistent with the trend with composition, where the BPY end-member has the lowest electrochemical resistance and the highest electronic conductivity as compared with the BZY.

3. Comparison Summary

A summary comparing the electrochemical performance of all measured materials on proton-conducting substrates is shown in Figure 6-58 below. The performance of PBSCF, measured as electrochemical resistance, is significantly better than that of LSCF or BZPY. Though the LSCF line obeys a slope close to -2, recall that this was due to the cracked substrate creating multiple triple phase boundaries on the interior of the micro-electrode, and does not reflect that LSCF serves as a sufficient conductor of protons to enable the two-phase-boundary pathway. In any case, PBSCF outperforms LSCF and BZPY in an identical geometry, indicating it is better suited toward p-SOFCs than the latter two materials.

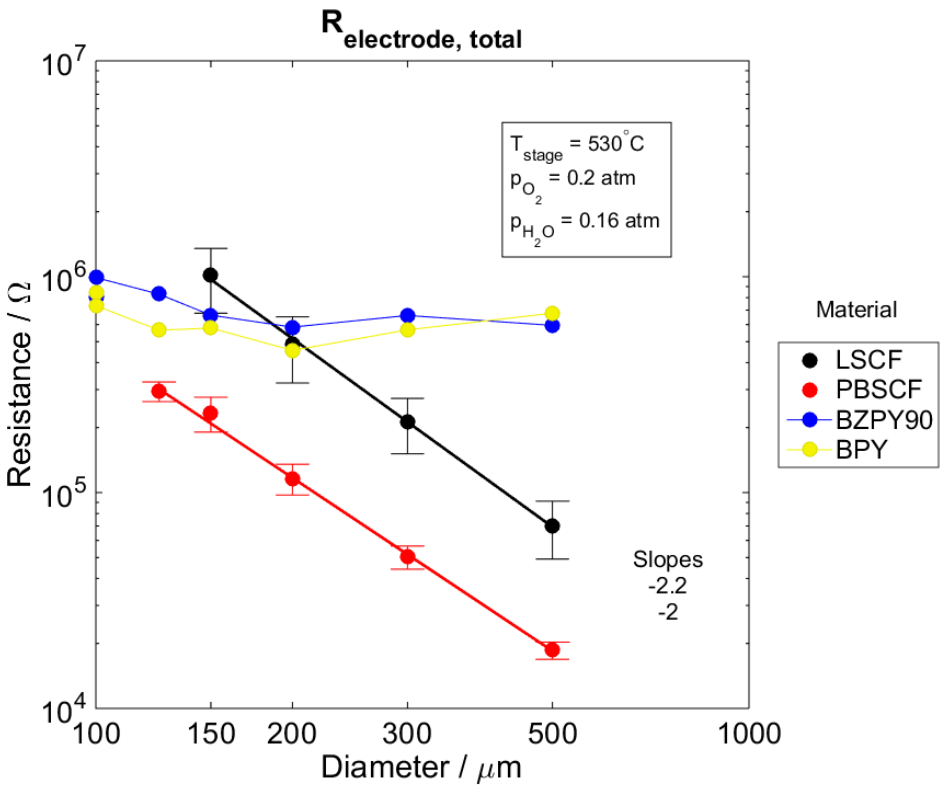

Figure 6-58. Summary of electrode activity on proton-conducting substrates.

4. Application to devices

With evidence suggesting that PBSCF exhibits both higher activity and, potentially, sufficient proton conductivity to be two-phase boundary limited, this material was tested in a real fuel cell device[3]. Anode-supported fuel cells were fabricated by Dr. Sihyuk Choi by lightly sintering a Ni-BZCYYb4411 substrates and drop-casting a thin film of BZCYYb4411 electrolyte. The resulting half-cell was sintered at 1550°C to form a dense electrolyte layer approximately 10μm thick. A porous PBSCF5531 layer was then applied via paste and then sintered. The fuel cell was sealed to an alumina tube using Ceramabond, and humidified hydrogen and synthetic air were fed to the anode and cathode respectively. The results of these fuel cell tests are shown in Figure 6-59 below. The fuel cell shows an excellent power density exceeding 1 W/cm^2 at 650°C.

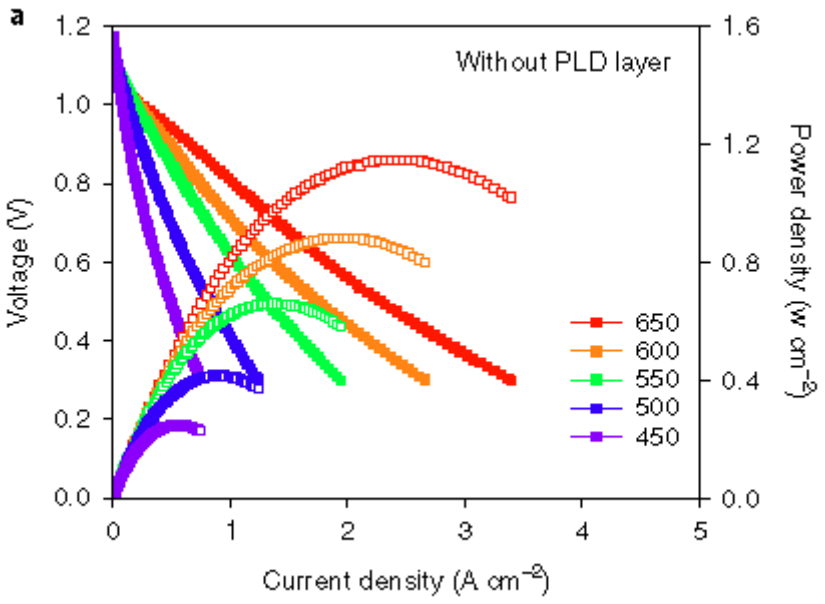

Figure 6-59. I-V curves of fuel cell without PBSCF PLD interlayer.

Encouraged by these results, it was observed that the ohmic offset of the cell was far beyond its theoretical value and postulated that this large ohmic resistance may be due to poor contact between the cathode and electrolyte. Poor contact would restrict the cross-sectional area of charge flow and thus increase ohmic resistance. To improve the contact between the porous PBSCF cathode layer and the BZCYYb electrolyte, a thin layer of PBSCF was deposited by PLD. The resulting I-V curves are shown in Figure 6-60 below.

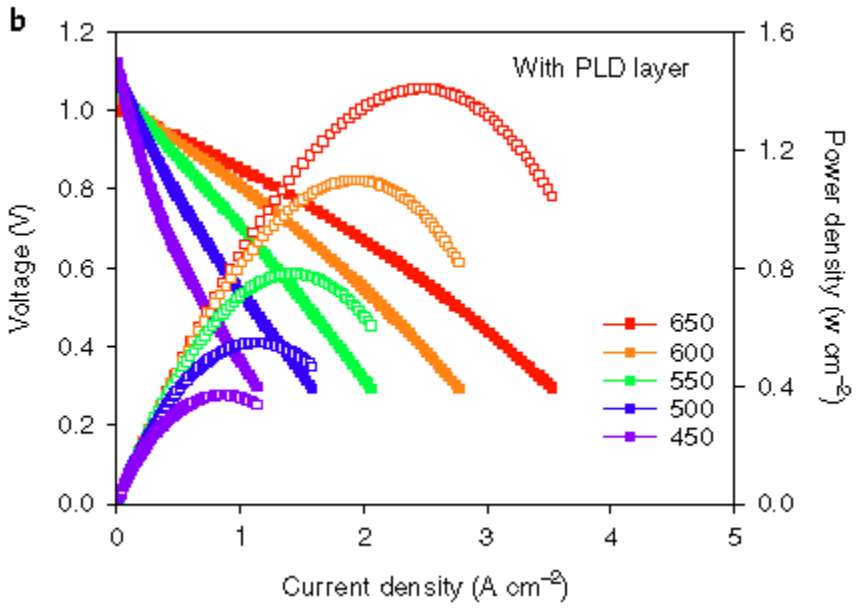

Figure 6-60. I-V curves of fuel cell without PBSCF PLD interlayer.

The observed peak power density improves by more than 20% at each temperature measured, and at 500°C exceeds 500mW/cm^2. The primary source of the enhancement was a decrease in ohmic offset is shown in Figure 6-61, showing the impedance spectrum collected from the fuel cell on a Nyquist plot comparing the cell with a PLD interlayer to that without a PLD interlayer. The spectrum looks as though it has directly shifted to a smaller offset while maintaining nearly identical arc width corresponding to electrochemical resistance. This

confirms the microprobe evidence suggesting PBSCF exhibits sufficient proton conductivity to serve as a bulk proton interlayer in a thin-film geometry.

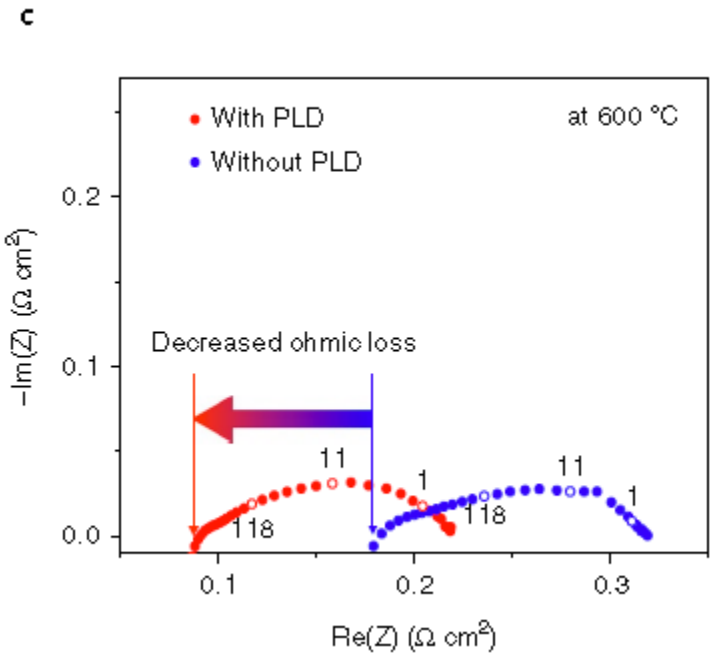

Figure 6-61. Impedance spectra of fuel cells with and without a PLD interlayer of PBSCF on the cathode.

5. Summary

In this chapter, we observed the powerful impact that the experimental technique outlined in this thesis can have on real devices. Through a high-throughput investigation of thin-film PBSCF, it was determined that this material may have sufficient proton conductivity to serve as a bulk proton conductor. When the material was applied in just such a way, a 20% increase in power density was observed. This result shows the great promise that this high-throughput experimental technique displays for future investigation and discovery of fuel cell materials.

6. References

1 Poetzsch, D., Merkle, R. & Maier, J. Proton Conductivity in Mixed-Conducting BSFZ Perovskite from Thermogravimetric Relaxation. *Phys Chem Chem Phys*, doi:10.1039/c4cp00459k (2014).

2 Téllez Lozano, H., Druce, J., Cooper, S. J. & Kilner, J. A. Double perovskite cathodes for proton-conducting ceramic fuel cells: are they triple mixed ionic electronic conductors? *Science and Technology of Advanced Materials* **18**, 977-986, doi:10.1080/14686996.2017.1402661 (2017).

3 Choi, S. *et al.* Exceptional power density and stability at intermediate temperatures in protonic ceramic fuel cells. *Nature Energy* (2018).

4 Medvedev, D. *et al.* BaCeO3: Materials development, properties and application. *Progress in Materials Science* **60**, 72-129, doi:DOI 10.1016/j.pmatsci.2013.08.001 (2014).

5 Fabbri, E., Bi, L., Tanaka, H., Pergolesi, D. & Traversa, E. Chemically Stable Pr and Y Co-Doped Barium Zirconate Electrolytes with High Proton Conductivity for Intermediate-Temperature Solid Oxide Fuel Cells. *Adv Funct Mater* **21**, 158-166, doi:10.1002/adfm.201001540 (2011).

6 Fabbri, E., Bi, L., Rupp, J. L. M., Pergolesi, D. & Traversa, E. Electrode tailoring improves the intermediate temperature performance of solid oxide fuel cells based on a Y and Pr co-doped barium zirconate proton conducting electrolyte. *Rsc Adv* **1**, 1183-1186, doi:10.1039/c1ra00545f (2011).

7 Fabbri, E., Bi, L., Pergolesi, D. & Traversa, E. High-performance composite cathodes with tailored mixed conductivity for intermediate temperature solid oxide fuel cells using proton conducting electrolytes. *Energ Environ Sci* **4**, 4984-4993, doi:10.1039/c1ee02361f (2011).

8 Stokes, S. J. & Islam, M. S. Defect chemistry and proton-dopant association in BaZrO3 and BaPrO3. *J Mater Chem* **20**, 6258-6264, doi:10.1039/C0JM00328J (2010).

Chapter 7

CONCLUSION

1. Summary

In this thesis, the application of a high-throughput materials characterization technique to solid oxide fuel cell electrode materials has led to rigorous comparisons of materials performance, both within and between families of compositions. The experiments carried out have yielded important fundamental insights that demonstrated impact on real-world devices. The work in this thesis contains measurements with perhaps the highest resolution in composition ever recorded for SOFC electrode materials.

When investigating LSCF on an oxygen-ion conducting electrolyte substrate, a rigorous quantitative comparison between the area-specific resistance of the end-member compositions was determined. This difference, a factor of 4 at intermediate temperatures, demonstrated that the ionic conductivity of the material did not appear to have a significant effect on the measured activity in this morphology, and hence the amount of strontium might be reduced to mitigate cation segregation and improve activity. A similar study of PBSCF yielded a direct comparison between the activity of these two materials on oxygen-ion conducting electrolytes. Though a significant difference in electrochemical activity was not observed between these two materials, this was likely due to the effect of orientation on the bulk ion transport of PBSCF, as the ion-conducting channels may not have been properly oriented for maximal ion transport. In addition, the enhancement of chemical capacitance in

PBSCF relative to LSCF warrants further study into the mechanism of non-stoichiometry in these double perovskite materials.

A meaningful difference was found between the performance of PBSCF and LSCF on proton-conducting substrates. Though the geometry dependence of LSCF electrodes on p-SOFC electrolytes proved inconclusive, by observing the geometry dependence of the electrochemical resistance of PBSCF micro-electrodes evidence for a bulk proton conducting pathway was established. These insights led to significant performance improvement in a real device through the use of a dense contact layer that reduced ohmic losses.

Thus, the application of this technique to two known electrode materials, one well studied and the other novel, led to key insights vital to the commercial development of these devices.

In summary, this work confirmed the viability of exploring gradient material compositions in this way, gave further insight into a previously well-studied material by investigating it in a new way, and compared the performance of multiple materials compositions on multiple electrolytes, eventually giving rise to a high-performance fuel cell based on a new proton-conducting electrode material.

2. Future Work

While this work represents an important step forward in the way cathode materials are studied, more work needs to be done. The next logical step would be the application of this technique to new materials systems, in particular complex co-doping and inter-doping of materials families. One material which particularly stands out for future study is $SrCo_{1-x}Nb_xO_{3-\delta}$. This material was shown to exhibit performance on par with the most active

compound yet discovered, BSCF[1]. Since it contains only strontium on the A-site, it is less subject to cation segregation that plagues materials such as LSCF. Furthermore, increased doping with niobium should eventually lead to a more insulating material, and a local maximum in performance is expected. With the high composition resolution this technique allows, it is the perfect way to optimize such materials.

Furthermore, future studies should carry out the measurement of cathode materials under more realistic operating conditions, specifically under bias. Biased measurements of different materials have yielded vastly different performance[2]. Performing measurements under bias will help better correlate device performance to cathode measurement.

Finally, the extension of this technique to other SOFC materials could help in the same manner as it has for cathodes. For instance, the high-throughput study of electrolyte materials could aid in optimizing electrolyte compositions or discovering new ion conductors entirely.

3. References

1 Zhou, W., Shao, Z. P., Ran, R., Jin, W. Q. & Xu, N. P. A novel efficient oxide electrode for electrocatalytic oxygen reduction at 400-600 degrees C. *Chem Commun*, 5791-5793, doi:Doi 10.1039/B813327a (2008).

2 Baumann, F. S. *et al.* Quantitative comparison of mixed conducting SOFC cathode materials by means of thin film model electrodes. *J Electrochem Soc* **154**, B931-B941, doi:Doi 10.1149/1.2752974 (2007).

APPENDIX A: EQUIVALENT CIRCUIT MODEL EQUIVALENCE

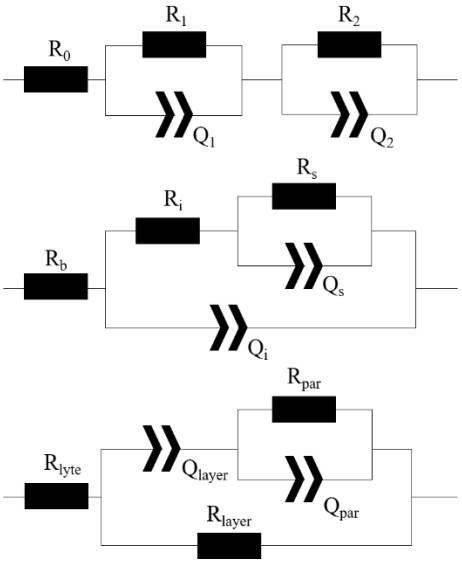

Figure A1-62. (a) R(RQ)(RQ) circuit (after Crumlin et al.). (b) Circuit derived from transmission line model after Baumann et al. (c) Model from Boukamp et al.

Both the circuit models derived by Boukamp et al.[1] and Baumann et al.[2] are mathematically equivalent to an R(RC)(RC) circuit when perfect capacitors are used rather than constant phase elements.

An R(RC)(RC) circuit consists of an offset resistance R_0 and two parallel R/C circuits R_1/C_1 and R_2/C_2. This circuit is often fitted to impedance spectra which contain two processes with distinguishable time constants. The impedance of this circuit is calculated as

$$Z(\omega) = R_0 + \left(\frac{1}{R_1} + i\omega C_1\right)^{-1} + \left(\frac{1}{R_2} + i\omega C_2\right)^{-1} = R_0 + \frac{R_1 + R_2 + i\omega R_1 R_2 (C_1 + C_2)}{1 - \omega^2 R_1 C_1 R_2 C_2 + i\omega (R_1 C_1 + R_2 C_2)} \qquad A1.1$$

The Baumann circuit contains five parameters: R_b, equivalent to the offset resistance; R_i, attributed to ion transfer across the cathode/electrolyte interface; R_s, attributed to the electrode surface reaction; C_i, the interfacial capacitance; and C_{chem}, the chemical capacitance. The impedance of the Baumann circuit is calculated as

$$Z(\omega) = \left(i\omega C_i + \left(R_i + \left(\frac{1}{R_s} + i\omega C_s \right)^{-1} \right)^{-1} \right)^{-1} = \frac{R_s + R_i + i\omega R_i R_s C_s}{1 - \omega^2 R_s C_s R_i C_i + i\omega(R_i C_i + R_s C_i + R_s C_s)} \qquad A1.2$$

The Boukamp circuit also contains five parameters: R_{lyte}, the electrolyte resistance; R_{layer} (R_l), the dc resistance; R_{par} (R_p), a resistance attributed to secondary phase formation; C_{layer} (C_l), the chemical capacitance; and C_{par} (C_p), the capacitance associated with secondary phase formation. The impedance for the Boukamp circuit is calculated as

$$Z(\omega) = \left(\frac{1}{R_l} + \left(\frac{1}{i\omega C_l} + \left(\frac{1}{R_p} + i\omega C_p \right)^{-1} \right)^{-1} \right)^{-1} = \frac{R_l + i\omega R_l R_p (C_l + C_p)}{1 - \omega^2 R_l C_l R_p C_p + i\omega \left(R_p C_p + (R_l + R_p) C_l \right)} \qquad A1.3$$

A system of equations to solve for the parameters in the Baumann and Boukamp circuits can be established by matching terms. Specifically, five sets of equations for the five unknowns are created by matching (1) the offset resistances, (2) real terms in the numerator, (3) terms

with $i\omega$ in the numerator, (4) terms with ω^2 in the denominator, and (5) terms with $i\omega$ in the denominator. Doing so yields:

Matching A1.1 to A1.2		Matching A1.1 to A1.3	
$R_b = R_0$	$A1.4$	$R_{el'lyte} = R_0$	$A1.5$
$R_s + R_i = R_1 + R_2$	$A1.6$	$R_l = R_1 + R_2$	$A1.7$
$R_i R_s C_s = R_1 R_2 (C_1 + C_2)$	$A1.8$	$R_l R_p (C_l + C_p) = R_1 R_2 (C_1 + C_2)$	$A1.9$
$R_s C_s R_i C_i = R_1 C_1 R_2 C_2$	$A1.10$	$R_l C_l R_p C_p = R_1 C_1 R_2 C_2$	$A1.11$
$R_i C_i + R_s C_i + R_s C_s = R_1 C_1 + R_2 C_2$	$A1.12$	$R_p C_p + (R_l + R_p) C_l = R_1 C_1 + R_2 C_2$	$A1.13$

This can be solved for each of the parameters in terms of the parameters for the RRCRC circuit, proving equivalence.

$R_b = R_0$	$A1.4$	$R_{el'lyte} = R_0$	$A1.5$
$R_i = \frac{R_1 R_2 (C_1 + C_2)^2}{C_1^2 R_1 + C_2^2 R_2}$	$A1.14$	$R_{layer} = R_1 + R_2$	$A1.7$
$C_i = \frac{C_1 C_2}{C_1 + C_2}$	$A1.15$	$C_{layer} = \frac{R_1^2 C_1 + R_2^2 C_2}{(R_1 + R_2)^2}$	$A1.16$
$R_s = \frac{(R_1 C_1 - R_2 C_2)^2}{C_1^2 R_1 + C_2^2 R_2}$	$A1.17$	$R_{par} = \frac{R_1 R_2 (R_1 + R_2)(R_1 C_1 - R_2 C_2)^2}{(R_1^2 C_1 + R_2^2 C_2)^2}$	$A1.18$

$C_{chem} = \frac{(C_1^2 R_1 + C_2^2 R_2)^2}{(C_1 + C_2)(R_1 C_1 - R_2 C_2)^2}$ A1.19	$C_{par} = \frac{C_1 C_2 (R_1^2 C_1 + R_2^2 C_2)}{(R_1 C_1 - R_2 C_2)^2}$ A1.20

Indeed, as can be noted for the equations for the Boukamp circuit, if $R_2 \gg R_1$ and then $R_{layer} \approx R_2$, $C_{layer} \approx \frac{R_2^2 C_2}{R_2^2} = C_2$, $R_{par} \approx \frac{R_1 R_2^2 (R_2 C_2)^2}{(R_2^2 C_2)^2} = R_1$, and $C_{par} \approx \frac{C_1 C_2 (R_2^2 C_2)}{(R_2 C_2)^2} = C_1$, confirming the approximate equivalence observed between fits to the RRQRQ circuit model and fits to the Boukamp model. For the Maier circuit, however, if $R_2 \gg R_1$ then $R_s \approx \frac{(R_2 C_2)^2}{R_2 C_2^2} = R_2$, $C_{chem} \approx \frac{(R_2 C_2^2)^2}{(C_1 + C_2)(R_2 C_2)^2} = \frac{C_2^2}{C_1 + C_2}$, $R_i \approx R_1 \frac{(C_1 + C_2)^2}{C_2^2}$, and $C_i = \frac{C_1 C_2}{C_1 + C_2}$. Therefore, the measured surface reaction resistance will be approximately the same, but the value for the chemical capacitance is convoluted with the value of the interfacial capacitance and vice versa. This leads to different calculated values for these parameters between studies.

When the capacitors are replaced with constant phase element such that $C_{eff} = Y^{\frac{1}{n}} R^{\frac{1}{n}-1}$, there are too many unknowns and the precise equivalence between the circuits breaks down. The behavior changes as well, since the *n* parameter in the Baumann circuit will be correlated with the *n* parameter of the surface resistance arc while the opposite will be true for the Boukamp circuit.

1 Boukamp, B. A., Hildenbrand, N., Bouwmeester, H. J. M. & Blank, D. H. A. Impedance of thin film cathodes: Thickness and current collector dependence. *Solid State Ionics* **283**, 81-90, doi:10.1016/j.ssi.2015.10.013 (2015).

2 Baumann, F. S., Fleig, J., Habermeier, H. U. & Maier, J. Impedance spectroscopic study on well-defined (La,Sr)(Co,Fe)O3-delta model electrodes. *Solid State Ionics* **177**, 1071-1081, doi:DOI 10.1016/j.ssi.2006.02.045 (2006).

APPENDIX B: MATLAB CODE

1. customImpedanceFit

This function fits an impedance model to a given impedance spectrum. Helper functions Circuits and WeightedArcFitting are also included.

```
function [medianFitParams] = ...
    customImpedanceFit(runs,  circuitVersion,  startingParams,  freqRange,
...
    sampleDir, fitFolderName)
% CUSTOMIMPEDANCEFIT Fits impedance data to a user-defined circuit
% INPUTS
%   runs            vector of run structs
%   circuitVersion  string of version of circuit to use
%   startingParams  Starting points for fit parameters
%   freqRange       Two-element array indicating min and max of freq range
%                   Input 'all' for all frequencies
%   folderName      Full path to where sim files are written
%   name            Filename of summary to write fit summary file
% OUTPUTS
%   medianFitParams      - fitted parameters
% EXAMPLES
%   custom_impedance_fit(runs, 'RRQ', [100 1000 1e-6 0.9], [1e0 1e3], ...
%                              'Sample1', 'fits_650_rrq');
%   This example fits runs contains in the struct 'runs' using the starting
%   parameters [100, 1000, 1e-6, 0.9] and fitting points in the frequency
%   range [1e0, 1e3]. It writes the fitted data to the fits_650_rrq
%   folder in the Sample1 directory


%% Set up lsqnonlin parameters

% Set the fitting function options
opts = optimoptions('lsqnonlin', ...
    'TolX', 1E-15, ...
    'TolFun', 1E-15, ...
    'MaxIter', 1000, ...
    ...'PlotFcns', {@optimplotx, @optimplotstepsize}, ...
    ...'Display', 'off', ...
    'MaxFunEvals', 50000);

weighting = 'modulus'; % 'unit', 'proportional', 'modulus'
writeToFile = 1;
makePlots = 0;
verbose = 1;

if(strcmp(freqRange, 'all'))
    freqRange = [0, Inf];
end
if(ismac)
    slash = '/';
```

```
    newline = '\n';
else
    slash = '\';
    newline = '\r\n';
end
%% Choose the circuit
switch(circuitVersion)
    case 'R'
        pNames      = {'R'};
        lowerBounds = 1;
        upperBounds = Inf;
    case 'RL'
        pNames      = {'R', 'L'};
        lowerBounds = [0 0];
        upperBounds = [Inf Inf];
    case 'RRQ'
        pNames         = {'R0', 'R1',  'Y1', 'n1'};
        lowerBounds    = [   1,    1,    0,  0.0];
        upperBounds    = [ Inf,  Inf,   Inf,  1.0];
    case 'RRQRQ'
        pNames         = {'R0', 'R1',  'Y1', 'n1',  'R2',  'Y2', 'n2'};
        lowerBounds    = [  1,    1,    0,  0.0,    1,    0,  0.0];
        upperBounds    = [ Inf,  Inf,   Inf,  1.0,   Inf,   Inf,  1.0];
    case 'RRQRQRQ'
        pNames          = {'R0', 'R1',  'Y1', 'n1',  'R2',  'Y2', 'n2',
'R3', 'Y3', 'n3'};
        lowerBounds    = [   1,    1,    0,  0.0,      1,     0,  0.0,
1,    0,  0.0];
        upperBounds    = [ Inf,  Inf,  Inf,  1.0,    Inf,   Inf,  1.0,
Inf,  Inf,  1.0];
    case '6a'
        pNames         = {'Rion', 'Rion_s', 'Cion_s', 'Cchem', 'Ceon_p',
'R0'};
        lowerBounds    = [    0,        0,        0,       0,        0,
0];
        upperBounds    = [  Inf,      Inf,      Inf,     Inf,      Inf,
Inf];
    case '7b'
        pNames         = {'Rion', 'Rion_s', 'Cion_s', 'Cchem', 'Yeon_p',
'neon_p', 'R0'};
        lowerBounds    = [    0,        0,        0,       0,        0,
0.0,    0];
        upperBounds    = [  Inf,      Inf,      Inf,     Inf,      Inf,
1.0,  Inf];
    case '7c'
        pNames         = {'Rion', 'Rion_s', 'Yion_s', 'nion_s', 'Cchem',
'Ceon_p', 'R0'};
        lowerBounds    = [    0,        0,        0,       0,        0,
0.0,    0];
        upperBounds    = [  Inf,      Inf,      Inf,       1,      Inf,
Inf,  Inf];
    case 'maier2006'
        pNames                = {'R_{lyte}', 'R_{ion,int}', 'Q_{int}',
'n_{ion,int}', 'R_{ion,surf}', 'Q_{chem}', 'n_{chem}'};
        lowerBounds    = [       1,           1,        0,          0.0,
1,        0.0,        0.0];
```

```
        upperBounds     = [         Inf,              Inf,         Inf,
1.0,            Inf,        Inf,        1.0];
    case 'boukamp2015'
        pNames       = {'R_{lyte}', 'R_{layer}', 'Q_{layer}', 'n_{layer}',
'R_{par}', 'Q_{par}', 'n_{par}'};
        lowerBounds    = [        1,            1,        0,          0.0,
1,        0.0,        0.0];
        upperBounds    = [      Inf,          Inf,      Inf,          1.0,
Inf,        Inf,        1.0];
    otherwise
        error('No circuit found');
end

% Scale everything so it falls in the range 1:10
parameters = startingParams;
fitParamMatrix = zeros(length(runs), length(startingParams));
scalingFactors = 10.^floor(log10(parameters));

%% Open summary filehandle for writing
fitsSummaryFilename = [sampleDir slash fitFolderName slash fitFolderName
'.txt']
if(writeToFile)
    sumFH = fopen(fitsSummaryFilename, 'w');

    fprintf(sumFH, '"Filename"\t"Chi-Sqr"\t"Sum-Sqr"\t');
    for i = 1:length(pNames)
        head = pNames{i};
        fprintf(sumFH,   '%s(+)\t%s(Error)\t%s(Error%%)\t',   head,   head,
head);
    end
    fprintf(sumFH, '\r\n');
end
%% Do the fitting!
bar = waitbar(0, 'Initializing...');

for i = 1:length(runs)
    if runs(i).customFit == 1
        % Get frequency and impedance data in appropraite range
        simName = [sampleDir slash fitFolderName slash runs(i).filename
'.sim'];
        freqs = runs(i).Z.freq;
        fRange = getRangeIndices(freqs, freqRange);
        %closestValues = min(abs(runs(i).Z.im(fRange))); %%%
        %indexOfClosest = find(closestValues == abs(runs(i).Z.im));
        %fRange                  =                  (max(1,indexOfClosest-
1)):1:min(indexOfClosest+1,length(freqs)); %%%


        % Calculate measured and initial impedance profiles
        % But only include where Zim > 0

        posIndices = runs(i).Z.im(fRange) < 0;
        newFRange = [];
        for jj = 1:length(posIndices)
            if(posIndices(jj))
                newFRange = [newFRange; fRange(jj)];
```

```
            end
        end
        freqs = freqs(newFRange);
        if(length(freqs) < 10)
            continue;
        end

        Zmeas = [runs(i).Z.re(newFRange), runs(i).Z.im(newFRange)];
        Zinitial = Circuits(parameters, freqs, circuitVersion);

        % Scale parameters and bounds by appropriate factors
        scaledParameters = parameters ./ scalingFactors;
        scaledLowerBounds = lowerBounds ./ scalingFactors;
        scaledUpperBounds = upperBounds ./ scalingFactors;

        waitbar(i/length(runs), bar, sprintf('Fitting spectrum %d of
%d...', i, length(runs)));

        % Weighted arc Fitting 'normalizes' the parameters by dividing by
the scaling factor
        [p_out, resnorm, residuals, eflag, output, lambda, jacob] = ...
            lsqnonlin(@(ps) WeightedArcFitting(ps, scalingFactors, freqs,
circuitVersion, Zmeas, weighting), ...
            scaledParameters,   scaledLowerBounds,   scaledUpperBounds,
opts);
        fitParams = p_out .* scalingFactors;
        covar = (jacob' * jacob)^(-1);
        ci = nlparci(p_out, residuals, 'jacobian', jacob, 'alpha', 0.33);
        cLow = ci(:, 1)' .* scalingFactors;
        cHigh = ci(:, 2)' .* scalingFactors;
        %fittedFreqs = logspace(0, 8)';

        fittedFreqs = freqs;
        Zfitted = Circuits(fitParams, fittedFreqs, circuitVersion);
        fitParamMatrix(i, :) = fitParams;

        %% Plot the results
        if(makePlots)
            nyFH = figure();
            set(nyFH, 'color', 'white');
            axis square;
            set(gca, 'DataAspectRatio', [1 1 1]);

            hold on;
            plot(Zmeas(:, 1),    -Zmeas(:, 2), 'co');
            plot(Zinitial(:, 1), -Zinitial(:, 2), 'r--');
            plot(Zfitted(:, 1),  -Zfitted(:, 2), 'b-');
            hold off;
            legend('Measured',    'Guessed',    'Fitted',    'Location',
'SouthEast')
            title(num2str(runs(i).seqNum));
        end

        %% Show the results
        if(verbose)
            disp(['Run #' num2str(runs(i).seqNum)]);
```

```
            for k = 1:length(pNames)
                str = [pNames{k}, ': ', num2str(fitParams(k)), ', [', ...
                    num2str(cLow(k)), ', ' num2str(cHigh(k)) ']'];
                disp(str);
            end
            disp(' ');
        end

        %% Write to file
        if(writeToFile)
            fprintf(sumFH, '"%s"\t%E\t%E\t', ...
                [sampleDir slash fitFolderName slash runs(i).filename], 0,
resnorm);
            for k = 1:length(fitParams)
                errorAbs = (cHigh(k) - cLow(k)) / 2;
                errorPercent = errorAbs / fitParams(k);
                fprintf(sumFH,  '%E\t%E\t%E\t',  fitParams(k),  errorAbs,
errorPercent);
            end
            fprintf(sumFH, newline);

            simFH = fopen(simName, 'w');
            for k = 1:10
                fprintf(simFH, ['Hey you! Keep on keepin'' on!' newline]);
            end
            fprintf(simFH,
['Freq(Hz)\tAmpl\tBias\tTime(Sec)\tZ''(a)\tZ''''(b)\tGD\tErr\tRange'
newline]);
            for k = 1:length(fittedFreqs)
                fprintf(simFH, ['%E, 0.0E+00, 0.0E+00, 0.0E+00, %E, %E,
0.0E+00, 0, 0' newline], fittedFreqs(k), Zfitted(k, 1), Zfitted(k, 2));
            end
            fclose(simFH);
        end
    end
end
if(writeToFile)
    fclose(sumFH);
end
close(bar);

nonzeroEntries = find(fitParamMatrix(:, 1));
medianFitParams = median(fitParamMatrix(nonzeroEntries, :));

end


function [resVec] = ...
    WeightedArcFitting(parameters, scalingFactors, freqs, ...
                       circuitVersion, Zmeas, weight)
%WEIGHTEDARCFITTING returns residuals of calculated impedance
%   To improve the fitting ability of lsqnonlin, it is helpful to break up
%   the data into real and imaginary residuals for each point. This
%   function determines these residuals between measured data (Zmeas) and
%   the calculated data (from Circuits). The user should create an
%   anonymous function to capture the output of this function given the
```

```
%   options selected by the user.

parameters = parameters .* scalingFactors;

Zcalc = Circuits(parameters, freqs, circuitVersion);
resVec = zeros(length(freqs), 2);

switch weight
    case 'modulus'  % modulus weighting
        resVec = (Zmeas - Zcalc) ./ repmat(sqrt(sum(Zmeas'.^2)), 2, 1)';
    case 'unit'  % unit weighting
        for k = 1:length(freqs)
            resVec(2*k - 1) = (Zmeas(k,1) - Zcalc(k,1));
            resVec(2*k)     = (Zmeas(k,2) - Zcalc(k,2));
        end
    case 'proportional' % proportional weighting
        for k = 1:length(freqs)
            resVec(2*k - 1) = (Zmeas(k,1) - Zcalc(k,1)) ./ Zcalc(k,1);
            resVec(2*k)     = (Zmeas(k,2) - Zcalc(k,2)) ./ Zcalc(k,2);
        end
    otherwise
        errstr = ['Unrecognized weight string "' weight '.'];
        error(errstr);
end

end

function Z = Circuits( parameters, freq, circuitVersion )
%CIRCUITS Master circuit function file
%   This function contains all of the fitting functions
%--- Inputs
%   parameters  - the input parameters of order unity
%   freq        - column vector of frequencies
%   c_version   - a string with the version of the fit to be used
%--- Outputs
%   Z           - N x 2 array of real and imaginary impedance

switch(circuitVersion)
    case{'R', 'r'}
        Z = Resistor(parameters, freq);
    case {'RL'}
        Z = RL(parameters, freq);
    case{'RRQ', 'rrq'}
        Z = RRQ(parameters, freq);
    case{'RRQRQ', 'rrqrq'}
        Z = RRQRQ(parameters, freq);
    case{'RRCRC', 'rrcrc'}
        Z = RRCRC(parameters, freq);
    case {'RRQRQRQ', 'rrqrqrq'}
        Z = RRQRQRQ(parameters, freq);
    case{'5'}
        Z = RobCircuit_5(parameters, freq);
    case{'6a'}
        Z = RobCircuit_6a(parameters, freq);
    case{'6b'}
```

```
        Z = RobCircuit_6b(parameters, freq);
    case{'7a'}
        Z = RobCircuit_7a(parameters, freq);
    case{'7b'}
        Z = RobCircuit_7b(parameters, freq);
    case{'7c'}
        Z = RobCircuit_7c(parameters, freq);
    case{'8'}
        Z = RobCircuit_8(parameters, freq);
    case{'maier2006'}
        Z = maier2006(parameters, freq);
    case('boukamp2015')
        Z = boukamp2015(parameters, freq);
    otherwise
        errstr = ['Version ' circuitVersion ' not recognized.'];
        error(errstr);
end

end

function Z = Resistor(params, freqs)
% Simple resistor

R = params(1);

Z = R .* ones(length(freqs), 1);

Z = [real(Z) imag(Z)];

end

function Z = RL(params, freqs)
% RL parallel circuit

R = params(1);
L = params(2);
w = 2 * pi * freqs;
Z = 1./(1/R + 1./(1i * w * L));

Z = [real(Z) imag(Z)];
end

function Z = RRQ(params, freqs)
% RobCircuit_RRQ Equivalent circuit for a microelectrode.
% p = [R Rs Y n];

R   = params(1);
Rs  = params(2);
Y   = params(3);
n   = params(4);
w   = 2*pi*freqs;

Z   = R + Rs ./ (1 + Y.*Rs.*(1i*w).^n);
Z   = [real(Z) imag(Z)];
```

```
end

function Z = RRQRQ(params, freqs)
% RobCircuit_RRQRQ Equivalent circuit for a microelectrode.
% Here Q = CPE
% p = [R0 R1 Y1 n1 R2 Y2 n2];

R0   = params(1);
R1   = params(2);
Y1   = params(3);
n1   = params(4);
R2   = params(5);
Y2   = params(6);
n2   = params(7);
w    = 2*pi*freqs;

Z   = R0 + R1 ./ (1 + Y1.*R1.*(1i*w).^n1) + R2 ./ (1 + Y2.*R2.*(1i*w).^n2);
Z   = [real(Z) imag(Z)];
end

function Z = RRQRQRQ(params, freqs)
% RobCircuit_RRQRQRQ Equivalent circuit for a microelectrode.
% Here Q = CPE
% p = [R0 R1 Y1 n1 R2 Y2 n2 R3 Y3 n3;

R0   = params(1);
R1   = params(2);
Y1   = params(3);
n1   = params(4);
R2   = params(5);
Y2   = params(6);
n2   = params(7);
R3   = params(8);
Y3   = params(9);
n3   = params(10);
w    = 2*pi*freqs;

Z   = R0 + R1 ./ (1 + Y1.*R1.*(1i*w).^n1) + R2 ./ (1 + Y2.*R2.*(1i*w).^n2)
+ ...
     R3 ./ (1 + Y3.*R3.*(1i*w).^n3);

Z   = [real(Z) imag(Z)];
end


function Z = RRCRC(params, freqs)
% RobCircuit_RRCRC Equivalent circuit for a microelectrode.
% p = [R0 R1 C1 R2 C2];

R0   = params(1);
R1   = params(2);
C1   = params(3);
R2   = params(4);
C2   = params(5);
```

```
i    = 1i;
w    = 2*pi*freqs;

Z   = R0 + R1 ./ (1 + R1.*C1.*i*w) + R2 ./ (1 + R2.*C2.*i*w);
Z   = [real(Z) imag(Z)];
end

function Z = RobCircuit_5(params, freqs)
% RobCircuit_5 Equivalent circuit for a microelectrode.
% p = [Rion Rion_s Cion_s Cchem  R0]

Rion    = params(1);
Rion_s  = params(2);
Cion_s  = params(3);
Cchem   = params(4);
R0      = params(5);
i       = 1i;
w       = 2*pi*freqs;

Zion_s  = Rion_s ./ (1 + i*w*Rion_s*Cion_s);
a       = sqrt(i*w*Rion*Cchem);

Z = (Rion + Zion_s.*a.*coth(a)) ./ (Zion_s.*a.^2./Rion + a.*coth(a)) + R0;
Z = [real(Z) imag(Z)];
end

function Z = RobCircuit_6a(params, freqs)
% RobCircuit_6a Equivalent circuit for a microelectrode.
% p = [Rion Rion_s Cion_s Cchem Ceon_p R0]

Rion    = params(1);
Rion_s  = params(2);
Cion_s  = params(3);
Cchem   = params(4);
Ceon_p  = params(5);
R0      = params(6);
i       = 1i;
w       = 2*pi*freqs;

Zion_s  = Rion_s ./ (1+i*w*Rion_s*Cion_s);
Zeon_p  = 1./(i*w*Ceon_p);
a       = sqrt(i*w*Rion*Cchem);

Z = (Rion.*Zeon_p + Zeon_p.*Zion_s.*a.*coth(a)) ./ ...
    (Rion + Zion_s.*a.^2.*Zeon_p/Rion + (Zion_s + Zeon_p).*a.*coth(a)) +
R0;
Z = [real(Z) imag(Z)];
end

function Z = RobCircuit_6b(params, freqs)
% RobCircuit_6b Equivalent circuit for a microelectrode.
% p = [Rion Rion_s Cion_s Cchem Rion_p R0]

Rion    = params(1);
```

```
Rion_s  = params(2);
Cion_s  = params(3);
Cchem   = params(4);
Rion_p  = params(5);
R0      = params(6);
i       = 1i;
w       = 2*pi*freqs;

Zion_s  = Rion_s ./ (1+i*w*Rion_s*Cion_s);
Zion_p  = Rion_p;
a       = sqrt(1i*w*Rion*Cchem);

Z = (Rion^2 + Zion_s.*Zion_p.*a.^2 + Rion.*(Zion_s + Zion_p).*a.*coth(a))
./ ...
    (Zion_s.*a.^2 + Rion.*a.*coth(a)) + R0;
Z = [real(Z) imag(Z)];
end

function Z = RobCircuit_7a(params, freqs)
% RobCircuit_7a Equivalent circuit for a microelectrode.
% p = [Rion Rion_s Cion_s Cchem Rion_p Cion_p R0]

Rion    = params(1);
Rion_s  = params(2);
Cion_s  = params(3);
Cchem   = params(4);
Rion_p  = params(5);
Cion_p  = params(6);
R0      = params(7);
i       = 1i;
w       = 2*pi*freqs;

Zion_s  = Rion_s ./ (1+i*w*Rion_s*Cion_s);
Zion_p  = Rion_p ./ (1+iw*Rion_p*Cion_p);
a       = sqrt(1i*w*Rion*Cchem);

Z = (Rion^2 + Zion_s.*Zion_p.*a.^2 + Rion.*(Zion_s + Zion_p).*a.*coth(a))
./ ...
    (Zion_s.*a.^2 + Rion.*a.*coth(a)) + R0;
Z = [real(Z) imag(Z)];
end

function Z = RobCircuit_7b(params, freqs)
% RobCircuit_7b Equivalent circuit for a microelectrode.
% p = [Rion Rion_s Cion_s Cchem Yeon_p neon_p R0]

Rion    = params(1);
Rion_s  = params(2);
Cion_s  = params(3);
Cchem   = params(4);
Yeon_p  = params(5);
neon_p  = params(6);
R0      = params(7);
i       = 1i;
```

```
w       = 2*pi*freqs;

Zion_s  = Rion_s ./ (1+i*w*Rion_s*Cion_s);
Zeon_p  = 1 ./ (Yeon_p.*(i*w).^neon_p);
a       = sqrt(i*w*Rion*Cchem);

Z = (Rion.*Zeon_p + Zeon_p.*Zion_s.*a.*coth(a)) ./ ...
    (Rion + Zion_s.*a.^2.*Zeon_p./Rion + (Zion_s + Zeon_p).*a.*coth(a)) +
R0;
Z = [real(Z) imag(Z)];
end

function Z = RobCircuit_7c(params, freqs)
% RobCircuit_7b Equivalent circuit for a microelectrode.
% p = [Rion Rion_s Yion_s nion_s Cchem Ceon_p R0]

Rion    = params(1);
Rion_s  = params(2);
Yion_s  = params(3);
nion_s  = params(4);
Cchem   = params(5);
Ceon_p  = params(6);
R0      = params(7);
i       = 1i;
w       = 2*pi*freqs;

Z_A = Rion_s ./ (1+Rion_s*Yion_s*(i*w).^nion_s);
Z_D = 1 ./ (i*w*Ceon_p);
a   = sqrt(i*w*Rion*Cchem);

Z = (Rion .* Z_D + Z_D .* Z_A .* a .* coth(a)) ./ ...
    (Rion + Z_A .* Z_D .* a.^2 / Rion + (Z_A + Z_D).*a.*coth(a)) + R0;
Z = [real(Z) imag(Z)];
end

function Z = RobCircuit_8(params, freqs)
% RobCircuit_8 Equivalent circuit for a microelectrode.
% p = [Rion Rion_s Cion_s Cchem Rion_p Cion_p Ceon_p R0]

Rion    = params(1);
Rion_s  = params(2);
Cion_s  = params(3);
Cchem   = params(4);
Rion_p  = params(5);
Cion_p  = params(6);
Ceon_p  = params(7);
R0      = params(8);
i       = 1i;
w       = 2*pi*freqs;

Zion_s  = Rion_s ./ (1+i*w*Rion_s*Cion_s);
Zion_p  = Rion_p ./ (1+i*w*Rion_p*Cion_p);
Zeon_p  = 1./(i*w*Ceon_p);
a       = sqrt(i*w*Rion*Cchem);
```

```
Z = (Rion^2.*Zeon_p + Zion_s.*Zion_p.*Zeon_p.*a.^2 + Rion.*Zeon_p.*(Zion_s
+ Zion_p).*a.*coth(a)) ./ ...
    (Rion^2  +  Zion_s.*a.^2.*(Zion_p  +  Zeon_p)  +  (Zion_s  +  Zion_p  +
Zeon_p).*Rion.*a.*coth(a)) + R0;
Z = [real(Z) imag(Z)];
end

function Z = maier2006(params, freqs)
% Maier2006 Physical circuit adapted from Baumann et. al. SSI 177 (2006)
%   p    =    ['R_{lyte}',    'R_{ion,int}',    'Q_{int}',    'n_{ion,int}',
'R_{ion,surf}',
% 'Q_{chem}', 'n_{ion, surf}']

R_lyte      = params(1);
R_ion_int   = params(2);
Q_ion_int   = params(3);
n_ion_int   = params(4);
R_ion_surf  = params(5);
Q_chem      = params(6);
n_chem      = params(7);

i           = 1i;
w           = 2*pi*freqs;

Z_Q_ion_int = (Q_ion_int * (i*w).^(n_ion_int)).^(-1);
Z_Q_chem    = (Q_chem * (i*w).^(n_chem)).^(-1);

Ztop = R_ion_int + (R_ion_surf .* Z_Q_chem)./(R_ion_surf + Z_Q_chem);

Z = R_lyte + 1./(Z_Q_ion_int.^(-1) + Ztop.^(-1));
Z = [real(Z) imag(Z)];
end

function Z = boukamp2015(params, freqs)
% Boukamp2015 Physical circuit adapted from Baumann et. al. SSI 177 (2006)
%   p    =    ['R_{lyte}',    'R_{ion,int}',    'Q_{int}',    'n_{ion,int}',
'R_{ion,surf}',
% 'Q_{chem}', 'n_{ion, surf}']

R_lyte  = params(1);
R_layer = params(2);
Q_layer = params(3);
n_layer = params(4);
R_par   = params(5);
Q_par   = params(6);
n_par   = params(7);

i = 1i;
w = 2*pi*freqs;

Z_Q_layer = (Q_layer * (i*w).^(n_layer)).^(-1);
Z_Q_par   = (Q_par* (i*w).^(n_par)).^(-1);
```

```
Zbottom = Z_Q_layer + (R_par .* Z_Q_par)./(R_par + Z_Q_par);

Z = R_lyte + 1./(R_layer.^(-1) + Zbottom.^(-1));
Z = [real(Z) imag(Z)];
end
```

2. calculateDotPositions

This function is used to predict the position of all micro-electrodes from the measurement of some arbitrary number greater than 3.

```
function [ positions ] = calculate_dot_positions(
transformation_parameters )
%CALCULATE_DOT_POSITIONS Calculate the dot positions
%   Inputs:
%       alpha - coefficient of thermal expansion
%       theta_zz - rotation about the z-axis
%       theta_yy - rotation about the x-axis
%       theta_xx - rotation about the y-axis
%       s_x, _y, _z - substrate position
%   Outputs:
%       positions - matrix of dot positions

alpha_cte = transformation_parameters(1);
theta_zz = transformation_parameters(2);
theta_yy = transformation_parameters(3);
theta_xx = transformation_parameters(4);
substrate_x = transformation_parameters(5);
substrate_y = transformation_parameters(6);
substrate_z = transformation_parameters(7);
offset = [substrate_x; substrate_y; substrate_z];
% Initialize all dot positions
x_pos = -[1 1.85:0.350:8.25 9];
y_pos = -[0.8 1.3 1.7 2 2.3 2.5:0.2:3.1 3.25:0.15:4.3];

nRows = length(y_pos);
nColumns = length(x_pos);
dot_positions = zeros(nRows, nColumns, 3);

% Generate rotation matrices
R_Z = [[cos(theta_zz), -sin(theta_zz), 0]; [sin(theta_zz), cos(theta_zz),
0]; [0 0 1]];
R_Y = [[cos(theta_yy), 0, sin(theta_yy)]; [0, 1, 0]; [-sin(theta_yy), 0,
cos(theta_yy)]];
R_X = [[1, 0, 0]; [0, cos(theta_xx), -sin(theta_xx)]; [0, sin(theta_xx),
cos(theta_xx)]];

% Transform all of the points
for row = 1:nRows
    for col = 1:nColumns
        position_vector = alpha_cte * [x_pos(col); y_pos(row); 0];
```

```
        position_vector = R_Z * R_Y * R_X * position_vector + offset;
        dot_positions(row, col, :) = position_vector;
    end
end

positions = dot_positions;

end
```